SYNTHESIS, PROPERTIES, AND APPLICATIONS OF NANOPARTICLE IONIC MATERIALS

A Dissertation

Presented to the Faculty of the Graduate School

of Cornell University

In Partial Fulfillment of the Requirements for the Degree of

Doctor of Philosophy

by

Nikhil Jayathirtha Fernandes

January 2014

SYNTHESIS, PROPERTIES, AND APPLICATIONS OF NANOPARTICLE IONIC MATERIALS

Nikhil Jayathirtha Fernandes, Ph. D.

Cornell University 2014

Nanoparticle Ionic Materials are a novel materials platform consisting of a nanoparticle core and a organic, typically polymeric canopy bonded by an ionic bond. These systems are a subset of a growing field of single-component nanohybrids, where the organic and inorganic components of a nanocomposite material are bonded to form a single independent unit. This approach is necessary to overcome the ubiquitous mixing problem inherent in creating inorganic/organic hybrid materials at length scales greater than small molecules.

In order to create the ionic bond, a typical strategy involves the functionalization of the core particle with an oligomer carrying an easily ionizable group, before reacting that with the canopy containing a complementary ionizable group. Part of the work presented here demonstrates an alternate synthesis for silica, extendable to other metal oxides, utilizing the inherent surface charge of the nanoparticle to create ionic materials without using complex chemistry.

A major attraction of the nanoparticle ionic materials is their tunable mechanical properties. Several authors have reported properties ranging from soft glassy materials to Newtonian fluids, depending on composition. An exhaustive study of the dependence of mechanical and thermal properties as a function of composition has been undertaken, and phase map has been created to inform future synthesis by design endeavors in this field.

Addtionally, the effect of using multifunctional polymers that can link nanoparticles together has been studied, and it has been shown that the resulting materials are stiffer with the addition of even a small fraction of crosslinking polymers. The ionic bond is shown to have a large effect on these properties by increasing the modulus dramatically. Additionally, these materials are shown to form self-healing elastomers, with the ability to be molded repeatedly, and then to recover their elastic strength in the new conformation, opening avenues to novel materials for applications such as coatings.

BIOGRAPHICAL SKETCH

Nikhil Fernandes was born and grew up in Bangalore, India. He attended Center For Learning until 2003. He then went on to Colgate University, where he debated between majoring in chemistry and physics until the third day of his first semester, when he overslept the chemistry placement test and decided on physics. While at Colgate, he joined the New York Zeta chapter of Phi Delta Theta, worked on campus in various roles as student technical support, and volunteered with Habitat for Humanity. His undergraduate research included the properties of Laguerre-Gauss laser beams under Prof. Enrique Galvez, and he then wrote his undergraduate thesis on fluxon dynamics in Josephson junction ratchets. He graduated in 2008 *summa cum laude* with a B.A. in Physics and a minor in Applied Mathematics and as a member of the Phi Beta Kappa honors society. He then joined Cornell University in the graduate field of Applied Physics, and joined the Giannelis group to study the properties of nanoparticle ionic materials.

This dissertation is dedicated to my parents, who taught me the scientific method (along with everything else).

ACKNOWLEDGEMENTS

I would like to thank Prof. Emmanuel Giannelis for taking a chance on a student without any materials science experience or coursework, and for giving me a free rein and a lot of opportunities. I am deeply grateful for his patience, insight, and support. It has been a pleasure and an honor to belong to his research group.

I deeply appreciate suggestions and discussions with my committee members, Prof. Joel Brock and Prof. Richard Hennig.

I am very grateful for the advice and help provided by researchers at the Air Force Research Labs: Dr. Richard Vaia, Dr. Hilmar Koerner, Dr. Mike Jespersen and Dr. Peter Mirau.

I am very indebted to my colleagues in the Giannelis research group. Robert Rodriguez, whose projects I inherited; Lou Estevez, for unfailingly cheerful support; Tiffany Williams, T. J. Wallin, Xiaonan Duan, Ritu Sahore, Michelle Wu, Loan Vo, Apostolos Enotiadis, Panos Dallas, Natalie Becerra, Suren Hayrapetyan, Tomo Osawa, Antonios Kelarakis, Genggeng Qi, and all the others in the group over the last five years. It has been a pleasure working with each of them.

I am grateful to staff and faculty of the Field of Applied Physics for their support. I am also grateful for all the support, scientific and otherwise, from my fellow students in the field over the years. I am particularly grateful to Julia Mundy and Pinshane Huang for their advice and help with microscopy. I am grateful to the staff, faculty, and students of the Materials Science and Engineering department for embracing me as one of their own, both on campus and off campus.

I would like to acknowledge input from Prof. Lynden Archer, and various members of his group. Their insights have contributed immensely to my knowledge of this field.

I am grateful for the help given by Brenda Fisher and David Jung of the KAUST-CU center, of John Grazul and Phil Carubia of the Cornell Center for Materials Research, of Ruipeng Liu of

the Cornell High Energy Synchrotron Source and of Penny Burke of the Nanobiotechnology Center.

This publication is based on work supported in part by award no. KUS-C1-018-02, made by King Abdullah University of Science and Technology (KAUST). This material is based upon work supported by the National Science Foundation under Grant No. IIP-1114275 and work supported by NYSERDA under Grant No. 18507. NYSERDA has not reviewed the information contained herein, and the opinions expressed in this report do not necessarily reflect those of NYSERDA or the State of New York. This work made use of the Cornell Center for Materials Research Shared Facilities which are supported through the NSF MRSEC program (DMR-1120296). This work made use of the Nanobiotechnology Center shared research facilities at Cornell.

I would like to acknowledge my friends, from school, college, graduate school, and elsewhere. There are too many of you to list, but none of this would have been possible without your support and good humor at all times.

Finally, I would like to acknowledge my parents. If I have managed to advance knowledge in any small way, it is thanks to foundations laid by them – everything else just fell into place.

TABLE OF CONTENTS

CHAPTER 1

INTRODUCTION

Nanoparticle Ionic Materials (NIMs) are a nanoparticle – polymer hybrid materials platform built around the concept of rigid nanoparticles coordinated to a canopy of flexible polymers by ionic bonds. As such, they are a subset of "hairy" nanoparticles (HNPs), a more general platform where the challenges involved with combing inorganic nanoparticles with organic polymers is overcome by relying on chemical interactions to bond the two normally immiscible components together.[1]

NIMs were first described by Bourlinos *et al.* in 2005 as an approach to create self-suspended nanoparticles.[2,3] They were shown to be highly stable, and a versatile materials platform, and in the following years a wide variety of core and canopy combinations were reported. This versatility is reviewed in Chapter 2 (published in Chemistry of Materials as an invited review).[4] Chapter 2 also describes the general synthetic approaches used and discusses their pros and cons. It goes on to review what is known about the structure and properties of HNPs in general, and NIMs in particular, and discusses the application areas where NIMs may have a significant impact. The remainder of this dissertation focuses on specific systems, addressing, in turn, a novel method of synthesis, elucidation of the liquid-solid transition and canopy structure, and the creation of ionic networked materials.

One of the primary issues with NIMs as originally described was their relatively complex synthesis. A typical synthesis of early-generation NIMs involves functionalizing the nanoparticles with a corona that provides a chargeable group that can support the ionic interaction, and then reacting it stoichiometrically with an end-functionalized polymer.[5] The corona creation step often involves repeated dialysis/filtration steps to remove unreacted products. A new method, the corona-free synthesis, was developed based on work initially done with poly(hydroxylated) fullerenes.[6] This method, discussed in detail in Chapter 3, exploits the

surface hydroxyls found on silica nanoparticles to create charged nanoparticles without the need for any chemical modification. These NIMs are compared to controls without ionic interactions, and are shown to be more dispersed, and to have liquid-like character as opposed to solid, aggregated controls.

In chapter 4, a systematic study of the effect of canopy graft density and molecular weight is undertaken to determine the structure of the canopy, and its effect on the physical properties of a NIMs melt. Using multiple techniques, a phase diagram is established, the transition between liquid and soft glass behaviors is elucidated, and shown to correspond to a multiple layer transition discussed in Chapter 2 and seen in NMR studies by other researchers. [7–9] This phase diagram can then be used to "dial-in" mechanical properties based on molecular weights and composition.

While the field of NIMs has been focused primarily on using polymeric canopies where each canopy molecule has a single point of attachment to particles, it is also possible to use multivalent polymers to link particles together. In Chapter 5, this effect is examined using poly(ethylene oxide) molecules as a linking agent. The nanoparticle-polymer hybrid networks created using the same ionic motifs discussed in the previous chapters show large improvements in strength with little to no change in morphology or structure when the monovalent polymer is replaced by an equivalent multivalent polymer.

This concept is extended in Chapter 6 to investigate the properties of poly(dimethylsiloxane) –based crosslinked networks of silica nanoparticles. These networks are found to be solidified for relatively small volume fractions of silica nanoparticle content, and are rubbery solids. Control samples without the ionic interactions are slurries, confirming that the ionic interaction is responsible for the solid nature. The solid samples are also shown to soften

under pressure and temperature, and then recover their strength on annealing in the absence of pressure, in a repeatable process with a well-defined Arrhenius activation energy for the recovery. Differential Scanning Calorimetry suggests that the softening is due to the rupture of the ionic bonds. These systems are created by melt-mixing pure polymer with dehydrated functionalized silica particles, which provides significant advantages for large scale industrial synthesis of these materials.

REFERENCES

(1) Fernandes, N. J.; Koerner, H.; Giannelis, E. P.; Vaia, R. A. Hairy nanoparticle assemblies as one-component functional polymer nanocomposites: opportunities and challenges. *MRS Commun.* **2013**, *3*, 13–29.

(2) Bourlinos, A. B.; Herrera, R.; Chalkias, N.; Jiang, D. D.; Zhang, Q.; Archer, L. A.; Giannelis, E. P. Surface-Functionalized Nanoparticles with Liquid-Like Behavior. *Adv. Mater.* **2005**, *17*, 234–237.

(3) Bourlinos, A. B.; Chowdhury, S. R.; Herrera, R.; Jiang, D. D.; Zhang, Q.; Archer, L. A.; Giannelis, E. P.; Ray Chowdhury, S. Functionalized Nanostructures with Liquid-Like Behavior: Expanding the Gallery of Available Nanostructures. *Adv. Funct. Mater.* **2005**, *15*, 1285–1290.

(4) Fernandes, N. J.; Wallin, T. J.; Vaia, R. A.; Koerner, H.; Giannelis, E. P. Nanoscale Ionic Materials. *Chem. Mater.* **2013**, 131009111600003.

(5) Rodriguez, R.; Herrera, R.; Bourlinos, A. B.; Li, R.; Amassian, A.; Archer, L. A.; Giannelis, E. P. The synthesis and properties of nanoscale ionic materials. *Appl. Organomet. Chem.* **2010**, *24*, 581–589.

(6) Fernandes, N. J.; Dallas, P.; Rodriguez, R.; Bourlinos, A. B.; Georgakilas, V.; Giannelis, E. P. Fullerol ionic fluids. *Nanoscale* **2010**, *2*, 1653–6.

(7) Jespersen, M. L.; Mirau, P. A.; Meerwall, E. Von; Vaia, R. A.; Rodriguez, R.; Fernandes, N. J.; Giannelis, E. P. NMR Characterization of Canopy Dynamics in Nanoscale Ionic Materials. In *NMR Spectroscopy of Polymers: Innovative Strategies for Complex Macromolecules*; American Chemical Society, 2011; Vol. 1077, pp. 149–160 SE – 9.

(8) Jespersen, M. L.; Mirau, P. A.; von Meerwall, E. D.; Koerner, H.; Vaia, R. A.; Fernandes, N. J.; Giannelis, E. P. Hierarchical Canopy Dynamics of Electrolyte-Doped Nanoscale Ionic Materials. *Macromolecules* **2013**, 131204112651000.

(9) Jespersen, M. L.; Mirau, P. A.; von Meerwall, E.; Vaia, R. A.; Rodriguez, R.; Giannelis, E. P. Canopy dynamics in nanoscale ionic materials. *ACS Nano* **2010**, *4*, 3735–42.

CHAPTER 2

NANOSCALE IONIC MATERIALS

Reproduced with permission from

Chem. Mater. (*Articles ASAP)*

DOI: 10.1021/cm402372q

Nikhil J. Fernandes, Thomas J. Wallin, Richard A. Vaia, Hilmar Koerner, and Emmanuel P. Giannelis

2.1 Introduction

The addition of nanoscale fillers (e.g. spherical nanoparticles, nanotubes, and exfoliated layered materials) to polymeric matrices to create polymer nanocomposites (PNCs) has become a widely accepted method to create novel materials and enhance the properties of existing materials for a wide range of applications.[1,2] With advances in the scale-up production of nanoparticles of various compositions and geometries,[3] the field of *functional* PNCs, where the inorganic component plays a role beyond that of a mechanical filler is now achieving commercial viability. Functional PNCs combine the unique advantages of nanoscale materials (high surface area, quantum confinement, surface plasmon resonance, and superparamagnetism to name just a few) with the processability, functionality, and stability of polymers.[4,5] A growing appreciation of the role of particle arrangement and dispersion in the properties of these PNCs greatly incentivized precise control of these parameters.[4–6] A major issue in controlling dispersion is that depletion interactions, entropic factors, and chemical incompatibility between the particle and polymer all favor the aggregation of particles.[6]

One approach that has met with some success is functionalizing the surface of the nanoparticles with brushes of grafted polymer chains forming a canopy around the particle. This complements small-molecule functionalized nanoparticles, where a canopy comprised of short ligands or surfactants imparts stability and functionality mainly through enthalpic and direct molecular interactions. The extended chain architecture of the grafter polymer adds steric stability through entropic factors derived from conformational freedom within the canopy. These polymer-grafted, or "hairy" nanoparticles (HNPs) can then be dispersed in a matrix of a miscible polymer, thus minimizing chemical incompatibilities that lead to aggregation or processing

protocols relying on kinetic barriers to phase seperation.[7,8] These particles can then be dispersed in a matrix of a miscible polymer, thus eliminating chemical incompatibilities that lead to aggregation. However, some entropic associated with autophobic dewetting arise and restrict dispersion in high molecular weight polymer matrices.[8–13] Significant attention has recently focused on an orthogonal approach to these challenges, avoiding the concept of two-component blending by using the HNPs in a neat state. This eliminates the matrix completely to form true one-component hybrids (Figure 1.1).[5,14] Additionally, this concept offers precise structure and dispersion control.[15]

A variety of synthetic approaches exist to creating HNPs.[5] Most focus on covalently linking the polymer and the particle, either by surface-initiated polymerization (*grafting from*)[16–18] or by attaching an end-functionalized polymer to the particle (*grafting to)*.[19,20] Both approaches have advantages and limitations. Grafting-to limits graft density and uniformity due to the requirement that the reactive end of each additional polymer molecule has to diffuse past the steric barrier posed by the polymers that are already in place.[21] However, by separating the polymer synthesis from the grafting reaction, greater control and purity of the polymer can be achieved. Alternatively, grafting-from allows high graft densities due to the small size of each monomer, but requires careful consideration of reaction conditions (temperature, concentration, solvent and impurities) to keep the particles unaggregated in the polymerization media. Many of these trade-offs with respect to HNPs have been recently reviewed in greater detail by Fernandes *et al*.[5]

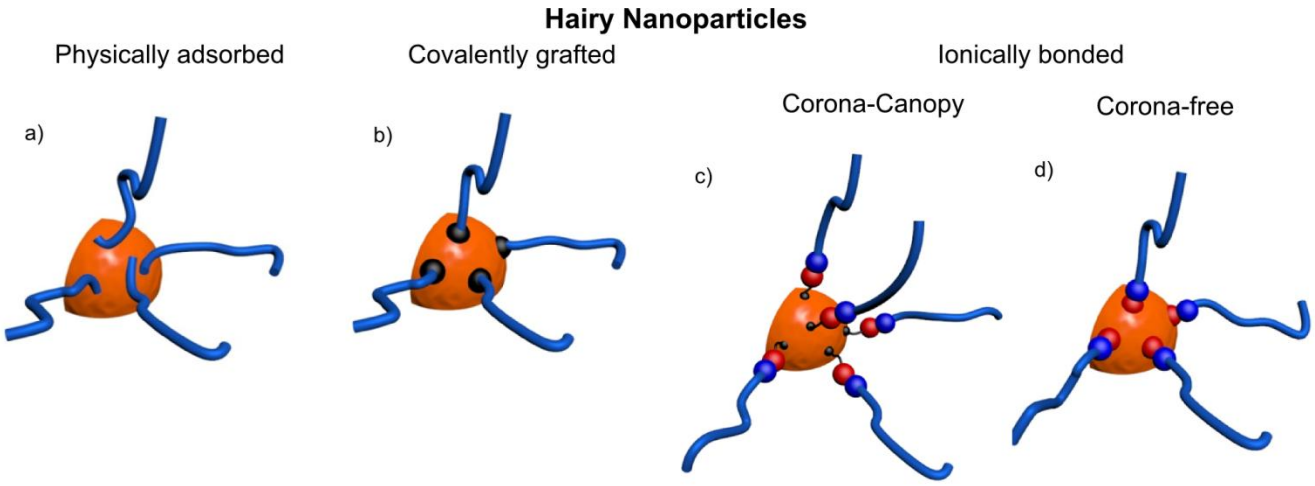

Figure 2.1: Schematic describing different methods of attaching a polymeric canopy to create hairy nanoparticles (HNPs): a) physical adsorption, b) covalent bonding, c) ionic bonding via a covalently grafted corona, and d) ionic bonding to the surface of the particle.

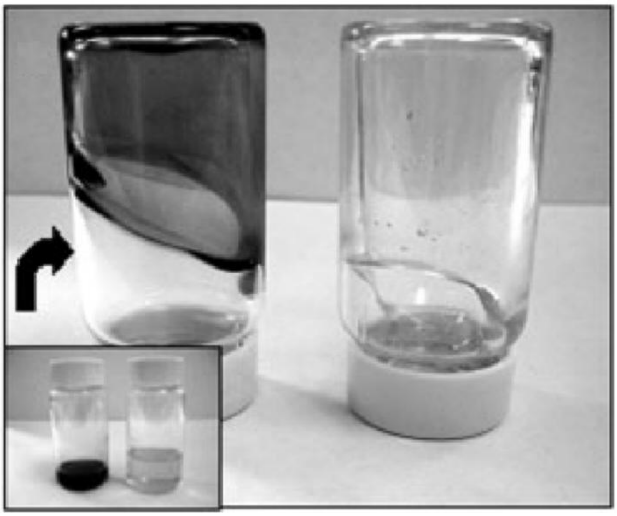

Figure 2. 2: Silica sulfonate nanosalt (right) and the same salt with dissolved methylene blue dye (left) (Reproduced with permission from Ref. 30, copyright 2005 John Wiley & Sons)

The above strategies are typically applied when forming a covalent link between the canopy and the particle. In general, though, this link need not be covalent. Ionic motifs via exchange or acid-base reactions, or multi-dentate architectures using an array of weak physioabsorbed or hydrogen bond interactions,[22,23] all provide reasonable design alternatives, especially when the dynamic character of the interface is considered a key contribution to overall performance. For such materials, the synthesis conceptually employs the "grafting-to" approach, albeit as the final step in the assembly of the polymeric canopy, and not specifically to form a covalent bond. From this perspective, hairy nanoparticle systems (HNPs) encompass not only spherical nanoparticles with covalently grafted chains (known as Polymer-Grafted Nanoparticles (PGNs)),[8] but also other discrete nanoscale hybrid structures with long chains on their surface. The coupling between the inorganic nanoparticle and macromolecular canopy can range from strongly covalent to kinetically constrained multipoint physisorption (Figure 2.1). This broader perspective of HNPs highlights the diversity and cross-fertilization of available synthetic concepts as well as the commonality of the physics underlying structure-property-processing relationships. Of these coupling options, the ionic bond (Figure 2.1(c,d)) is especially intriguing in that it allows control of both the structure and dynamics through a simple yet versatile materials platform suitable for a wide array of applications. For these Nanoscale Ionic Materials (NIMs), the canopy provides the stability, dispersion, and functionality common in solvent-free HNP systems.[5] NIMs exhibit additional dispersion stability due to electrostatic repulsion between particles, both during the synthesis and assembly stages, as well as in the final material. Additionally, the dynamic nature of the ionic links introduces structural and dynamic behavior, which has parallels to ionic liquids and ionomers. In this way, NIMs might be viewed as a HNP

materials platform analogous to the mythological chimera, combining in a single system the properties of ionic liquids, charged colloid dispersions, and hairy nanoparticle assemblies.

In the following we will review synthetic strategies for NIMs, highlight the wide library of materials that have been thus created and examine the challenges that remain. We will then discuss the state of the theoretical framework for predictive synthesis, and relate it to properties measured experimentally. Finally, we will examine some of the successful applications of these materials, and point out directions where future research and development can exploit the wide variety of accessible properties for highly improved existing applications as well as novel applications, where the full potential of such nanohybrids has not yet been investigated.

2.2 Synthetic strategies.

The fundamental structural features of all NIMs are a charge-bearing nanoparticle and an electrostatically bound oppositely-charged organic canopy (Fig 2.1(c,d)). With this in mind, NIMs synthesis involves the following steps: i) synthesis of the nanoparticle; ii) attachment of charged groups to the particle; iii) ionic coupling of the organic canopy to the particle, typically via an end group. Numerous chemical strategies exist for producing large quantities of monodisperse rigid nanoscale structures in a variety of shapes (spherical, rod, plate, and star nanoparticles) and compositions (such as metals, metal oxides, chalcogenides, biomacromolecules, to name just a few) that are reviewed elsewhere.[3,24] Similarly, a large library of monomers can be polymerized using living polymerization methods such as Atom-Transfer Radical-Polymerization (ATRP) and Reversible-Addition Fragmentation Transfer (RAFT) to yield end-functionalized, and generally monodisperse polymeric canopy species.[25,26] Permutations of this extensive number of nanoparticles and canopy species allows for a near limitless number of NIMs systems. This wide parameter space allows for selection of cores and

canopies with functionality appropriate to the application under consideration, constrained only by the synthetic requirements necessary for compatibility among the components. For this reason, the current discussion will focus on synthetic steps ii) and iii) above.

Different synthetic routes have emerged for the localization of the charge on the nanoparticle and the ionic coupling. Each method presents unique advantages and difficulties. Critical concerns in the design and implementation of any synthetic concept are: a) all components must stay dispersed and soluble to maximize yield, control and uniformity of the product, b) the surface charge density must be consistent, and, if possible tunable, as this is a critical factor in the properties of the resulting material, and c) the process must be amenable to purification and scale-up.

The creation of a charged group near the surface of the core nanoparticle has been accomplished primarily through two general means: i) covalent attachment of a ligand that contains terminally charged functional groups to form a charged corona around the core and ii) the utilization of inherent surface charges on the nanoparticle. The first approach leads to a *corona-canopy* architecture (Figure 2.1(c)), whereas the second leads to a "*corona-free*" system (Figure 2.1 (d)). One advantage inherent in either synthetic route is that the ionizable group on the particle surface confers stability in solution during synthesis by increasing the magnitude of zeta potential. This chargeable surface suppresses flocculation by electrostatic repulsion in high dielectric constant solvents, such as water, or polar organics (such as ethanol, acetone, dimethylformamide and dimethyl sulfoxide).[27] Subsequent attachment of the canopy then proceeds by either a direct ion exchange of the counterion associated with the corona or via protonation or hydroxylation of the corona via acid-base reactions.

Early work demonstrated the chemical flexibility of a corona-canopy approach. Owing to the large array of commercially available orthogonal heterobifunctional ligands, there are numerous options available for the formation of the corona.[28] For example, in the case of silica with surface hydroxyl groups, a condensation reaction with a silane is a well-established method utilized to graft oligomers to the particle surface. This feature was exploited in the first demonstration of NIMs. Bourlinos et al. condensed the silyl ether groups of a trimethoxysilane quarternary amine chloride salt to the hydroxyl groups on the surface of silica nanoparticles to yield a corona with a cationic nitrogen which endows the nanoparticles with a positive charge (Figure 2.2).[30] This same approach can be extended to other organosilane species, as illustrated by the condensation between unmodified silica and 3-(trihydroxysilyl)-1-propane-sulfonic acid.[31] In this case the ligand's exposed terminal SO_3^- group after deprotonation serves as the charged group, yielding an anionic corona. The sulfonate based system, in particular, has been extensively characterized with a variety of techniques, and can be regarded as a model system for NIMs.[31–34]

Formation of the corona through surface condensation of ligands offers many design advantages. The covalent bonds formed between the ligand and the particle are very stable and potentially multidentate (as in the organosilane above). Additionally, the approach offers the ability to attain high grafting densities. For example, in the condensation reactions above, almost all surface silanol groups are able to participate, with graft densities approaching 5 SO_3H/nm^2. Furthermore, controlling the stoichiometry of the functionalization reaction enables fine-tuning of the density of ionizable groups ($\leq$ maximum limit). [21] Alternatively, co-condensation with an inert ligand, such as octyl trimethoxysilane, maintains the total graft density but decreases the relative density of the functionalized groups, a strategy that has been successfully exploited in

"grafting from" to control the surface density of initiators.[35–37] Finally, the distance between the particle surface and the location of the ionic interaction can be adjusted by varying the molecular weight of the ligand. However, an increase in the length of the grafted ligand hinders the subsequent attachment of other ligand molecules (as discussed below) leading to a trade-off with the maximum possible grafting density.

Corona formation via condensation enables the creation of NIMs from a wide array of core materials. For example, the silane attachment method has been employed for many metal oxides, such as TiO_2 (anatase),[29] γ-Fe_2O_3 (maghemite),[30] MoS_2,[39] and ZnO[40] nanoparticles. Silanes are not the only ligands possible – metal oxide surfaces also show good reactivity towards carboxylate and phosphonate-based ligands. In fact, the phosphonate-metal oxide bond is particularly strong for anatase, and unlike organosilanes these phosphonate linkages cannot self-condense to form undesirable byproducts.[28] For noble metals (gold, silver, platinum, palladium, etc.) and noble metal coated nanoparticles, thiolated ligands provide the means to create ionic surface groups[19,41,42] and have been used to assemble NIMs based on lead sulfide quantum dots, platinum capped iron nanoparticles, and gold nanorods.[38,43,44] Other noble-metal based systems have successfully exploited weaker linkages from amines, pyridine, amino acids, and phosphines to covalently graft the ionic groups onto the particle.[5,45] Finally, a wide range of materials can be successfully capped with silica or noble metals in a core-shell paradigm,[46] providing a well-defined surface for the subsequent attachment of the corona; excellent illustrations of the latter approach are the creation of silica-coated magnetic nanoparticles, and their functionalization with an amine-terminated silane demonstrated by Lee *et al.*, [47] the creation of silica-coated cadmium selenide/zinc-sulfide quantum dot semiconductors by Gerion *et al.*,[48] and the synthesis of iron/platinum NIMs by Dallas and coworkers (Figure 2.3).[38]

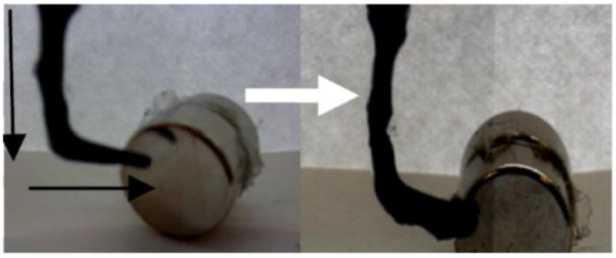

Figure 2.3: Magnetic PtFe NIMs falling down a surface have their motion affected by an external magnetic field (reproduced from Ref. 38, copyright 2013 with permission from Elsevier)

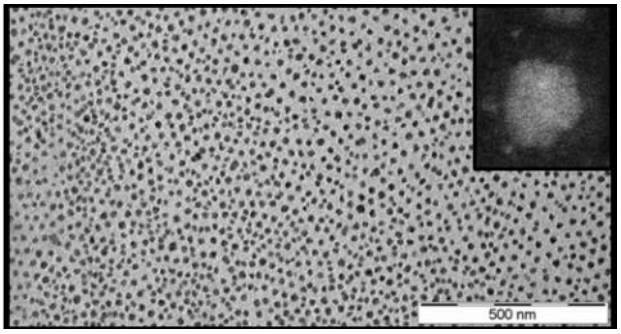

Figure 2.4: TEM of Silica/PEO-NH2 NIMs showing well-dispersed particles. The inset shows a single particle with a polymeric shell (Reproduced with permission from Ref. 50, copyright 2013 American Chemical Society),

Despite these benefits, a corona-canopy approach may not be desirable for a number of reasons. Firstly, by its very nature, the addition of the ligand layer to form a corona hinders scalability as the extra step consumes time, energy, and depending on the final application necessitates additional purification. For example, self-condensation of the organosilane can occur to form undesired byproducts, as described for γ-aminopropyltriethoxysilane by Peña-Alonso *et al.*.[49] These byproducts may be removed prior to further reaction by filtration, centrifugation, or dialysis, as shown by gel permeation chromatography during successive purifications by Gerion *et al.*,[48] but this process adds additional costs that may hinder commercial exploitation. Additionally, the requisite solvent and reactants for the corona formation step may be incompatible with the stabilization motif of the initial nanoparticle. If the ligand (or its solvent) causes flocculation of the particles, nonuniform grafting or irreversible aggregation may occur. If the initial nanoparticle stabilization relies on an oligomeric stabilizer, such as a surfactant or weakly associated ligand, removal of this displaced stabilizer after condensation will necessitate additional purification. Together, these issues introduce additional challenges for control of the synthesis and purity of the products.

To avoid these limitations, it is possible to forgo the corona-formation step and instead exploit the inherent surface charge of certain nanoparticle systems (Fig 2.1(d)). For example, the point of zero charge (pzc) of colloidal silica is at pH ~2: The surface is negatively charged above pH = 2, and positively charged below it.[51] Fernandes et al. showed that acidic surface silanol groups can be deprotonated at high pH values to leave an exposed $Si\text{-}O^-$ for direct coupling with a basic canopy such as amine-terminated poly(ethylene glycol) (Figure 2.4).[50] This strategy is not limited to silica. Based on their pzc, other metal oxides may become anionic or cationic.[52] As a general guideline, a particle with a high pzc can form the cation, while a low pzc makes the

particle suitable to be an anion. In the former case, an acid-terminated canopy is required to lower the pH below the pzc (thus forming the anion), while in the latter, a base-terminated canopy (which becomes the cation) is necessary. Amphoteric particles can play both roles, provided the canopy's functional group is a sufficiently strong acid or base. Additionally, carbonate,[53] sulfonate,[54] and phosphonate[55] inclusions on particle surfaces may all reasonably be expected to be acidic, thus expanding the library of available particles to include other mineral and polymeric nanoparticles.[56]

The corona-free approach offers some advantages especially with regard to scale up. The elimination of corona formation reduces the number of reaction steps and thus the number of compatibility issues. In addition, any material loss during the corona synthesis step can be entirely avoided. However, the lack of a corona places limitations on the final design. Most importantly, corona-free NIMs are restricted to nanoparticles that innately carry Bronsted acid or base surface functional groups. For example, metallic cores, such as Au, Ag or Pd require a corona to form NIMs. Additionally, as previously mentioned, the surface polarity (and thus the choice of functional group for the canopy molecules) is determined by the pzc of the particle. Concerns such as particle dissolution and site-specific absorption must also be considered when selecting functional groups, in contrast to well-defined and stable surfaces possible with the formation of a corona. Further, the number of acidic or basic OH groups on the particle surface is typically less than the total present preventing extremely high graft densities. For example, unmodified 16 nm colloidal silica particles have a surface silanol density of 4-5 $–OH/nm^2$ of which only 10%-20% are acidic due to the variation in the local environment of silanol group.[51,57] After careful titration of the silica nanoparticles with amine terminated polyethylene oxide ($PEO\text{-}NH_2$) Fernandes et al. found that the organic volume fraction corresponded to a graft

density of only $1nm^{-2}$.[50] This result is consistent with only a fraction of silanol groups being acidic leading to a canopy graft density which was much less than the value of 5.3 nm^{-2} achieved via the corona-canopy approach for the same silica particles.[31]

The corona-free approach has also been demonstrated for a number of carbogenic cores. Oxidation of carbon nanoparticles introduces carboxyl and hydroxyl groups on to the surface of carbon nanotubes, graphene sheets, and fullerenes.[58–61] Additionally, thermal decomposition of carbon precursors such as ammonium citrate salts yields carbon nanoparticles with cationic surface charges.[62] These surface-charge bearing particles support the aforementioned assembly approaches. To date, carbon nanotubes[63–65], carbogenic quantum dots[62], fullerenes (Figure 1.5(a))[66], and graphene[67] based NIMs have been realized. Additionally, biologically derived molecules provide another ligand-free core option that carry intrinsic surface charges. For example, backbone phosphate groups were used to create DNA-based NIMs.[29] Similarly, Perriman et al. electrostatically coupled cationized ferritin with a sulfonate-terminated polymer to yield a liquid protein complex (Figure 2.5(b)).[68] In the cationization process, dimethyl-1,3-propanediamine was covalently attached to aspartic acid and glutamic acid, two amino acids present on the surface of ferritin. This study further indicated that the approach could be extended to other proteins, such as apoferritin, myoglobin, and lysozymes, expanding the class of solvent-free liquid bionanomaterials.

Once the appropriate charge has been induced on the nanoparticles by one of these approaches, the ionic assembly with the polymeric canopy has to be formed. Two general approaches are available: ion exchange and acid-base reactions. Like all ion exchanges, the reaction is reversible, driven by Le Chatelier's principle. By adding an excess of the canopy the exchange process can be driven to near-completion. Referring again to the silica based system

from Bourlinos et al.,[30] the chloride ions present after the silation reaction with a trimethoxysilane quarternary amine chloride was exchanged for the sulfonate anion of a potassium alkyl ether sulfonate. After exchange, excess canopy and residual electrolytes (in the above case K^+ and Cl^-) need to be removed, as these can have dramatic effects on the behavior of the resulting NIMs, such as changes in mechanical properties or electrical conductivity.[69,70] Purification can be accomplished via dialysis, filtration or separation. For example, when McCuspie *et al.* used an excess of ligand and surfactant to cover gold nanoparticles and drive the ion exchange, iterative centrifugation and resuspension in a water-ethanol mixture was required to remove excess surfactant and ligand, a process monitored by the increase in inorganic content of successive precipitates from 10 % to 80 % by weight.[70] Overall, these post-synthesis purification steps are economically disadvantageous and problematic to scale-up. One possible method to circumvent these issues was demonstrated by Sun *et al,* and Dallas *et al.* (among others) when they carried out the ion exchange separately, effectively synthesizing an ionic liquid of the corona-canopy couple, and then subsequently grafting the assembly to the nanoparticle.[38,43,71] While this method simplifies purification and avoids some solvent compatibility issues, it does not completely avoid problems associated with "grafting-to" methods for large polymers, including low graft density and long reaction times.

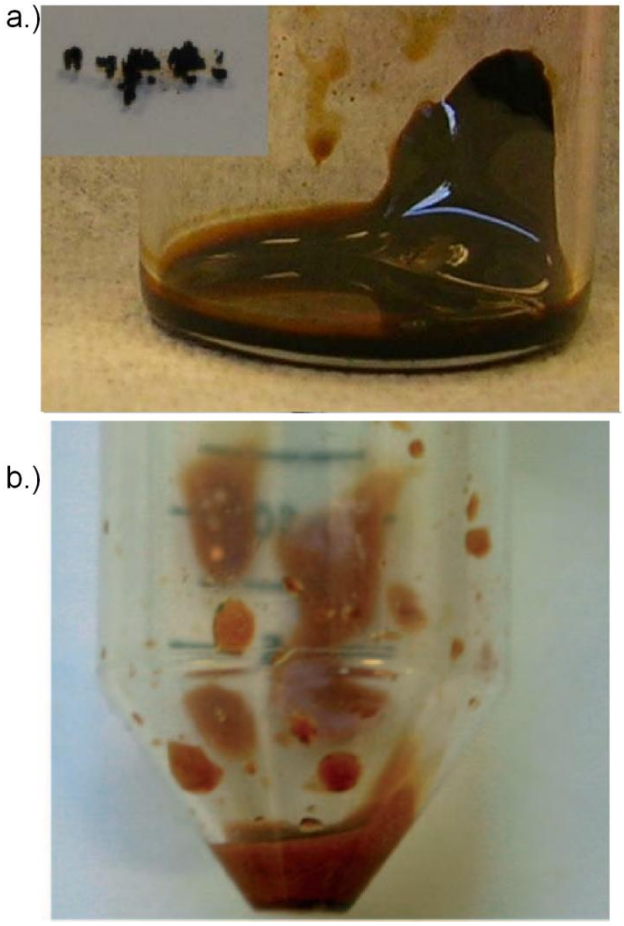

Figure 2.5: a.) Fullerol ionic liquid. (Ref. 66, Reproduced by permission of The Royal Society of Chemistry). b.) Cationized Ferritin-sulfonate NIMs after annealing (Reproduced with permission from Ref. 68, copyright 2009 John Wiley & Sons),

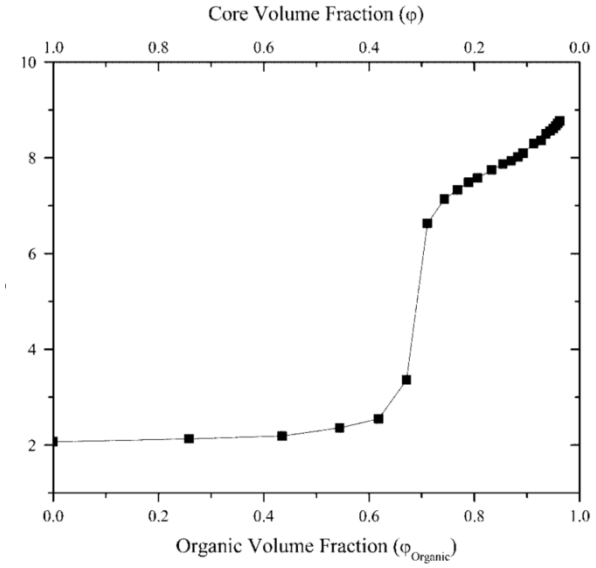

Figure 2.6: The titration curve resulting from reacting silica particles (18 nm) with a tertiary amine canopy species. The equivalence point is taken as the greatest change in slope which occurs at an organic volume fraction of 0.692 in this NIMs system. (Reproduced with permission from Ref. 32, copyright 2010 John Wiley & Sons)

As an alternative to ion exchange, the canopy coupling can be driven by an acid/base reaction between the components. Here both reactive groups are neutral (i.e. electrolytes are removed from the systems). Following stoichiometric mixing in an appropriate solvent, the conjugate acid and base are electrostatically bound. The process of canopy formation can be readily followed by a titration curve, as demonstrated by titrating sulfonic acid functionalized silica particle against a polyether amine canopy[31,32] (Figure 2.6). The inflection point in a plot of pH vs. organic (canopy) volume fraction yields the stoichiometric equivalence point. The equivalence point can be shifted by varying the number of acidic species available for reaction, by adjusting parameters such as nanoparticle size, shape, type or ligand grafting density. One constraint of this approach is that the ionic coupling reaction only occurs when the pK_a of the acid group and the pK_b of the base group are sufficiently separated to ensure the acidic species is readily deprotonated and the basic species is readily protonated at the pH of the reaction medium. It is relevant here to note that the pK_a of the acidic group has been shown to be affected by the radius of curvature of the nanoparticle, due to electrostatic interactions of the ionized acid groups.[72] Additionally, solvent selection must support the acid-base reaction with labile H^+ including an appropriately high dielectric constant to promote ionization.

In summary, different synthetic approaches have emerged for the synthesizing NIMs. Each method presents unique advantages and difficulties. Critical concerns in the choice and implementation of these approaches are: a) all components must stay dispersed and soluble to maximize yield, control, and uniformity of the product; b) the surface charge density must be consistent (and if possible, tunable) over the surface of the particle, between particles, and across multiple batches, as this is a critical factor in the properties of the resulting material, and c) the process must be amenable to purification and scale-up.

2.3 Structure and properties

While NIMs are conceptually and synthetically relatively simple, they are capable of exhibiting a wide range of behaviours due to the large parameter space accessible in this system. The ability to relate their structural, dynamic, and thermal properties to their dimensions and chemical nature of the constituent components will be critical to further exploit this new materials platform. We survey a number of theoretical and experimental studies provide a framework for understanding the properties of NIMs, starting with the nature of the ionic bond and its consequences, and then discussing theoretical and experimental characterization of the canopies, particularly in the context of studies on the closely related field of PGNs. We discuss the successes and challenges of computational approaches to the modeling of NIMs, and finally briefly touch on the wealth of experimental data that has begun to emerge on these systems

The ionic bond at the heart of the NIMs platform defines their structure and properties. The major parameter, the surface group density that can be ionized, σ_{charge}, can, as discussed earlier, vary widely. Considering silica as a model, the values range from ~1 -OH/nm^2 for bare silica[50] to 5.3 -SO_3H/nm^2 for sulfonic acid grafted silica.[31] The structure and dynamics of the canopy depend sensitively on a number of factors, including σ_{charge}, the molecular structure of the canopy, the degree of polymerization of the canopy ($N_{CANOPY)}$, and the radius of curvature of the nanoparticle ($R_{CORE)}$. This parameter space allows for extensive tuning of the bulk properties of NIMs.

Oyerekun and Vaia considered the role of R_{CORE}, canopy structure and N_{CANOPY} (indirectly, through the unperturbed Flory radius) and interaction energy of the groups at the interface on the structure of the canopy in the context of the kinetics of the grafting-to reaction.[21] They obtained an analytical expression for the optimal number of canopy molecules per

nanoparticle taking into account the loss of conformational entropy due to the crowding of chains, as well as ε, the interaction energy between the surface of the particle and the end group of the canopy.

The exact value for ε depends on the nature of the ionic groups involved. Typical values for ionic liquids can be up to ~200 kJ •mol^{-1} (~80 k_BT at room temperature) per ionic bond.[73] On the other hand, a simple electrostatic calculation by Hong and Panagiotopoulos provides an estimate of about 30-35 k_BT, based on the bead model they used.[74] Oyerokun and Vaia suggest even lower values for ε, going as low as 2 k_BT per amine/sulfonate by fitting their model to previously reported data for reaction between sulfonate-stabilized $CaCO_3$ and a polymer incorporating secondary amines.[21,75] Importantly, they verify the intuitive hypothesis that higher interaction energies lead to a larger number of surface-attached polymers, when all other factors are controlled. This model therefore has implications for all aspects of the synthesis of NIMs, starting with the choice of functional groups, and including the concentrations and size of both the core and the canopy.

Another result that emerges from the Oyerokun-Vaia model is that the average number of chains absorbed is significantly below the maximum packing of end-groups on a particle surface possible as calculated by Miracle *et al.* using geometric considerations.[76] Consider the NIMs model system described by Rodriguez *et al.*, consisting of silica nanoparticles functionalized with sulfonic acid groups as the anionic core, and amine-terminated poly(ethylene oxide)-*b*-poly(propylene oxide) as the cationic canopy.[31] Using the expression derived by Miracle *et al.*, it is easy to see that the number of canopy molecules derived from stoichiometric equivalence of the acid-base equilibrium in the formation of the ionic ensemble (nanosalt) far exceeds the

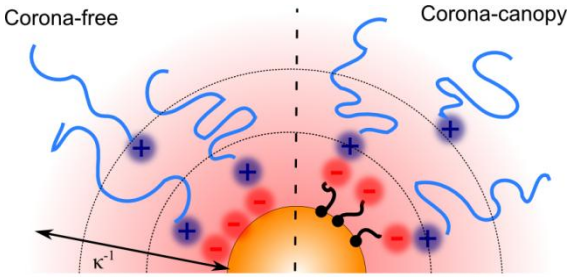

Figure 2.7: "Onion-like" model where multiple layers of canopy molecules are associated with the core, with end groups distributed out to the Debye length κ^{-1} where the electrostatic field of the core is in effect. This is valid for both corona-free and corona-canopy systems.

maximum number that can be fitted in one shell around the core particle. With R_{CORE} = 8 nm,[31] and taking the end-group dimension of the poly(ethylene oxide) based canopy to be one Kuhn length a = 0.37 nm, we find that the maximum graft density is 2.2 nm^{-2}, significantly below the stoichiometrically calculated density of 5.3 nm^{-2}.

This seeming paradox is resolved by hypothesizing an "onion"-type model where the relatively long-range coulomb interactions are able to keep multiple layers of polymeric cations around the central nanoparticle anion (Figure 2.7). From a thermodynamic description of a system of mobile charges, the Debye Length (κ^{-1} or Thomas–Fermi screening length in solids) emerges as the characteristic length of the distribution of charge away from an interface or defect. κ^{-1} scales linearly with the square root of dielectric constant and temperature and inversely with the square root of the ionic strength. For polymers (ϵ~ 2-10) at room temperature, κ^{-1} values that are consistent with an "onion" model (~ 1-10 nm) occur for local ionic concentrations of 10^{-2}-10^{-5} ions/nm^3, which is consistent with the graft densities described. This hypothesis has been verified by Jespersen and coworkers using Pulsed-Field-Gradient NMR to probe canopy transport behavior in the sulfonate based SiO_2 model system.[69] They find that there are two distinct populations of canopy molecules with different diffusion times – a strongly bound inner population with a slow diffusion constant, and a more loosely bound outer population with fast diffusion constant that is close to the diffusion constant measured for the neat canopy in the absence of nanoparticle cores. This slower diffusion time for the outer layer is attributed to the weaker electrostatic attraction between the canopy and the corona due to increased distance from the surface, and due to screening by the inner layer. When the system was spiked with one equivalent of NaCl, the Na^+ ions screened the charge on the core from both

the inner and outer layers, thus freeing the canopy to diffuse faster. This manifests as a single (fast) diffusion constant in the NMR measurements.

This multiple layer model is one of the many challenges involved in creating a theoretical foundation for predictive modeling of NIMs. To successfully capture all their behavior, any framework must incorporate elements from the models for ionic liquids, HNPs, star polymer melts, and charged colloids. The canopy structure of isolated HNPs have been studied in detail by extending the Daoud-Cotton blob model for star polymers to take into account the finite core radius of the nanoparticle.[5,77,78] Briefly, the polymer chain conformation is found to depend on R_{CORE}, graft density σ, and degree of polymerization N, as well as the Flory interaction parameter χ for the canopy and solvent. At higher graft densities, the inner portion of the chains is highly stretched in an impenetrable concentrated polymer brush regime while the outer layer (if the degree of polymerization is high enough) is in a more relaxed random walk semi-dilute polymer brush regime.

As the HNP solution becomes more concentrated, the canopies begin to impinge upon each other, leading to dispersion interactions, if the ends are in the concentrated brush regime, and entanglement interactions, if the ends are in the semidilute brush regime and can wet the brushes of the neighboring particles.[79] In the solvent-free limit, a space-filling constraint is added, which can lead to significant entropic penalties as the brushes are forced to deform to occupy all the interstitial space.[15,80–82] This additional constraint implies that interparticle constraints are no longer pairwise additive, and attempts to coarse-grain systems of solvent-free HNPs using only an interparticle potential have met with mixed success, particularly for short chains or low graft densities of large chains, where the constraint has a greater effect.[83]

Further, this model is only valid for PGNs, that is, systems in which the canopy is covalently attached to the particle surface. The long-range nature of the electrostatic interactions, and thus the varying radial distribution of the "grafting point" in the onion-like structure inferred from the NMR experiments suggest that the various brush models are only applicable for the inner layer of canopy chains. The outer layers may be hypothesized as a solvent that is strongly associated with the particle. Further, while the theory of isolated HNPs in a good solvent is relatively well established, the effect of solvent chains with degree of polymerization comparable to N_{CANOPY} is a rich field of study in itself, with the dispersion and structure formation characteristics hinging on the wetting of the canopy by the solvent.[8,84] Here, the electrostatic attraction of the "solvent" portion of the NIMs canopy to the core would play a perturbing effect that is not accounted for in studies carried out on HNPs in a polymeric matrix.

Furthermore, the aforementioned many-body interactions imposed by space filling constraints on the canopy point toward the complexity of formulating a broad theory for solvent-free HNPs that relates structure to ε, σ, N_{CANOPY}, and size polydispersity of the core. With analogy to the theoretical basis of block copolymers mesophases, such future understanding will be crucial to all facets of NIMs design for different technologies, including solvent-free NIMs assemblies comprised of stoichiometric ratios of NIMs with different cores and canopies.

Given all these challenges, simulations, rather than first-principles theory, are necessary for predictive and explanatory modeling. Molecular dynamics simulations of solvent-free HNPs have met with some success, particularly in elucidating the effect of various parameters on their diffusivity and viscosity, as well as particle distribution and structure.[85–87] Extending this work to NIMs, Panagiotopoulos and coworkers used a molecular dynamics model that models the canopy as a chain of beads with Lennard-Jones potentials with a terminal charged bead and the particle

as a rigid sphere with a monolayer of bound charges on the surface.[88] This model describes the structure of NIMs effectively, but due to the complications posed by the varying length scales, simulations are limited to small particles (with R_{CORE} of the same order as the correlation length of the polymer) and a few (<15) relatively short (N ~ 12) chains, and do not entirely capture to realistic systems. Additionally, the computational power required limits their work to 160 particles at the most. Nevertheless, this model captures many of the essential features of NIMs. In particular, they find the same canopy migration and diffusion effects observed in the NMR experiments, even with the low graft density leading to only one layer of canopy molecules.[74]

A particularly enlightening result of this work is that despite having an accurate estimate for the binding energy of the counterions from electrostatic calculations (31 k_BT), it is found that the viscosity obeys Arrhenius-type dynamics with an activation energy of 37 $kJ \cdot mol^{-1}$ (11-14 k_BT over the temperature range simulated). This energy was found to be similar to activation energies reported for covalently tethered systems, as well as polymer relaxation activation energies measured in NIMs systems,[32] suggesting that viscosity is mediated by canopy relaxation, and not canopy migration. They also find similar Arrhenius-type behavior for conductivity.

Further, they resolve the seeming paradox that the canopy is able to easily dissociate and migrate despite the binding energy being at least an order of magnitude greater than k_BT by showing that the migration occurs when the cores approach close together, thus effectively flattening the energy landscape for the canopy to 'hop' to the next core, and thus speeding canopy transport. In experimentally measured systems, the energy barrier is lowered further due to a number of factors, including the separation between charges in the "onion" model discussed

above, the availability of unbound charge sites due to steric hindrance, and screening of the charges by small ions.

Though a unified theoretical framework for understanding the behavior of NIMs is currently in its infancy, there is a wealth of experimental data on a number of systems that highlight the structure-property correlations underlying the remarkable tunablity of NIMs. Much experimental work has been focused on characterizing the fluidity of a variety of systems. The first report on NIMs by Bourlinos *et al.* was remarkable for the observed fluidity of the material, as well as its ability to dissolve other materials similar to a molecular liquid.[30] Later work has been focused on relating the relaxation of the canopy as measured by broadband dielectric spectroscopy, structure of NIMs as measured by small-angle X-ray scattering (SAXS), thermal properties as measured by differential scanning calorimetry (DSC), and flow characteristics measured by rheology.[32,89] A particularly interesting feature is that the reduced viscosity η/η_{canopy} of silica/tertiary amine-based NIMs diverges at a core volume fraction φ = 0.26, significantly before that expected for a dispersion of hard spheres at φ = 0.64. While this discrepancy was initially attributed to an increase in the effective diameter of the core and canopy, molecular dynamics simulations have revealed that the increased viscosity is at least partly due to clustering of the cores.[74] Other rheological studies have revealed the same anomalously low jamming fraction, and have demonstrated that the viscosity can be tuned over a wide range by varying N_{CANOPY} while keeping R_{CORE} and σ constant.[33]

The same system was studied using DSC and broadband dielectric spectroscopy to investigate the temperature dependence of canopy relaxation. Above the glass transition temperature, T_g, the β (local dipole) relaxations are essentially unchanged, confirming that the vast majority of the canopy is in a neighborhood of similar segments. Below T_g, the α relaxation

(segmental motions) was significantly dampened for NIMs as opposed to the neat polymer, suggesting confinement of at least some fraction of the chains. This behavior is consistent with DSC data showing that when the material is cooled below the T_m of the pure polymer, the degree of crystallinity is dramatically reduced from 100% to 20%.[32] Both the dampening in chain relaxations and reduction of crystallinity have been observed in covalently linked HNP systems, underlining that despite the dynamic nature of the link, there are significant commonalities with HNP systems in general.[90] Fourier-transform infrared (FTIR) spectroscopy on similar systems has verified that there is frustrated packing of the canopy around the core, which, in addition to having consequences for the thermal and mechanical properties of NIMs,[91] has been shown to affect the swelling behavior of the polymer. The latter has important implications for solvent and gas capture applications.[34,92,93]

While there is enough experimental and simulation data to underline the versatility of NIMs, there are many unanswered questions, particularly with regards to their structure. As expected from the layered (onion-like) canopy structure and long-range electrostatic interactions, interparticle structure is not straightforward to determine, and simple hard-sphere models are not sufficient to correctly explain the scattering profiles.[32] Some systems have shown the potential for the creation of highly ordered assemblies,[50] but very little is known about the effect of varying various parameters on this order. A phase map showing various structures has been simulated for solvent-free covalently grafted HNPs (Figure 2.8)[86,87] and even constructed for these HNPs dispersed in a matrix,[8,94,95] but there is very little such systematic work for NIMs as of yet. While there will obviously be parallels, current simulation work has shown that the charged nature of the core-canopy bond has a significant effect on structure, making mapping the structures of covalently grafted HNPs to the structure of NIMs challenging.

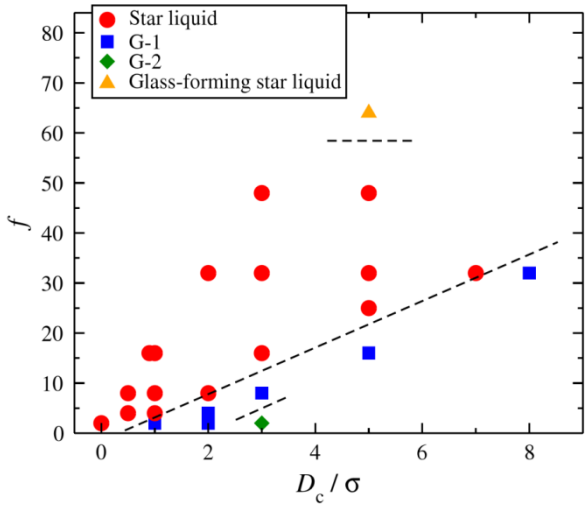

Figure 2.8: Structural map derived from Monte Carlo simulations of covalently bonded HNP assemblies as a function of the number of arms per particle, f, and Dc/σ (particle diameter/brush blob size) for a chain length of 10 brush blobs. Creation of such a phase map for NIMs would allow for more targeted synthetic strategies. (Reproduced with permission from Ref: 87 Copyright 2011 by The American Physical Society.)

Overall, two key conclusions can be drawn from the prior theoretical and experimental work. The first is that the nature of the polymer determines a wide range of properties, as demonstrated by their Arrhenius-like dependence with an activation energy that is significantly different from the binding/dissociation energy of the core and canopy. The second is that the canopy is mobile and not attached to any specific particle, and the mobility is mediated by particle-hopping.

Although molecular dynamics simulations have had some success in explaining the origin of some experimentally observed properties, the theoretical framework for relating the bulk structure and properties of NIMs with their molecular-scale structure is very limited, due in part to the large number of length and time scales involved. This is a timely area that requires additional studies, as the ability to further relate the structural, dynamic, and thermal properties of NIMs to the dimensions and chemical nature of the constituent components will be key to further exploit this new materials platform.

2.4 Current applications and future prospects:

The ionic motif is the centerpiece of the design platform, one that endows the NIMs with a versatility and a unique set of properties that open up a wide range of applications. They can be used as functional ionic liquids, highly processable nanoparticle dispersions, coatings with controlled surface properties, and also for a wide range of other applications for which HNPs have already been considered.[5]

One of the primary characteristics of NIMs is their similarity to ionic liquids, with a low to nonexistent vapor pressure and a high density of ionic groups. The usefulness of ionic liquids in a wide range of applications is well established:[96,97] For example, as electrolytes, due to their ability to conduct charge and dissolve salts,[97] green solvents and catalysts for a number of

syntheses (electrodeposition, organic synthesis and polymerization) due to their controllable acidity, thermal stability, and recyclability,[98,99] and ion, gas and biochemical sensors, to name just a few.[100] Using a nanoparticle as one of the constituents creates further opportunities. In the new design not only does the core alter the mechanical or flow behavior of the material, but the composition of the core can impart additional functionality such as a magnetic or optical response. This combination of properties is especially critical for ink development for emerging additive manufacturing and print-to-device concepts.

A major application area of current relevance in which NIMs have already being investigated in detail is their use as electrolytes for lithium-ion batteries. The use of solid polymer electrolytes and gel electrolytes has been an area of interest for some time, and the use of nanoscale metal oxide fillers in polymer electrolytes has been demonstrated to improve conductivity by several orders of magnitude, due to the Lewis acidity of the surface and the disruption of crystallite formation in the polymer.[101,102] A high degree of particle dispersion, surface functionality, disruption of canopy crystallization, and the ability to dissolve salts makes NIMs a promising choice in this field. Initial work by Moganty *et al.* focused on tethering one portion of an ionic liquid covalently to the nanoparticle cores, which led to NIMs with a large corona and small, mobile canopy (Figure 2.9).[71] This system was found to have the same characteristics that make a good ionic electrolyte – high electrochemical and thermal stability and the ability to dissolve lithium bis(trifluoro- methylsulfonyl)imide (LiTFSI), a salt often used to optimize ionic conductivity. Additionally, rheologically they behave similar to soft glasses rather than liquids, due to the effect of the cores, and it is believed that this mechanical strength resists lithium dendrite formation, increasing the lifespan and safety of the electrolyte. A more novel architecture, reported by Schaefer *et al.* relies on modifying the surface of the particle with

–SO_3H groups, and then using some fraction of these groups to attach a canopy, with the remainder of the groups used to carry lithium ions.[103] Due to the immobility of the anionic groups, this architecture provides high Li^+ transference numbers, as well as allowing for a route to tune mechanical properties by varying the degree of polymerization of the canopy, N_{CANOPY}, or the fraction of surface sites used for the canopy. This ability to "dial in" a viscosity and mechanical modulus is particularly important when dealing with non-standard battery geometries where creating a solid electrolyte is difficult. The advantages of using a gel-type electrolyte are obvious: They can resist leakage in the event of battery puncture while still being soft enough to conform to mechanical deformations without long-term residual stress. With the growing use of lithium ion batteries in applications where safety and geometry are critical, such as aviation and road transport, this platform may well become ubiquitous in the future. Another viable candidate for replacement of volatile liquids is in the growing field of carbon-capture materials. Current technology uses short-chain amines to capture CO_2 from flue gases. This technology comes with significant disadvantages, such as volatility, corrosivity, and low thermal stability window. Studies have shown that even without gas-specific functional groups for capture, NIMs show an improved gas uptake capacity relative to untethered polymer chains due to entropic effects arising from canopy ordering. [34,92,93] Since the gas uptake is due to physical factors rather than chemical interactions, varying the chemical nature of the polymer can open up a new class of fluids for SO_2, NO_2 and CO_2 capture and separation, among others. Again, the low vapor pressure and high thermal stability offer significant advantages over other liquid capture materials, while the fluidity allows for flow and transport that would not be possible with solid sorbents.

.

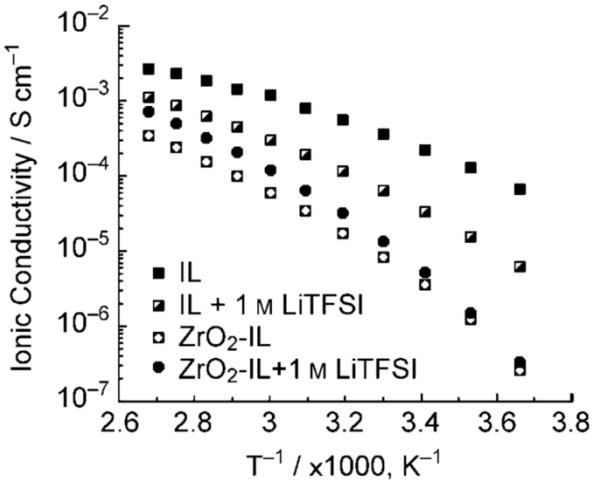

Figure 2.9: Conductivity as a function of temperature of ammonium based ionic liquid (IL) and that same ionic liquid tethered to zirconia nanoparticles to form NIMs (ZrO_2-IL). Both systems were measured with and without dissolved LiTFSI salt. (Reproduced with permission from Ref: 71 Copyright 2010 by John Wiley & Sons)

The list of applications for non-volatile fluids is in no way limited to the above-discussed systems. To consider just one more example, utilizing a magnetic core would lead to a solvent-free ferrofluid. Ferrofluids are already being widely considered for applications as diverse as lubricants and thermal transfer materials (mobile heat sinks) whose transport and localization can be magnetically controlled.[104] The ability to use solvent-free fluids would minimize issues such as viscosity changes due to solvent loss. While many of these applications rely on a single functionality, it is easy to see that they may be combined to create, for example, a magnetically pumpable carbon capture fluid.

Another area in which NIMs show considerable promise is in sensor applications. Ionic liquids have already been investigated for biological, ion-selective, and gas sensors, based on their electrochemical and mechanical response in the presence of the target molecule, and tethering them to nanoparticles would improve their mechanical properties by forming self-supporting gels.[100] Additionally, HNPs in general have been shown to offer a number of candidate materials for sensors,[5] and the fluidity and directable assembly of NIMs may provide additional opportunities in this field. One particularly remarkable example is the potential use of gold nanorod NIMs as a shear sensor. When a shear force was applied, a significant optical response, attributed to a change in the conformation of the rods affecting surface plasmon resonance, was observed (Figure 2.10).[44] With a wide library of such functional materials available for cores and canopies, this application area is ripe for further study.

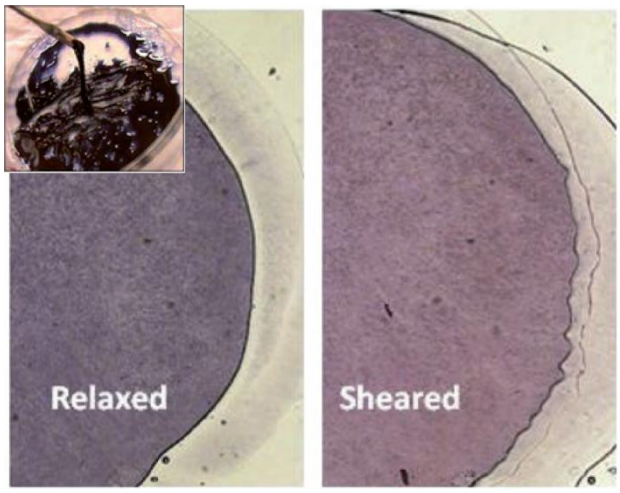

Figure 2.10: Gold nanorod based NIMs showing shear-induced chromatic shift. (Ref. 44, Reproduced by permission of The Royal Society of Chemistry)

The ability to form thin layers of fluid nanoparticles has also been exploited for creating self-healing conductive lubricant coatings for contacts on MEMS devices.[70,105,106] Gold nanoparticles provide a highly conductive interfacial layer that retains its structure despite repeated mechanical switching, providing stable electrical conduction over many cycles, and reducing common failure modes such as shorting and stiction. Any damage to the submonolayer of NIMs repairs itself by migration of the particles into the damaged area.[70,105,106] Kim and Cho demonstrated a multifunctional ionic fluid material by loading ionic-liquid-grafted gold particles with iron(III) chloride to create a magnetically switchable conducting liquid, thus adding another level of functionality to already demonstrated contact lubrication fluids.[107]

The ability to form lubricating monolayers that reduce wear has also been explored at macroscopic scales. Silica-based NIMs used as thickeners in traditional lubricating oils has created materials whose mechanical moduli and viscosity can be tuned over a wide range.[108] These lubricants exhibit lower friction coefficients than the base oil, an effect attributed to the particles acting as nanoscale ball-bearings, preventing the base oil from being expelled from the contact surfaces. NIMs have also been shown to reduce wear resistance due to the localization of the silica in the wear tracks of the contact surface. While current research has focused on NIMs as additives, there is every reason to believe that the same effects seen for solvent-free NIMs at the microscopic scale in MEMS contacts described above, such as reduced friction and self-healing capabilities, will also be seen at the macroscopic scale.

The fluidity and charged nature of NIMs can also be exploited for applications where their properties are critical for further assembly or surface modification. Kim *et al.* demonstrated the use of particles grafted to ionic liquids (which can be considered as short-canopy NIMs) for layer-by-layer deposition of thin films.[110] Such charge-based deposition has been exploited in

nanoparticle “inks” that can be selectively deposited on photolithographically modified substrates,[111] to create superhydrophilic membranes for water purification,[112–115] and to create partially permeable seperators for lithium ion batteries (Figure 2.11).[109,116] A particularly illuminating example is the use of quantum dots to create optically active films that have high efficiencies (Figure 2.12).[43,110,117] With the appropriate choice of core and canopy, it is possible to create fluorescent inks with the long photobleaching lifetimes and high quantum yield characteristic of quantum dots.[110] Quantum dot cores with conducting canopies will pave the way to the creation of easily printable flexible solar cells and LEDs, analogous to covalent HNP-type assemblies demonstrated by Liang *et al.*[118]. By changing the core functionality, printable superparamagnetic films for shielding of irregularly shaped objects in applications, where traditional Mu-metal shields would be difficult to shape become possible. Alternatively, using high-Z cores, flexible radiation attenuators can be created in a manner analogous to already-demonstrated PNC systems.[119] In this way inorganic structures with complex geometries and precise spatial composition control may be assembled without the requirement of high temperature that would ordinarily be needed for inorganic 3D printing.

Once the assembly of the cores into the required geometry is achieved, the polymer may be further processed chemically. For example, Agarwal *et al.* demonstrated the creation of shape-memory polymeric materials from NIMs by crosslinking the canopy of cast films.[120] The nanoparticles act as network points for the crosslinked polymer. This approach has potential for creating flexible inorganic materials where the nanoparticles also impart additional functionality. While current experimental work has relied on complete crosslinking, theoretical work has suggested that the dynamic nature of the ionic bonds can improve the tensile strength of the assembly, and create self-healing materials by allowing fractures to heal by reforming

bonds.[121,122] This points the way to creating self-healing materials with inorganic functionalities which can be processed into a desired geometry, creating multifunctional analogues of self-healing elastomers and nanoparticle-filled elastic membranes.[123,124]

Highly dispersed nanoparticles surrounded by a canopy can also be used as precursor materials for the creation of highly porous films. Work has already demonstrated nanoporous films[125] and monoliths[126] using highly dispersed particles surrounded by organic material as templates, then carbonizing/crosslinking the organic layer and finally removing the particle by chemical means. However, current demonstrations have been using solvent-mediated structure formation of the precursor; using solvent-free viscous fluid or soft-gel precursors allows the creation of shape-conformal templates over complex geometries. By varying polymer molecular weight, addition control can be achieved over nanoparticle spacing and thus over pore spacing.

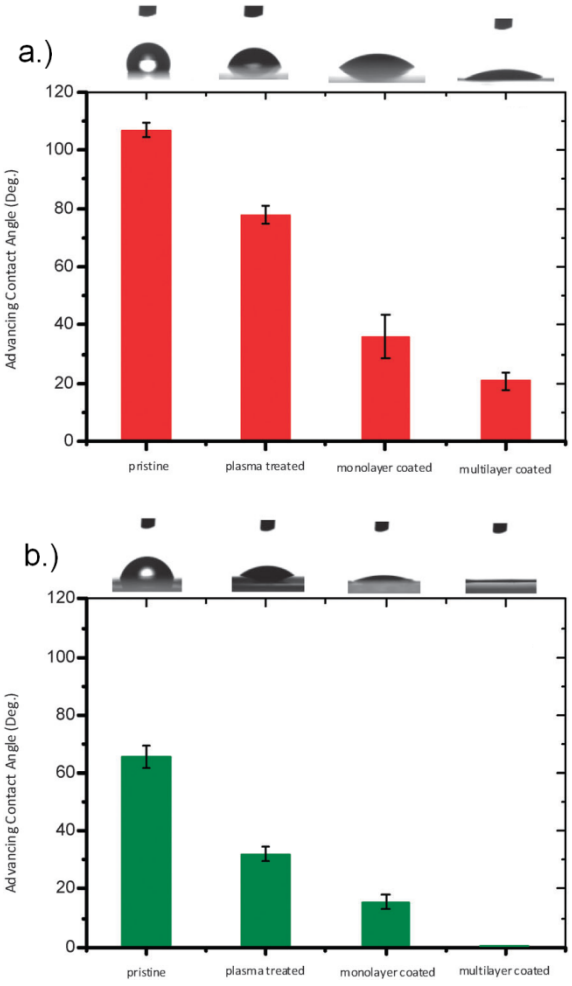

Figure 2.11: Advancing contact angles of a) water and b) propylene carbonate, a common battery electrolyte. The presence of electrostatically bound silica nanoparticle layers improves wettability of the membrane in both cases. (Reproduced with permission from Ref: 109 Copyright 2011 by The Royal Society of Chemistry)

2.5 Conclusions:

Nanoscale ionic materials are a new materials platform that exhibit a versatility in applications and properties as well as filling a niche in the broader field of polymer nanocomposites. This versatility is due to the dynamic nature of the ionic linkages as well as the tunability of the system in terms of interaction strength, graft density, core and canopy dimensions and chemistry. Their response can be described as nanoscale ionic liquids, self-suspended hairy nanoparticles, charged colloid dispersions, or well-dispersed polymer nanocomposites.

Since the first demonstration by Bourlinos *et al.* in 2005, a wide gallery of materials have been synthesized, and a large range of synthetic techniques to form the central ionic bond have been described. Several detailed investigations into the behavior of these materials have shown that they have a remarkable breadth of properties. However, to date a unified model for their behavior has yet to be developed, due to the complex interplay between electrostatic interactions and steric interactions of the polymer canopy and the cores. Currently, molecular dynamics simulations have had some success in explaining experimental measurements, but much work remains to allow for predictive design of these materials for desired properties.

Despite this limitation, several promising advances particularly in energy applications such as battery electrolytes, lubricants, thin film optical devices, and carbon sequestration have been already demonstrated. With their unique blend of properties there are many more opportunities beyond these listed and discussed, and NIMs are poised to have significant impact both scientifically and technologically.

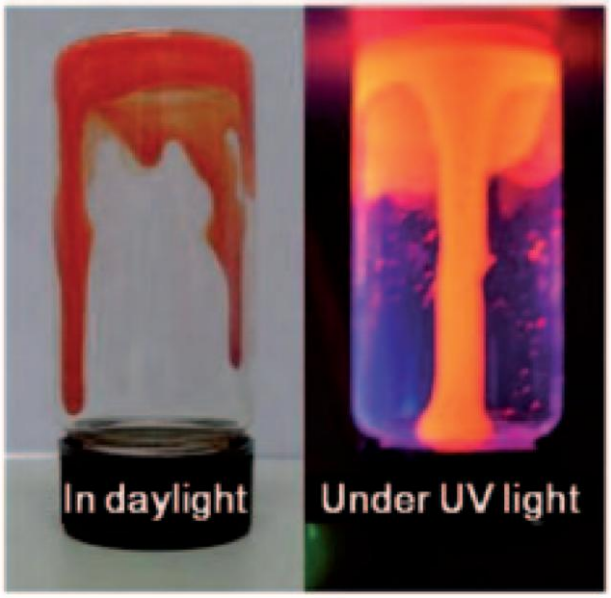

Figure 2.12: Ionic-liquid quantum dots shown in daylight and under UV light (Reproduced with permission from Ref 117, copyright 2010 John Wiley & Sons)

REFERENCES

(1) Winey, K. I.; Vaia, R. A. *MRS Bull.* **2011**, *32*, 314–322.

(2) Kumar, S. K.; Krishnamoorti, R. *Annu. Rev. Chem. Biomol. Eng.* **2010**, *1*, 37–58.

(3) Masala, O.; Seshadri, R. *Annu. Rev. Mater. Res.* **2004**, *34*, 41–81.

(4) Vaia, R. a.; Maguire, J. F. *Chem. Mater.* **2007**, *19*, 2736–2751.

(5) Fernandes, N. J.; Koerner, H.; Giannelis, E. P.; Vaia, R. A. *MRS Commun.* **2013**, *3*, 13–29.

(6) Mackay, M. E.; Tuteja, A.; Duxbury, P. M.; Hawker, C. J.; Van Horn, B.; Guan, Z.; Chen, G.; Krishnan, R. S. *Science* **2006**, *311*, 1740–3.

(7) Fischer, S.; Salcher, A.; Kornowski, A.; Weller, H.; Förster, S. *Angew. Chem. Int. Ed. Engl.* **2011**, *50*, 7811–4.

(8) Kumar, S. K.; Jouault, N.; Benicewicz, B.; Neely, T. *Macromolecules* **2013**, *46*, 3199–3214.

(9) Akcora, P.; Liu, H.; Kumar, S. K.; Moll, J.; Li, Y.; Benicewicz, B. C.; Schadler, L. S.; Acehan, D.; Panagiotopoulos, A. Z.; Pryamitsyn, V.; Ganesan, V.; Ilavsky, J.; Thiyagarajan, P.; Colby, R. H.; Douglas, J. F. *Nat. Mater.* **2009**, *8*, 354–9.

(10) Lin, Y.-L.; Chiou, C.-S.; Kumar, S. K.; Lin, J.-J.; Sheng, Y.-J.; Tsao, H.-K. *J. Phys. Chem. C* **2011**, *115*, 5566–5577.

(11) Wang, X.; Foltz, V. J.; Rackaitis, M.; Böhm, G. G. a. *Polymer (Guildf).* **2008**, *49*, 5683–5691.

(12) Smith, G. D.; Bedrov, D. *Langmuir* **2009**, *25*, 11239–43.

(13) Green, P. F. *Soft Matter* **2011**, *7*, 7914.

(14) Hui, C. M.; Pietrasik, J.; Schmitt, M.; Mahoney, C.; Choi, J.; Bockstaller, M. R.; Matyjaszewski, K. *Chem. Mater.* **2013**, 130828072046006.

(15) Koerner, H.; Drummy, L. F.; Benicewicz, B.; Li, Y.; Vaia, R. A. *ACS Macro Lett.* **2013**, *2*, 670–676.

(16) Stenzel, M. H. *Macromol. Rapid Commun.* **2009**, *30*, 1603–24.

(17) Min, K.; Gao, H.; Yoon, J. A.; Wu, W.; Kowalewski, T.; Matyjaszewski, K. *Macromolecules* **2009**, *42*, 1597–1603.

(18) Li, C.; Benicewicz, B. C. *Macromolecules* **2005**, *38*, 5929–5936.

(19) Corbierre, M. K.; Cameron, N. S.; Lennox, R. B. *Langmuir* **2004**, *20*, 2867–73.

(20) Achilleos, D. S.; Vamvakaki, M. *Materials (Basel).* **2010**, *3*, 1981–2026.

(21) Oyerokun, F. T.; Vaia, R. a. *Macromolecules* **2012**, *45*, 7649–7659.

(22) Li, M.; Wong, K. K. W.; Mann, S. *Chem. Mater.* **1999**, *11*, 23–26.

(23) Subbiah, R.; Veerapandian, M.; Yun, K. S. *Curr. Med. Chem.* **2010**, *17*, 4559–77.

(24) Cui, H.; Feng, Y.; Ren, W.; Zeng, T.; Lv, H.; Pan, Y. *Recent Pat. Nanotechnol.* **2009**, *3*, 32–41.

(25) Patten, T. E.; Matyjaszewski, K. *Adv. Mater.* **1998**, *10*, 901–915.

(26) Moad, G.; Rizzardo, E.; Thang, S. H. *Polymer (Guildf).* **2008**, *49*, 1079–1131.

(27) Greenwood, R.; Kendall, K. *J. Eur. Ceram. Soc.* **1999**, *19*, 479–488.

(28) Neouze, M.-A.; Schubert, U. *Monatshefte für Chemie - Chem. Mon.* **2008**, *139*, 183–195.

(29) Bourlinos, A. B.; Chowdhury, S. R.; Herrera, R.; Jiang, D. D.; Zhang, Q.; Archer, L. A.; Giannelis, E. P.; Ray Chowdhury, S. *Adv. Funct. Mater.* **2005**, *15*, 1285–1290.

(30) Bourlinos, A. B.; Herrera, R.; Chalkias, N.; Jiang, D. D.; Zhang, Q.; Archer, L. A.; Giannelis, E. P. *Adv. Mater.* **2005**, *17*, 234–237.

(31) Rodriguez, R.; Herrera, R.; Archer, L. A.; Giannelis, E. P. *Adv. Mater.* **2008**, *20*, 4353–4358.

(32) Rodriguez, R.; Herrera, R.; Bourlinos, A. B.; Li, R.; Amassian, A.; Archer, L. A.; Giannelis, E. P. *Appl. Organomet. Chem.* **2010**, *24*, 581–589.

(33) Agarwal, P.; Qi, H.; Archer, L. A. *Nano Lett.* **2010**, *10*, 111–5.

(34) Petit, C.; Park, Y.; Lin, K. A.; Park, A. A. *J. Phys. Chem. C* **2012**, *116*, 516–525.

(35) Cash, B. M.; Wang, L.; Benicewicz, B. C. *J. Polym. Sci. Part A Polym. Chem.* **2012**, *50*, 2533–2540.

(36) Li, C.; Han, J.; Ryu, C. Y.; Benicewicz, B. C. *Macromolecules* **2006**, *39*, 3175–3183.

(37) Soto-Cantu, E.; Cueto, R.; Koch, J.; Russo, P. S. *Langmuir* **2012**, *28*, 5562–9.

(38) Dallas, P.; Kelarakis, A.; Sahore, R.; DiSalvo, F. J.; Livi, S.; Giannelis, E. P. *J. Colloid Interface Sci.* **2013**.

(39) Zhang, Y.; Gu, S.; Yan, B.; Ren, J. *J. Mater. Chem.* **2012**, *22*, 14843.

(40) Bourlinos, A. B.; Stassinopoulos, A.; Anglos, D.; Herrera, R.; Anastasiadis, S. H.; Petridis, D.; Giannelis, E. P. *Small* **2006**, *2*, 513–6.

(41) Slocik, J. M.; Tam, F.; Halas, N. J.; Naik, R. R. *Nano Lett.* **2007**, *7*, 1054–8.

(42) Zheng, Y.; Zhang, J.; Lan, L.; Yu, P.; Rodriguez, R.; Herrera, R.; Wang, D.; Giannelis, E. P. *Chemphyschem* **2010**, *11*, 61–4.

(43) Sun, L.; Fang, J.; Reed, J. C.; Estevez, L.; Bartnik, A. C.; Hyun, B.-R.; Wise, F. W.; Malliaras, G. G.; Giannelis, E. P. *Small* **2010**, *6*, 638–41.

(44) Bhattacharjee, R. R.; Li, R.; Estevez, L.; Smilgies, D.-M.; A; Amassian, A.; Giannelis, E. P. *J. Mater. Chem.* **2009**, *19*, 8728.

(45) Mehdizadeh Taheri, S.; Fischer, S.; Förster, S. *Polymers (Basel).* **2011**, *3*, 662–673.

(46) Ghosh Chaudhuri, R.; Paria, S. *Chem. Rev.* **2012**, *112*, 2373–433.

(47) Lee, J.; Lee, Y.; Youn, J. K.; Na, H. Bin; Yu, T.; Kim, H.; Lee, S.-M.; Koo, Y.-M.; Kwak, J. H.; Park, H. G.; Chang, H. N.; Hwang, M.; Park, J.-G.; Kim, J.; Hyeon, T. *Small* **2008**, *4*, 143–52.

(48) Gerion, D.; Pinaud, F.; Williams, S. C.; Parak, W. J.; Zanchet, D.; Weiss, S.; Alivisatos, a. P. *J. Phys. Chem. B* **2001**, *105*, 8861–8871.

(49) Peña-Alonso, R.; Rubio, F.; Rubio, J.; Oteo, J. L. *J. Mater. Sci.* **2006**, *42*, 595–603.

(50) Fernandes, N. J.; Akbarzadeh, J.; Peterlik, H.; Giannelis, E. P. *ACS Nano* **2013**, *7*, 1265–71.

(51) Iler, R. K. *The Chemistry of Silica*; John Wiley & Sons, Inc.: New York, 1979; p. 865.

(52) Kosmulski, M. *J. Colloid Interface Sci.* **2002**, *253*, 77–87.

(53) Li, Q.; Dong, L.; Deng, W.; Zhu, Q.; Liu, Y.; Xiong, C. *J. Am. Chem. Soc.* **2009**, *131*, 9148–9.

(54) Brijmohan, S. B.; Swier, S.; Weiss, R. a.; Shaw, M. T. *Ind. Eng. Chem. Res.* **2005**, *44*, 8039–8045.

(55) Ziegler, A.; Landfester, K.; Musyanovych, A. *Colloid Polym. Sci.* **2009**, *287*, 1261–1271.

(56) Kosmulski, M. *Adv. Colloid Interface Sci.* **2012**, *171-172*, 77–86.

(57) Leung, K.; Nielsen, I. M. B.; Criscenti, L. J. *J. Am. Chem. Soc.* **2009**, *131*, 18358–65.

(58) Schniepp, H. C.; Li, J.-L.; McAllister, M. J.; Sai, H.; Herrera-Alonso, M.; Adamson, D. H.; Prud'homme, R. K.; Car, R.; Saville, D. a; Aksay, I. a *J. Phys. Chem. B* **2006**, *110*, 8535–9.

(59) Dreyer, D. R.; Park, S.; Bielawski, C. W.; Ruoff, R. S. *Chem. Soc. Rev.* **2010**, *39*, 228–40.

(60) Datsyuk, V.; Kalyva, M.; Papagelis, K.; Parthenios, J.; Tasis, D.; Siokou, a.; Kallitsis, I.; Galiotis, C. *Carbon N. Y.* **2008**, *46*, 833–840.

(61) Hamano, T.; Mashino, T.; Hirobe, M. *J. Chem. Soc. Chem. Commun.* **1995**, 1537.

(62) Bourlinos, A. B.; Stassinopoulos, A.; Anglos, D.; Zboril, R.; Karakassides, M.; Giannelis, E. P. *Small* **2008**, *4*, 455–8.

(63) Bourlinos, A. B.; Georgakilas, V.; Tzitzios, V.; Boukos, N.; Herrera, R.; Giannelis, E. P. *Small* **2006**, *2*, 1188–91.

(64) Bourlinos, A. B.; Georgakilas, V.; Boukos, N.; Dallas, P.; Trapalis, C.; Giannelis, E. P. *Carbon N. Y.* **2007**, *45*, 1583–1585.

(65) Lei, Y.; Xiong, C.; Dong, L.; Guo, H.; Su, X.; Yao, J.; You, Y.; Tian, D.; Shang, X. *Small* **2007**, *3*, 1889–93.

(66) Fernandes, N. J.; Dallas, P.; Rodriguez, R.; Bourlinos, A. B.; Georgakilas, V.; Giannelis, E. P. *Nanoscale* **2010**, *2*, 1653–6.

(67) Zeng, C.; Tang, Z.; Guo, B.; Zhang, L. *Phys. Chem. Chem. Phys.* **2012**, *14*, 9838–45.

(68) Perriman, A. W.; Cölfen, H.; Hughes, R. W.; Barrie, C. L.; Mann, S. *Angew. Chem. Int. Ed. Engl.* **2009**, *48*, 6242–6.

(69) Jespersen, M. L.; Mirau, P. A.; Meerwall, E. Von; Vaia, R. A.; Rodriguez, R.; Fernandes, N. J.; Giannelis, E. P. In *NMR Spectroscopy of Polymers: Innovative Strategies for Complex Macromolecules*; American Chemical Society, 2011; Vol. 1077, pp. 149–160 SE – 9.

(70) MacCuspie, R. I.; Elsen, A. M.; Diamanti, S. J.; Patton, S. T.; Altfeder, I.; Jacobs, J. D.; Voevodin, A. a.; Vaia, R. a. *Appl. Organomet. Chem.* **2010**, *24*, 590–599.

(71) Moganty, S. S.; Jayaprakash, N.; Nugent, J. L.; Shen, J.; Archer, L. A. *Angew. Chemie* **2010**, *122*, 9344–9347.

(72) Wang, D.; Nap, R. J.; Lagzi, I.; Kowalczyk, B.; Han, S.; Grzybowski, B. a; Szleifer, I. *J. Am. Chem. Soc.* **2011**, *133*, 2192–7.

(73) Fumino, K.; Wulf, A.; Ludwig, R. *Angew. Chem. Int. Ed. Engl.* **2008**, *47*, 3830–4.

(74) Hong, B.; Panagiotopoulos, A. Z. *Soft Matter* **2013**, 6091–6102.

(75) Papke, B. L.; Bartley, L. S.; Migdal, C. A. *Langmuir* **1991**, *7*, 2614–2619.

(76) Miracle, D. B.; Sanders, W. S.; Senkov, O. N. *Philos. Mag.* **2003**, *83*, 2409–2428.

(77) Ohno, K.; Morinaga, T.; Takeno, S.; Tsujii, Y.; Fukuda, T. *Macromolecules* **2007**, *40*, 9143–9150.

(78) Dukes, D.; Li, Y.; Lewis, S.; Benicewicz, B.; Schadler, L.; Kumar, S. K. *Macromolecules* **2010**, *43*, 1564–1570.

(79) Vlassopoulos, D.; Fytas, G. *High Solid Dispersions* **2010**.

(80) Yu, H.-Y.; Koch, D. L. *Langmuir* **2010**, *26*, 16801–11.

(81) Yu, H.-Y.; Koch, D. L. *Langmuir* **2013**, *29*, 8197–202.

(82) Choi, J.; Hui, C. M.; Schmitt, M.; Pietrasik, J.; Margel, S.; Matyjazsewski, K.; Bockstaller, M. R. *Langmuir* **2013**, *29*, 6452–9.

(83) Hong, B.; Chremos, A.; Panagiotopoulos, A. Z. *J. Chem. Phys.* **2012**, *136*, 204904.

(84) Green, P. F.; Oh, H.; Akcora, P.; Kumar, S. K. In *Dynamics of Soft Matter Neutron Scattering Applications and Techniques*; García Sakai, V.; Alba-Simionesco, C.; Chen, S.-H., Eds.; Springer US: Boston, MA, 2012; pp. 349–366.

(85) Goyal, S.; Escobedo, F. a *J. Chem. Phys.* **2011**, *135*, 184902.

(86) Chremos, A.; Panagiotopoulos, A. Z.; Yu, H.-Y.; Koch, D. L. *J. Chem. Phys.* **2011**, *135*, 114901.

(87) Chremos, A.; Panagiotopoulos, A. *Phys. Rev. Lett.* **2011**, *107*, 105503.

(88) Hong, B.; Chremos, A.; Panagiotopoulos, A. Z. *Faraday Discuss.* **2012**, *154*, 29.

(89) Bourlinos, A. B.; Giannelis, E. P.; Zhang, Q.; Archer, L. A.; Floudas, G.; Fytas, G. *Eur. Phys. J. E. Soft Matter* **2006**, *20*, 109–17.

(90) Tchoul, M. N.; Fillery, S. P.; Koerner, H.; Drummy, L. F.; Oyerokun, F. T.; Mirau, P. a.; Durstock, M. F.; Vaia, R. a. *Chem. Mater.* **2010**, *22*, 1749–1759.

(91) Agarwal, P.; Kim, S. A.; Archer, L. A. *Phys. Rev. Lett.* **2012**, *109*, 258301.

(92) Park, Y.; Decatur, J.; Lin, K.-Y. A.; Park, A.-H. A. *Phys. Chem. Chem. Phys.* **2011**, *13*, 18115–22.

(93) Lin, K.-Y. A.; Park, A.-H. A. *Environ. Sci. Technol.* **2011**, *45*, 6633–9.

(94) Kim, D.; Srivastava, S.; Narayanan, S.; Archer, L. a. *Soft Matter* **2012**, *8*, 10813.

(95) Srivastava, S.; Shin, J. H.; Archer, L. A. *Soft Matter* **2012**, *8*, 4097.

(96) Freemantle, M. *An Introduction to ionic liquids*; RSC Publishing: Cambridge, 2010.

(97) Armand, M.; Endres, F.; MacFarlane, D. R.; Ohno, H.; Scrosati, B. *Nat. Mater.* **2009**, *8*, 621–9.

(98) Plechkova, N. V; Seddon, K. R. *Chem. Soc. Rev.* **2008**, *37*, 123–50.

(99) Zhao, D.; Wu, M.; Kou, Y.; Min, E. *Catal. Today* **2002**, *74*, 157–189.

(100) Wei, D.; Ivaska, A. *Anal. Chim. Acta* **2008**, *607*, 126–35.

(101) Appetecchi, G. .; Croce, F.; Persi, L.; Ronci, F.; Scrosati, B. *Electrochim. Acta* **2000**, *45*, 1481–1490.

(102) Croce, F.; Appetecchi, G.; Persi, L.; Scrosati, B. *Nature* **1998**, *394*, 456–458.

(103) Schaefer, J. L.; Yanga, D. a.; Archer, L. a. *Chem. Mater.* **2013**, *25*, 834–839.

(104) Jeong, U.; Teng, X.; Wang, Y.; Yang, H.; Xia, Y. *Adv. Mater.* **2007**, *19*, 33–60.

(105) Voevodin, A. a; Vaia, R. a; Patton, S. T.; Diamanti, S.; Pender, M.; Yoonessi, M.; Brubaker, J.; Hu, J.-J.; Sanders, J. H.; Phillips, B. S.; MacCuspie, R. I. *Small* **2007**, *3*, 1957–63.

(106) Patton, S. T.; Voevodin, A. A.; Vaia, R. A.; Pender, M.; Diamanti, S. J.; Phillips, B. *J. Microelectromechanical Syst.* **2008**, *17*, 741–746.

(107) Kim, Y.; Cho, J. *Nanoscale* **2013**, *5*, 4917–22.

(108) Kim, D.; Archer, L. A. *Langmuir* **2011**, *27*, 3083–3094.

(109) Fang, J.; Kelarakis, A.; Lin, Y.-W.; Kang, C.-Y.; Yang, M.-H.; Cheng, C.-L.; Wang, Y.; Giannelis, E. P.; Tsai, L.-D. *Phys. Chem. Chem. Phys.* **2011**, *13*, 14457–61.

(110) Kim, Y.; Kim, D.; Kwon, I.; Jung, H. W.; Cho, J. *J. Mater. Chem.* **2012**, *22*, 11488.

(111) Xu, H.; Hong, R.; Lu, T.; Uzun, O.; Rotello, V. M. *J. Am. Chem. Soc.* **2006**, *128*, 3162–3.

(112) Tiraferri, A.; Kang, Y.; Giannelis, E. P.; Elimelech, M. *Environ. Sci. Technol.* **2012**, *46*, 11135–44.

(113) Mauter, M. S.; Wang, Y.; Okemgbo, K. C.; Osuji, C. O.; Giannelis, E. P.; Elimelech, M. *ACS Appl. Mater. Interfaces* **2011**, *3*, 2861–8.

(114) Tiraferri, A.; Kang, Y.; Giannelis, E. P.; Elimelech, M. *ACS Appl. Mater. Interfaces* **2012**, *4*, 5044–5053.

(115) Fang, J.; Kelarakis, A.; Estevez, L.; Wang, Y.; Rodriguez, R.; Giannelis, E. P. *J. Mater. Chem.* **2010**, *20*, 1651.

(116) Herrera Alonso, R.; Estevez, L.; Lian, H.; Kelarakis, A.; Giannelis, E. P.; Alonso, R. H. *Polymer (Guildf).* **2009**, *50*, 2402–2410.

(117) Feng, Q.; Dong, L.; Huang, J.; Li, Q.; Fan, Y.; Xiong, J.; Xiong, C. *Angew. Chem. Int. Ed. Engl.* **2010**, *49*, 9943–6.

(118) Liang, Z.; Dzienis, K. L.; Xu, J.; Wang, Q. *Adv. Funct. Mater.* **2006**, *16*, 542–548.

(119) Nambiar, S.; Yeow, J. T. W. *ACS Appl. Mater. Interfaces* **2012**, *4*, 5717–26.

(120) Agarwal, P.; Chopra, M.; Archer, L. A. *Angew. Chem. Int. Ed. Engl.* **2011**, *50*, 8670–3.

(121) Kolmakov, G. V; Matyjaszewski, K.; Balazs, A. C. *ACS Nano* **2009**, *3*, 885–92.

(122) Iyer, B. V. S.; Salib, I. G.; Yashin, V. V.; Kowalewski, T.; Matyjaszewski, K.; Balazs, A. C. *Soft Matter* **2013**, *9*, 109.

(123) Cordier, P.; Tournilhac, F.; Soulié-Ziakovic, C.; Leibler, L. *Nature* **2008**, *451*, 977–80.

(124) Tee, B. C.-K.; Wang, C.; Allen, R.; Bao, Z. *Nat. Nanotechnol.* **2012**.

(125) Tang, C.; Bombalski, L.; Kruk, M.; Jaroniec, M.; Matyjaszewski, K.; Kowalewski, T. *Adv. Mater.* **2008**, *20*, 1516–1522.

(126) Estevez, L.; Dua, R.; Bhandari, N.; Ramanujapuram, A.; Wang, P.; Giannelis, E. P. *Energy Environ. Sci.* **2013**.

CHAPTER 3

SYNTHESIS AND PROPERTIES OF HIGHLY DISPERSED IONIC SILICA–POLY(ETHYLENE OXIDE) NANOHYBRIDS

Reproduced with permission from

ACS Nano **2013**, *7* (2), pp 1265–1271

Nikhil J. Fernandes, Johanna Akbarzadeh, Herwig Peterlik, and Emmanuel P. Giannelis

2.1 Introduction

One of the major challenges at the forefront of research into nanoparticle/polymer systems is nanoparticle dispersion. The spatial distribution of nanoparticles in the polymer matrix affects a range of properties, from flow and strength to electrical and thermal conductivity. More control over nanoparticle dispersion could allow better property "tuning" and provide appropriate functionality.[1–4] In particular, the ability to keep nanoparticles isolated and uniformly dispersed is critical in creating hybrid materials that retain the fluidity of the host polymer while incorporating a high fraction of inorganic particles with their associated properties.[1,5] Fluids with high nanoparticle content are of particular interest for applications such as lubricants,[6,7] high refractive index materials for lithography,[8] battery electrolytes,[9] carbon capture materials,[10] and other applications where processability demands fluidity but functionality demands a high inorganic content. However, dispersing nanoparticles uniformly in a polymer is often challenging. Flory-Huggins theory suggests that in order to achieve a stable and uniform dispersion, the particle and polymer have to be chemically compatible, *i.e.* with an interaction parameter $\chi \leq 0$.[2] This is achieved in one of two ways; either by choosing an appropriate nanoparticle/polymer combination (such as crosslinked polystyrene particles and a linear polystyrene host), or by grafting short oligomeric or polymeric chains to the surface of the particle, creating a "corona" that has a favorable interaction parameter with the host.[11–14] The first approach limits the choice of materials in the composite. Additionally, it has been shown by Mackay *et al*. that this approach is limited to systems where the radius of the particle is less than the radius of gyration (R_g) of the polymer.[2] The second approach is more general, with a vast library of core/shell particle systems that have been made by a variety of methods,[15] but the dispersion characteristics are highly sensitive to the graft density and molecular weight of the

corona and host matrix.[16] The sensitivity of the final structure to precise synthetic control of the materials, in addition to the chemistry required to graft the corona or grow it from the surface of the particle, imposes limits on scale-up and commercial production.

An alternative approach is to graft short oligomeric chains with ionic functionalities to the particles, and then react those functionalities with a polymer end-terminated with a functionality of the opposite charge.[17–26] These Nanoparticle Ionic Materials (NIMs) are notable because they are more similar to one-phase, solvent-free molten salts than two-phase dispersions of nanoparticles. While NIMs have been demonstrated with several nanoparticle cores as diverse as metal oxides,[21,22,26,27] chalcogenides,[20] and metals,[19] all these systems still require the modification of the nanoparticle surface with a molecular corona to impart the necessary charge. For example, in silica-based NIMs the nanoparticles are typically reacted with a silane comprising of a terminal sulfonic acid or amine group.[23] While this approach has the advantage of producing a more tunable platform, it does not eliminate the grafting and purification steps entirely.

We describe here an alternative system where we exploit the favorable interactions between the polymer and the nanoparticles using an end-functionalized amine-terminated polymer (PEO-NH_2) to react with the inherently acidic hydroxyl groups present on the surface of oxide nanoparticles. We show that despite the relatively high inorganic content the SiO_2 nanoparticles are well dispersed due to the ionic interactions present in this system and the material behaves distinctly different from systems where these interactions are absent. First, the ionic hybrids show high-degree of order in both thin film and bulk forms. Second, the unique dispersion of the nanoparticles endows them with liquid-like character despite their high

inorganic content. In contrast, the controls show solid-like character and a yield stress consistent with nanoparticle aggregation and poor dispersion levels.

While we demonstrate the approach using silica nanoparticles, the method is general and can be used with a variety of nanoparticles provided that they possess surface groups that can act as acids or bases and interact with polymers containing appropriate groups. The favorable χ parameter due to the presence of strong ionic interactions ensures thorough mixing and an excellent dispersion of the nanoparticles within the polymer matrix. Either end-functionalized polymer or polymers with appropriate side groups can be utilized although the presence of multiple interaction sites could lead to crosslinked systems. We note that our approach uses commercially available colloidal silica making the process simple and scalable. In an earlier publication we focused on polyhydroxylated fullerenes,[25] but the small, well-defined molecular weight of fullerenes makes that material closer to a molecular ionic liquid than a true nanoparticle hybrid material. This approach is analogous to the use of ionic blend compatibilizers in creating well-dispersed polymeric blends,[28] with the difference being that one of the components in the blend is an inorganic nanoparticle (which has been shown to lead to an additional entropic penalty that has to be overcome).[2]

2.2 Results and discussion

Using the monomer length l_0 of 0.37 nm, C_∞ =5.6, and 44.05 g mol^{-1} for the repeat unit and molecular mass for PEO we estimate the radius of gyration for a 20 kDa coil in a Θ solvent (and therefore also in the melt) to be 7.6 nm.[29] The pH and zeta potential of the as obtained, Na^+ stabilized silica suspension (0.03 g/ml) are 11 and -30 mV, respectively. Passing the silica through a proton exchanged resin results in a suspension with a pH of about 3 and a zeta

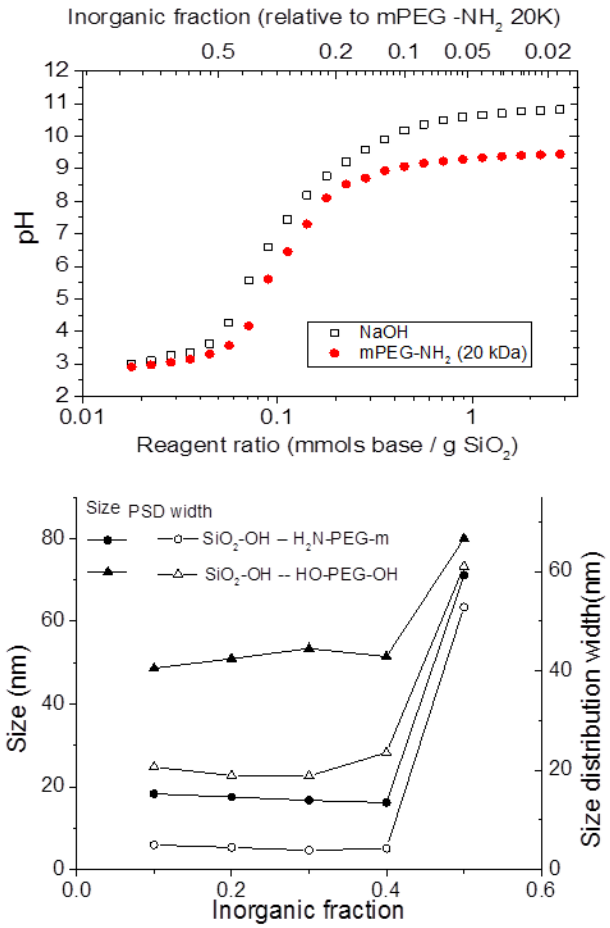

Figure 3.1: (a) pH *vs*. reagent ratio for the reaction of the silica particles with 1.5 mM NaOH (open) and 1.5 mM PEO-NH_2 (closed). The upper axis shows the inorganic fraction for the ionic hybrid . (b) DLS results corresponding to the titration curves, showing modal size (filled) and size distribution width (open) for the ionic material (O) and a silica/PEO mixture (Δ).

potential of -5 mV. The pH and zeta potential values indicate that nearly all surface groups are in the neutral, protonated form.[30,31]

The acidity of silica surface hydroxyls (silanols) is well established, although the exact pK_a values vary depending on the system. Typically, two pK_a values have been reported for silanols – one in the 4-5 range, and another in the 8-10 range.[32–34] The surface silanol density is about 4-5 -OH/nm^2, of which the more acidic groups are reported to be anywhere between 10% to 20%. We expect only the more acidic sites to take part in an acid-base reaction with PEO-NH_2

Figure 3.1(a) shows the pH profiles obtained in titrating NaOH solution and the amine-terminated polymer with the H^+-exchanged silica suspension. The reaction with PEO-NH_2 can be represented by

$$(SiO_2)\text{--}OH + H_2N\text{--}PEO \rightleftharpoons (SiO_2)\text{--}O^- H_3{}^+N\text{--}PEO$$

As silica is added to the PEO-NH_2 solution the equilibrium shifts to the right and an ionic hybrid is formed. At a pH of 8.5, the zeta potential of the resulting suspension was about ζ = -17 mV, indicating that the protons from the silanols have reacted with the terminal amine groups on the PEO, and the particles are again negatively charged. If more silica is added, the pH drops rapidly as the concentration of free acidic silanols increases. In contrast, when the (SiO_2)-OH is added to OH-PEO, the pH drops immediately to 4 as the number of free acidic silanol groups goes up from zero, and then remains essentially unchanged since there is nothing to counteract the acidity of the free silanols. The measured point of complete reaction as 0.28 mmols per gram of SiO_2 corresponds to an inorganic volume fraction of 0.15 in the hybrid with 20 kDa PEO-NH_2. If α is the inorganic mass fraction for a given hybrid, then the number of polymer molecules per particle N is given by:

$$N = \frac{4}{3}\frac{\pi r^3 \rho_{core} N_A}{M_W}\left(\frac{1-\alpha}{\alpha}\right)$$

Where ρ_{core} and r are the density and radius of the silica particle, N_A is Avagadro's number, and M_W is the molar mass of the polymer. If we take the equivalent point to be at α = 0.15, we obtain N = 805 for the 20 kDa PEO, which corresponds to an active silanol density of 1 nm^{-2} and in excellent agreement with the estimate of 20% of the total number of the silanol groups (5 OH/nm^2) being acidic.

Aliquots of the solution were taken at regular intervals during the titration experiment and the size was measured by Dynamic Light Scattering. The particle size obtained is shown in Figure 3.1(b). In the case of the amine-terminated PEO, the particles stay dispersed in solution until the pH drops below 6, at which point the solution becomes turbid and the particles aggregate, as seen by a jump in both the nominal particle size, and by the width of the size distribution.

The protonation of the silica and the formation of the ionic bonds are essential to obtaining a good dispersion of particles into the polymer. Figure 3.2(a) is a TEM micrograph of a sample consisting of 20% by weight SiO_2 nanoparticles and a 20 kDa PEO-NH_2, showing excellent dispersion with the silica nanoparticles evenly dispersed in the polymer. In contrast, aggregation and phase-separation of the particles in the polymer can be seen in Figure 3.2(b), which shows a TEM micrograph of an identically prepared sample but where sodium-stabilized silica particles were used, and Figure 3.2(c), which shows a TEM micrograph of an identically prepared sample with proton-exchanged silica particles and hydroxyl-terminated PEO.

PEO is known to absorb on the surface of silica *via* hydrogen-bonding involving terminal groups or the backbone ether oxygens.[35,36] In the case of the amine-terminated PEO, the amine groups preferentially react with the surface silanols of the particles, and since there is a single

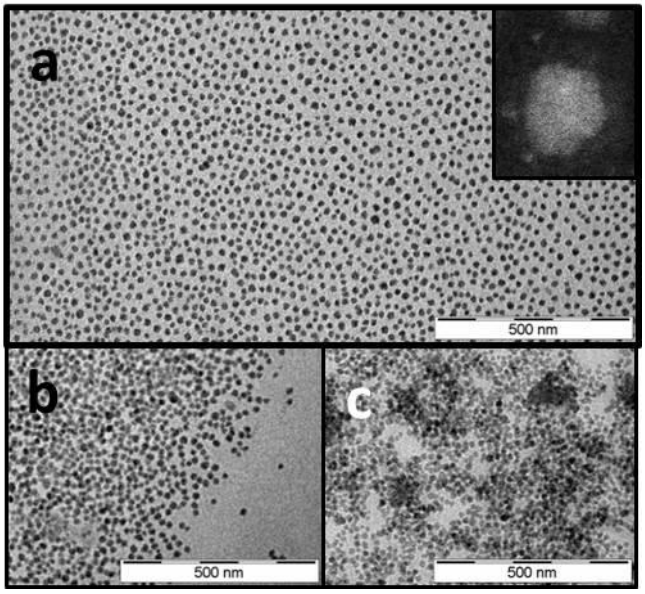

Figure 3.2. TEM images of (a) ionic material (with inset showing HAADF image of a single particle with a polymeric shell; (b) phase separated mixture of Na^+ stabilized particles mixed with polymer, and (c) HS30-OH particles mixed with unfunctionalized PEO.

reactive group per PEO molecule, each particle becomes surrounded with a layer of PEO chains. In contrast, with the HO-PEO, the particles aggregate immediately, even at low inorganic fractions, as seen in Figure 3.1(b), a phenomenon that has been exploited to flocculate stable silica suspensions.

The "ordering" shown in Figure 3.2(a) can be analyzed to determine the packing geometry of the particles. The positions of the particle centers are extracted using the software package ImageJ, and then a Matlab script is used to create a Voronoi diagram. Figure 3.3(a) shows the same sample with a superimposed Voronoi diagram. It is easy to see that the majority of particles are hexagonally coordinated, with "point defects" consisting of somewhat larger or smaller particles, and "line defects" consisting of alternating pentagonally and heptagonally coordinated particles. We conclude that the particles pack as spheres in 2D, which is consistent with a spherical shell surrounding each particle. This shell is invisible in brightfield TEM, but seen using HAADF-STEM (Figure 3.2(a) inset). The fact that the arrangement is not perfectly crystalline is due to inhomogeneity in the particle sizes. The defect lines in the Voronoi diagram do not form complete grain boundaries because the polymer shell is soft, allowing the defects to re-absorb into the hexagonal structure.

Small-angle X-ray scattering (SAXS) measurements were carried out on the ionic hybrid and both control samples in order to obtain structural information on the distribution of the particles. The samples were heated to 75°C (above the melting temperature of PEO) to probe the arrangement of particles and eliminate any complications from the crystallinity of the PEO chains.

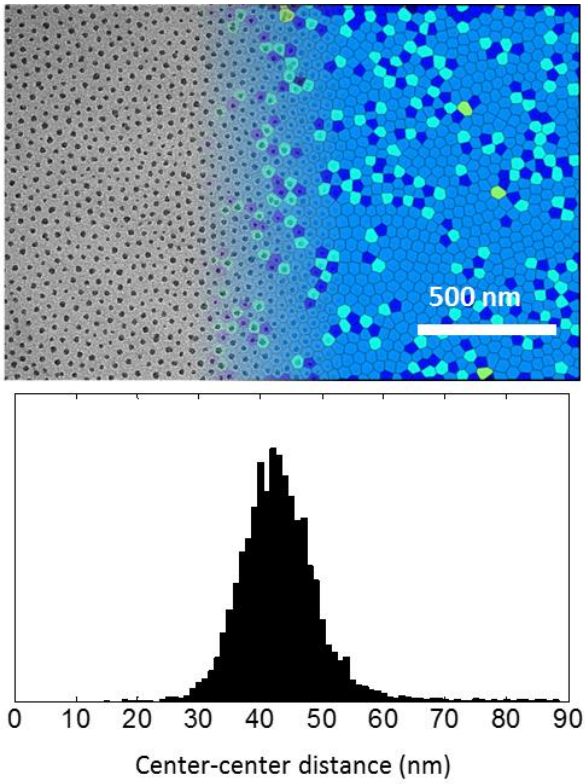

Figure 3.3: (a) Voronoi diagram of a TEM image of the ionic material , color-coded by coordination number of each cell. (b) Histogram of center-to-center distributions obtained from analysing the Voronoi image.

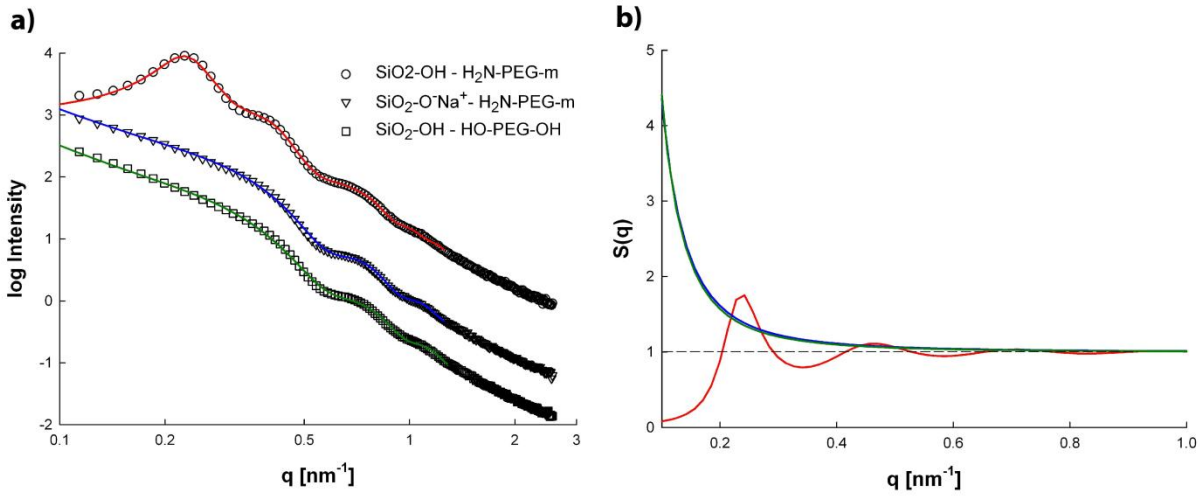

Figure 3.4: (a) Scattering curves of the ionic material (o), Na^+ stabilized HS30 particles in PEO (Δ) and HS30-OH mixed with unfunctionalized PEO (□). The curves are vertically shifted for better visibility. (b) Corresponding structure factors obtained from GIFT.

The scattering curves of all three samples are shown in Figure 3.4(a). In general, the scattering intensity of a two-phase system of polydisperse particles can be described as the product of the form factor *P(q)* and an effective structure factor *S(q)* by $I(q) \propto (\Delta\rho)^2 P(q) S(q)$ where Δρ is the electron density difference between the two phases, *i.e.* the silica core and the polymer matrix. [37]For dilute systems with negligible interparticle interactions, the structure factor is constant, *S(q)=1*. For such samples, the scattering curve can be fully described by the form factor *P(q)*.

All three samples show small modulations in the scattering intensity between q = 0.4 to 1.5 nm^{-1} which allow us to determine the amount of polydispersity and result in a mean diameter and a Gaussian half-width for silica particles with d = 16±2 nm, which is consistent with TEM measurements of the size of the particles. The ionic hybrid shows two additional peaks in the range between 0.2 and 0.4 nm^{-1}. They can be attributed to the short-range order, *i.e.* the presence of electrostatic interactions between the negatively-charged silica cores and the positively charged PEO-NH_2 chains, which leads to a regular arrangement with a characteristic particle-to-particle distance. From the position of the first peak, the distance between two silica particle centers is roughly $d = 2\pi/q_{max} = 27$ nm

The control samples (Na^+ stabilized HS30 particles in PEO and HS30-OH mixed with unfunctionalized PEO) do not exhibit a distinct short-range order peak, but an intensity increase towards very low q-values. These results indicate some agglomeration and are described here by a structure factor from a fractal model.[38,39] To separate the effect from structure factor and form factor, we used the generalized indirect Fourier transformation (GIFT) for data evaluation.[40,41]

GIFT allows us to simultaneously determine both the pair distance distribution function p(r) and pair correlation function g(r), describing the shape of particles and their interaction in

real space. Since the ionic material consists of charged particles, we decided to use the Yukawa potential for charged spheres as a structure factor model, which can be solved by a rescaled mean spherical approximation (RMSA).[42,43] From the model, one obtains a particle-to-particle distance of 27.2 nm from the first peak maximum of the structure factor (Figure 3.4(b)).[44] Additionally, one obtains an effective hard sphere volume fraction η, which describes the probability of finding two particles at a well-defined distance from each other, in analogy with the packing of hard spheres. The value of η is 0.38, suggesting a high degree of order in the system. Note that η in an ordered SC lattice is 0.52. The degree of ordering in the ionic hybrid system is even more astonishing considering that the measurements were carried out at 75 °C, where the system is a fluid.

In contrast, the structure factor in the control systems is described with a fractal model,[38,39] which corresponds to a wide range of different particle-to-particle distances. This agglomeration is also visible in the TEM images (Figure 3.2(b) and 3.2(c)). The wide size distribution leads to no specific short-range order peak, but to an intensity increase towards low q-values (Figure 3.4(a)). The corresponding structure factors from the fractal model are shown in Figure 3.4(b). The value for the fractal dimension is 2.4, indicating the mass fractal nature of the control samples. It should be noted that large agglomerates with a more well-defined size can be seen in Fig 3.2(c), but their size is larger than 100 nm and a short range order peak would not be within the accessible q-range of the SAXS measurements.

An estimate for the brush height of polymer is given by:[45]

$$\left(\frac{h}{H_0}\right)^3\left[1+\frac{3}{4}\left(\frac{h}{\omega H_0}\right)+\frac{1}{5}\left(\frac{h}{\omega H_0}\right)^2\right]=1$$

where $H_0=\left(\frac{8}{\pi^2}\right)^{1/3} l_0 N\nu^{1/3}\sigma^{*1/3}$, $\omega=\frac{R_0}{H_0}$, $\sigma^*=\sigma l_0^2$ and $\nu=\left(\frac{1}{2}-\chi_{PP}\right)$

With graft density σ = 1 nm^{-2}, degree of polymerization N = 454, nanoparticle radius R_0 = 8 nm, and setting the Flory parameter $\chi_{PP} = 0$ to capture the fact that in a melt the polymer is its own solvent, we can solve for h, obtaining h = 21 nm. If we consider each particle and its associated polymer as a single sphere, we would find (from the particle-particle separation of 27.2 nm calculated by SAXS) a brush height of 5.6 nm. The seemingly large discrepancy is explained by two factors. First, the polymers attached to neighboring particles interpenetrate strongly, since there is no other solvent in the system to swell the brushes. Second, there is a space-filling constraint; the polymer has to fill all the interstices between the hard spheres.[46] These two factors combine to reduce the particle-particle separation from the theoretically predicted value.

The larger particle-particle distance seen in the TEM images is believed to be a consequence of the drop-casting method for the preparation of thin samples: as the solvent evaporates, the core-shell spheres shrink anisotropically, forming disks that by conservation of volume have a larger lateral radius than the original sphere in 3 dimensions.

The consequences of a well-dispersed system of particles are dramatically manifested in their rheological behavior. Samples were characterized by imposing a constant oscillatory strain $\gamma(t) = \gamma_0 \sin(\omega t)$ within the linear viscoelastic regime, and monitoring the complex viscosity, $\eta^*(\omega)$, and the complex modulus, $G^*(\omega) = G' + iG''$. A convenient way to study different materials is to plot the complex viscosity as a function of the complex modulus (Figure 2. 5).[47] The neat PEO-NH_2 behaves like a Newtonian fluid, with constant viscosity across the measured range of complex moduli. On the other hand, the controls, which show significant phase separation and aggregation by TEM and SAXS, show a divergent η* at low G*, characteristic of solid materials with a yield stress. This divergence has been attributed to the formation of

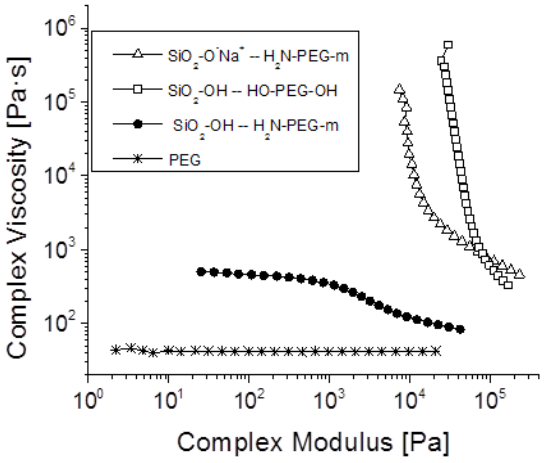

Figure 5. Cross plot of viscosity against complex modulus for Na+ stabilized particles in PEO (Δ), HS30-OH mixed with unfunctionalized PEO (□), the ionic material (●) and pure PEO (*), showing that the ionic material is a viscoelastic fluid while the other materials are yielding solids.

networks of particles within the material.[1,5] In contrast, the ionic hybrid shows shear thinning, but also has low viscosities across the entire span of complex moduli measured. We attribute this fluid-like behavior to three factors: First, the ability of the ionic hybrid to resist phase separation due to the more favorable polymer-particle interactions than polymer-polymer and particle-particle interactions, which prevents the formation of reinforcing particle networks. Second, the ability of chains to "hop" from one particle to another has been shown to enhance fluidity, as seen in NMR studies of other NIMs systems.[48] And finally, the outer portion of the polymer chains that occupies the interstices between the spheres acts as a solvent for the rest of the system.[49] The shear thinning behavior has been shown by simulations on solvent-free grafted polymer systems as due to the alignment of chains in the material.[50]

3.3 Conclusions

We report a simple and scalable method of synthesizing well-dispersed nanoparticle/polymer hybrids comprised of relatively high volume nanoparticle fractions by exploiting the electrostatic interactions as a result of an acid-base reaction between the native silanol groups of silica and an amine-terminated polymer. While we demonstrate here silica as a model system the approach can be easily extended to other oxide or nitride nanoparticles and polymers with complementary functional groups. The ionic hybrids show remarkable dispersion of the nanoparticles and appeared ordered in both thin films (TEM images) and bulk forms (SAXS). Control hybrid samples, where the ionic interactions have been turned off intentionally, show high levels of nanoparticle aggregation and behave more like conventional nanoparticle/polymer mixtures. The unique dispersion of the nanoparticles endows them with liquid-like character despite their high inorganic content. In contrast, the controls show solid-like character and a yield stress consistent with nanoparticle aggregation and poor dispersion levels.

3.4 Materials and Methods

Amine-terminated poly(ethylene oxide) (PEO-NH_2) (FW 20 kDa, PDI 1.02) was purchased from Laysan Biotech. Ludox sodium-stabilized, silica (HS30, average diameter 16±2 nm), poly(ethylene oxide) (PEO) (FW 20 kDa) and Dowex HCR-W2 ion exchange resin were obtained from Sigma Aldrich. All materials were used as supplied.

To create the ionic hybrid the HS30 silica suspension is first diluted to 3 wt% and passed three times through a column of H^+-exchanged Dowex resin to fully protonate the surface hydroxyls to form a suspension referred to as (HS30)-OH.

The optimal silica:PEO ratio was determined by first titrating a known volume of 3% (HS30)-OH solution with a 1.5 mM NaOH solution and monitoring the pH (Figure 1(a)). We find that the surface of the silica is neutralized (as evidenced by the change in the slope of the pH curve) at a ratio of 0.28 mmols of NaOH per gram of SiO_2 particles.

SiO_2/PEO-NH_2 hybrids were synthesized by adding the silica suspension dropwise to a 3% (1.5 mM) solution of PEO-NH_2 solution to reach the desired composition. The suspension was then stirred vigorously for about six hours before freezing with liquid nitrogen and then placing in a lyophilizer to remove the water. All samples were then annealed at 75°C in vacuum for 48 hours before characterization.

Two control samples void of any ionic interactions were prepared for comparison following the procedure described above. In the first a hydroxyl-terminated poly(ethylene oxide) (MW 20,000) was used. In the second the pristine sodium-stabilized silica suspension (HS30)-Na^+ (without the H^+ exchange step) was added directly to the PEO-NH_2 solution.

For electron microscopy, the samples were diluted to 1% by weight in deionized water, and then a 5µL drop was placed on a copper grid and allowed to rest for a minute before most of the water

was blotted away. The grid was dried completely in air, and then annealed in vacuum at 75°C before imaging. Brightfield TEM was carried out on a FEI Tecnai T12 microscope operating at 120 kV. High-Angle Annular Dark Field microscopy was carried out on a FEI Tecnai F20 microscope, operating at 200 kV. Dynamic Light Scattering and zeta potential measurements were carried out on a Malvern Instruments Zetasizer Nano. Rheological measurements were conducted on a Anton Paar MCR-501 Rheometer with a peltier/nitrogen gas heating chamber and 25 mm diameter cone and plate geometry (measuring system CP25-1). All rheological measurements were carried out at 75°C.

Small angle X-ray scattering (SAXS) experiments were carried out on a Bruker NanoStar Turbo X-ray source (rotating anode generator with CuKα radiation, wavelength 0.1542 nm) and equipped with a pinhole camera. The radiation is monochromatized and collimated with crossed Goebel mirrors. The samples were placed into quartz glass capillaries with ten microns thick walls (Hilgenberg, Germany) and the measurements on the bulk materials were carried out at 75°C. The X-ray images were recorded for 900s with a 2D position sensitive detector (Vantec 2000), corrected for background scattering and radially integrated to obtain the scattering intensity as a function of the scattering vector, $q = (4\pi/\lambda) \sin \theta$, with 2θ being the scattering angle and λ the X-ray wavelength.

3.5 Acknowledgement

This publication was based on work supported by award no. KUS-C1-018-02, made by King Abdullah University of Science and Technology (KAUST). This material is based upon work supported by the National Science Foundation under Grant No. IIP-1114275 and work supported by NYSERDA under Grant No. 18507. NYSERDA has not reviewed the information

contained herein, and the opinions expressed in this report do not necessarily reflect those of NYSERDA or the State of New York. This work made use of the Cornell Center for Materials Research Shared Facilities which are supported through the NSF MRSEC program (DMR-1120296). We acknowledge P. Huang, R. Hovden, and J. Mundy of Cornell University for help with the TEM imaging. The Austrian Science Funds FWF (project number I449) is acknowledged for financial support.

REFERENCES

1. Kumar, S. K.; Krishnamoorti, R. Nanocomposites: Structure, Phase Behavior, and Properties. *Annu. Rev. Chem. Biomol. Eng.* **2010**, *1*, 37–58.

2. Mackay, M. E.; Tuteja, A.; Duxbury, P. M.; Hawker, C. J.; Horn, B. Van; Guan, Z.; Chen, G.; Krishnan, R. S. General Strategies for Nanoparticle Dispersion. *Science* **2006**, *311*, 1740–1743.

3. Winey, K. I.; Vaia, R. A. Polymer Nanocomposites. *MRS Bull.* **2011**, *32*, 314–322.

4. Podsiadlo, P.; Kaushik, A. K.; Arruda, E. M.; Waas, A. M.; Shim, B. S.; Xu, J.; Nandivada, H.; Pumplin, B. G.; Lahann, J.; Ramamoorthy, A. *et al.* Ultrastrong and Stiff Layered Polymer Nanocomposites. *Science* **2007**, *318*, 80–83.

5. Akcora, P.; Kumar, S. K.; Moll, J.; Lewis, S.; Schadler, L. S.; Li, Y.; Benicewicz, B. C.; Sandy, A.; Narayanan, S.; Ilavsky, J. *et al.* "Gel-like" Mechanical Reinforcement in Polymer Nanocomposite Melts. *Macromolecules* **2010**, *43*, 1003–1010.

6. Voevodin, A. A; Vaia, R. A; Patton, S. T.; Diamanti, S.; Pender, M.; Yoonessi, M.; Brubaker, J.; Hu, J.-J.; Sanders, J. H.; Phillips, B. S. *et al.* Nanoparticle-wetted Surfaces for Relays and Energy Transmission Contacts. *Small* **2007**, *3*, 1957–1963.

7. Kim, D.; Archer, L. A. Nanoscale Organic-Inorganic Hybrid Lubricants. *Langmuir* **2011**, *27*, 3083–3094.

8. Bremer, L.; Tuinier, R.; Jahromi, S. High Refractive Index Nanocomposite Fluids for Immersion Lithography. *Langmuir* **2009**, *25*, 2390–2401.

9. Nugent, J. L.; Moganty, S. S.; Archer, L. A. Nanoscale Organic Hybrid Electrolytes. *Adv. Mater.* **2010**, *22*, 3677–3680.

10. Lin, K.-Y. A.; Park, A.-H. A. Effects of Bonding Types and Functional Groups on CO2 Capture Using Novel Multiphase Systems of Liquid-like Nanoparticle Organic Hybrid Materials. *Environ. Sci. Technol.* **2011**, *45*, 6633–6639.

11. Corbierre, M. K.; Cameron, N. S.; Lennox, R. B. Polymer-stabilized Gold Nanoparticles with High Grafting Densities. *Langmuir* **2004**, *20*, 2867–2873.

12. Goel, V.; Pietrasik, J.; Dong, H.; Sharma, J.; Matyjaszewski, K.; Krishnamoorti, R. Structure of Polymer Tethered Highly Grafted Nanoparticles. *Macromolecules* **2011**, *44*, 8129–8135.

13. Zhang, Q.; Archer, L. A. Poly(ethylene oxide)/Silica Nanocomposites: Structure and Rheology. *Langmuir* **2002**, *18*, 10435–10442.

14. Ohno, K.; Morinaga, T.; Koh, K.; Tsujii, Y.; Fukuda, T. Synthesis of Monodisperse Silica Particles Coated with Well-Defined, High-Density Polymer Brushes by Surface-Initiated Atom Transfer Radical Polymerization. *Macromolecules* **2005**, *38*, 2137–2142.

15. Ghosh Chaudhuri, R.; Paria, S. Core/shell Nanoparticles: Classes, Properties, Synthesis Mechanisms, Characterization, and Applications. *Chem. Rev.* **2012**, *112*, 2373–2433.

16. Akcora, P.; Liu, H.; Kumar, S. K.; Moll, J.; Li, Y.; Benicewicz, B. C.; Schadler, L. S.; Acehan, D.; Panagiotopoulos, A. Z.; Pryamitsyn, V. *et al.* Anisotropic Self-assembly of Spherical Polymer-grafted Nanoparticles. *Nat. Mater.* **2009**, *8*, 354–359.

17. Moganty, S. S.; Jayaprakash, N.; Nugent, J. L.; Shen, J.; Archer, L. A. Ionic-Liquid-Tethered Nanoparticles: Hybrid Electrolytes. *Angew. Chem. Int. Ed. Engl.* **2010**, *122*, 9344–9347.

18. Bhattacharjee, R. R.; Li, R.; Estevez, L.; Smilgies, D.-M.; Amassian, A.; Giannelis, E. P. A Plasmonic Fluid with Dynamically Tunable Optical Properties. *J. Mater. Chem.* **2009**, *19*, 8728-8731.

19. Warren, S. C.; Banholzer, M. J.; Slaughter, L. S.; Giannelis, E. P.; DiSalvo, F. J.; Wiesner, U. B. Generalized Route to Metal Nanoparticles with Liquid Behavior. *J.Amer. Chem. Soc.* **2006**, *128*, 12074–12075.

20. Sun, L.; Fang, J.; Reed, J. C.; Estevez, L.; Bartnik, A. C.; Hyun, B.-R.; Wise, F. W.; Malliaras, G. G.; Giannelis, E. P. Lead-salt Quantum-dot Ionic Liquids. *Small* **2010**, *6*, 638–641.

21. Bourlinos, A. B.; Stassinopoulos, A.; Anglos, D.; Herrera, R.; Anastasiadis, S. H.; Petridis, D.; Giannelis, E. P. Functionalized ZnO Nanoparticles with Liquidlike Behavior and Their Photoluminescence Properties. *Small* **2006**, *2*, 513–516.

22. Bourlinos, A. B.; Giannelis, E. P.; Zhang, Q.; Archer, L. A.; Floudas, G.; Fytas, G. Surface-functionalized Nanoparticles with Liquid-like Behavior: The Role of the Constituent Components. *Eur. Phys. J. E. Soft Matter* **2006**, *20*, 109–117.

23. Rodriguez, R.; Herrera, R.; Bourlinos, A. B.; Li, R.; Amassian, A.; Archer, L. A.; Giannelis, E. P. The Synthesis and Properties of Nanoscale Ionic Materials. *Appl. Organomet. Chem.* **2010**, *24*, 581–589.

24. Perriman, A. W.; Cölfen, H.; Hughes, R. W.; Barrie, C. L.; Mann, S. Solvent-free Protein Liquids and Liquid Crystals. *Angew. Chem. Int. Ed. Engl.* **2009**, *48*, 6242–6246.

25. Fernandes, N.; Dallas, P.; Rodriguez, R.; Bourlinos, A. B.; Georgakilas, V.; Giannelis, E. P. Fullerol Ionic Fluids. *Nanoscale* **2010**, *2*, 1653–1656.

26. Bourlinos, A. B.; Herrera, R.; Chalkias, N.; Jiang, D. D.; Zhang, Q.; Archer, L. A.; Giannelis, E. P. Surface-Functionalized Nanoparticles with Liquid-Like Behavior. *Adva. Mater.* **2005**, *17*, 234–237.

27. Bourlinos, A. B.; Ray Chowdhury, S.; Herrera, R.; Jiang, D. D.; Zhang, Q.; Archer, L. A.; Giannelis, E. P. Functionalized Nanostructures with Liquid-Like Behavior: Expanding the Gallery of Available Nanostructures. *Adv. Funct. Mater.* **2005**, *15*, 1285–1290.

28. Koning, C.; Duin, M. Van; Pagnoulle, C.; Jerome, R. Strategies for Compatibilization of Polymer Blends. *Prog. Polym. Sci.* **1998**, *23*, 707–757.

29. Wang, Z.-G. Chain Dimensions in Amorphous Polymer Melts. *Macromolecules* **1995**, *28*, 570–576.

30. Allen, L. H.; Matijevic, E. Stability of Colloidal Silica. *J. Colloid. Interface. Sci.* **1970**, *33*, 420–429.

31. Allen, L. H.; Matijevic, E.; Meites, L. Exchange of Na^+ for the Silanolic Protons of Silica. *J. Inorg. Nucl. Chem.* **1971**, *33*, 1293–1299.

32. Iler, R. K. *The Chemistry of Silica*; John Wiley & Sons, Inc.: New York, 1979; p. 865.

33. Leung, K.; Nielsen, I. M. B.; Criscenti, L. J. Elucidating the Bimodal Acid-base Behavior of the Water-silica Interface from First Principles. *J. Amer. Chem. Soc.* **2009**, *131*, 18358–18365.

34. Rosenholm, J. M.; Czuryszkiewicz, T.; Kleitz, F.; Rosenholm, J. B.; Lindén, M. On the Nature of the Brønsted Acidic Groups on Native and Functionalized Mesoporous Siliceous SBA-15 as Studied by Benzylamine Adsorption from Solution. *Langmuir* **2007**, *23*, 4315–4323.

35. Madathingal, R. R.; Wunder, S. L. Confinement Effects of Silica Nanoparticles with Radii Smaller and Larger Than R g of Adsorbed Poly(ethylene Oxide). *Macromolecules* **2011**, *44*, 2873–2882.

36. Mathur, S.; Moudgil, B. Adsorption Mechanism(s) of Poly(Ethylene Oxide) on Oxide Surfaces. *J. Colloid. Interface. Sci.* **1997**, *196*, 92–98.

37. Brunner-Popela, J.; Mittelbach, R.; Strey, R.; Schubert, K.-V.; Kaler, E. W.; Glatter, O. Small-angle Scattering of Interacting Particles. III. D_2O-$C_{12}E_5$ Mixtures and Microemulsions with N-octane. *J. Chem. Phys.* **1999**, *110*, 10623-10632.

38. Freltoft, T.; Kjems, J.; Sinha, S. Power-law Correlations and Finite-size Effects in Silica Particle Aggregates Studied by Small-angle Neutron Scattering. *Phys. Rev. B* **1986**, *33*, 269–275.

39. Teixeira, J. Small-angle Scattering by Fractal Systems. *J. Appl. Crystallogr.* **1988**, *21*, 781–785.

40. Brunner-Popela, J.; Glatter, O. Small-Angle Scattering of Interacting Particles. I. Basic Principles of a Global Evaluation Technique. *J. Appl. Crystallogr.* **1997**, *30*, 431–442.

41. Weyerich, B.; Brunner-Popela, J.; Glatter, O. Small-angle Scattering of Interacting Particles. II. Generalized Indirect Fourier Transformation Under Consideration of the Effective Structure Factor for Polydisperse Systems. *J. Appl. Crystallogr.* **1999**, *32*, 197–209.

42. Hayter, J. B.; Penfold, J. An Analytic Structure Factor for Macroion Solutions. *Mol. Phys.* **1981**, *42*, 109–118.

43. Hansen, J.-P.; Hayter, J. B. A Rescaled MSA Structure Factor for Dilute Charged Colloidal Dispersions. *Mol. Phys.* **1982**, *46*, 651–656.

44. Srivastava, S.; Shin, J. H.; Archer, L. A. Structure and Rheology of Nanoparticle–polymer Suspensions. *Soft Matter* **2012**, *8*, 4097--4108.

45. Dukes, D.; Li, Y.; Lewis, S.; Benicewicz, B. C.; Schadler, L.; Kumar, S. K. Conformational Transitions of Spherical Polymer Brushes: Synthesis, Characterization, and Theory. *Macromolecules* **2010**, *43*, 1564–1570.

46. Yu, H.-Y.; Koch, D. L. Structure of Solvent-free Nanoparticle-organic Hybrid Materials. *Langmuir* **2010**, *26*, 16801–16811.

47. Goel, V.; Pietrasik, J.; Matyjaszewski, K.; Krishnamoorti, R. Linear Viscoelasticity of Spherical SiO 2 Nanoparticle-Tethered Poly(butyl Acrylate) Hybrids. *Ind. Eng. Chem. Res.* **2010**, *49*, 11985–11990.

48. Jespersen, M. L.; Mirau, P. A.; Meerwall, E. von; Vaia, R. A.; Rodriguez, R.; Giannelis, E. P. Canopy Dynamics in Nanoscale Ionic Materials. *ACS Nano* **2010**, *4*, 3735–3742.

49. Chremos, A.; Panagiotopoulos, A. Z.; Koch, D. L. Dynamics of Solvent-free Grafted Nanoparticles. *J. Chem. Phys.* **2012**, *136*, 044902-1—044902-9.

50. Goyal, S.; Escobedo, F. A Structure and Transport Properties of Polymer Grafted Nanoparticles. *J. Chem. Phys.* **2011**, *135*, 184902-1—184902-12.

CHAPTER 3

CANOPY STRUCTURE AND PROPERTIES IN NANOPARTICLE IONIC MATERIALS

4.1 Introduction

Much attention has been focused recently on the use of "hairy" nanoparticles as an avenue to overcome dispersion challenges in polymer nanocomposites.[1] A subset of hairy nanoparticles are Nanoparticle Ionic Materials (NIMs), which rely on ionic charges on the particles and end-functionalized polymers to form hairy particles in a facile manner.[2–4] Synthesis of NIMs has strong analogies with the grafting-to methods used to create other (covalently grafted or physisorbed) hairy nanoparticles, as the synthesis involves an ionic interaction between charged groups on the nanoparticle surface and the end of the polymer. Understanding the effect of graft density, polymer molecular weight, and the multilayer transition is therefore essential to creating a framework that allows the creation of NIMs by design. For example, NIMs have been studied for gel electrolytes for lithium ion batteries[5], and for lubricant applications.[6] Flow behavior is critical in both these applications, and thus having a clear understanding of the effect of graft density and canopy molecular weight is essential in order to tailor the materials to their intended function.

There are three major barriers to arbitrarily high grafting densities.[7] The first is the maximum geometrically possible graft density, also referred to as the parking area of the incoming polymer. Another barrier is entropic, and arises from the conformation of the polymers in the brush. As the graft density increases, the volume available to each polymer chain decreases, forcing them to adopt a longitudinally stretched and laterally constrained conformation. This reduction in volume leads to a reduction in entropy available for the system.[8] Finally it has been shown that the graft reaction for other "grafting-to" systems proceeds to completion in logarithmic time, since the barrier to additional polymers reaching the surface is kinetic as well as thermodynamic.[9]

In the class of NIMs considered here, the nanoparticles are first functionalized by a strong ionic group, such as the sulfonate group (Figure 4.1).[3] These groups are then reacted with a corresponding basic group (such as the amine group) on the end of the canopy polymer.

$$\text{(Particle)-AH + B-Polymer} \rightarrow \text{(Particle)-A}^{-}\cdots^{+}\text{HB-Polymer}$$

With the correct choice of ionic groups, this reaction can be driven to the right. Figure 3.2 shows the titration curve when an amine terminated poly(ethylene oxide) (PEO)is attached to a dispersion of silica functionalized with sulfonic acid groups. The titration curve can be interpreted in terms of an effective graft density σ_{Eff} , as seen by the secondary axis. Remarkably, σ_{Eff} at the endpoint of the titration (where the pH passes through neutrality) is very high. Not only does it exceed previously reported grafting densities in the "grafting to" or indeed even "grafting from" systems, it exceeds the maximum geometric grafting density. This is a consequence of the ionic nature of the reaction; since water has a high dielectric constant, it can support the ions that are formed even though many of the polymer chains must be spatially distant from the particle surface.

This seeming contradiction is resolved by a multilayer "onion" model where an inner layer is directly grafted, while the outer layers are held in place by (partly screened) electrostatic interactions. This model has been verified by pulsed-field gradient NMR experiments by Jespersen et al., who showed that while free polymer has a single slightly stretched diffusion time, ionically bound polymer chains exhibits two diffusion times – a fast time that is somewhat slower than the time for free polymers, and a slow time attributed to the inner layer of polymer.[10,11] In the same study, they have verified the ionic nature of the coupling by showing that the diffusion of this inner layer can be sped up by adding salts to the system, screening the charge and reducing the barrier for decoupling the polymer chains from the particle.[12]

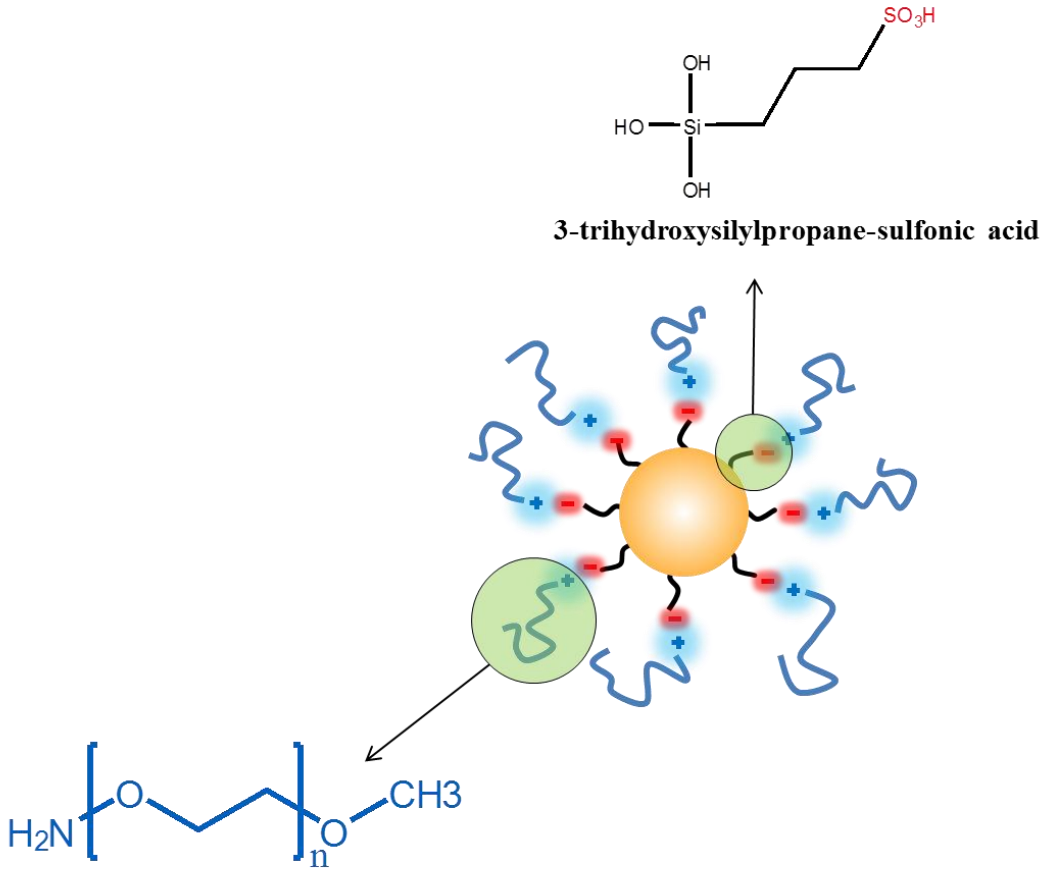

Figure 4.1: A schematic of the Nanoparticle Ionic Material used in this study.

The threshold value for the graft density is expected to have a significant effect on the thermal and mechanical properties of NIMs. As Jespersen and coworkers have demonstrated, the high diffusivity of the polymer in the outer layers leads to a lower viscosity for the bulk material. Additionally, a number of works have shown that the confinement of polymers near the particle has an effect on its thermal properties. In this study, the effect of molecular weight and graft density on the properties of silica/poly(ethylene oxide) NIMs are systematically studied, with a view towards creating a phase map that will inform synthesis by design for future applications.

4.2 Materials and Methods

Sulfonic acid functionalized silica was prepared by a previously reported method.[3] Briefly, Ludox HS-30 silica (Sigma Aldrich, 30% w/w in water) was diluted in de-ionized and added dropwise under stirring to a solution of 3-(trihydroxysilyl) propanesulfonic acid (Gelest, 30% w/w in water) in the ratio of 2g of silane to 1g of silica particles., and the pH was raised to ~5 by dropwise addition of aqueous 1M NaOH (Sigma Aldrich). The solution was then sealed and allowed to react at 70°C for 48 hours. The unreacted silane was removed by dialysis in a Thermo/Fisher SpectraPor dialysis membrane (MWCO 25,000) with an effective solution: bath volume of 200:1 over 5 days (where the water was changed every day). Finally, the resulting material was poured over a cation exchange resin (Dowex Marathon C) to remove residual sodium ions. The concentration of the resulting dispersion was determined by drying an aliquot. The resulting sulfonated silica had an acid activity of 1.52 mmol/g, as determined by titration (Figure 3.2).

Amine-terminated poly(ethylene oxide) (mPEG-NH_2) was obtained from Laysan Bio in a number of molecular weights (2 kDa, 5 kDa, 10 kDa, 20 kDa, 30 kDa). To synthesize a hybrid material, an appropriate amount of the mPEG-NH2 was diluted in deionized water to form a 4%

w/w solution, and then mixed with an appropriate amount of the silica dispersion. The vial was agitated violently for 12 hours in a shaking table, and then all water was removed by immersing the vial in liquid nitrogen to freeze it rapidly, and then extracting the water by sublimation in a lyophilizer (condenser temperature -40C, vacuum ~ 250 μbar). The resulting material was annealed/degassed under vacuum at 75°C (above the melting point of PEG) for 24 hours. Table 4.1 shows the weight fraction of silica in each sample.

Dynamic Light Scattering was carried out on all samples in water at 25°C using a Malvern Zetasizer. In each case, the concentration of the sample was less than 1% to ensure that interactions such as depletion effects and clustering did not play a role.

All rheological experiments were carried out at 75°C. In a typical experiment, a small amount of sample was placed to completely fill the gap between the two plates of an Anton-Paar Physica rheometer, and the excess sample was trimmed away. An initial constant shear rate of 10 s^{-1} was imposed to homogenize the sample, followed by a pause to allow internal stresses to dissipate. For more solid samples, a normal force of 40N was applied for an hour before being released in order to fully pack the sample. Various methods of probing the behavior of the sample were used and will be discussed.

Differential Scanning Calorimetry was used to determine phase transitions in the hybrids by measuring heat flow as a function of temperature. Between 2 and 5 milligrams of each sample was loaded into TZero™ hermetically sealed pan. The samples were heated and cooled at 3 °C/min, and the second heating curve was analyzed in order to maintain all samples at a consistent thermal history.

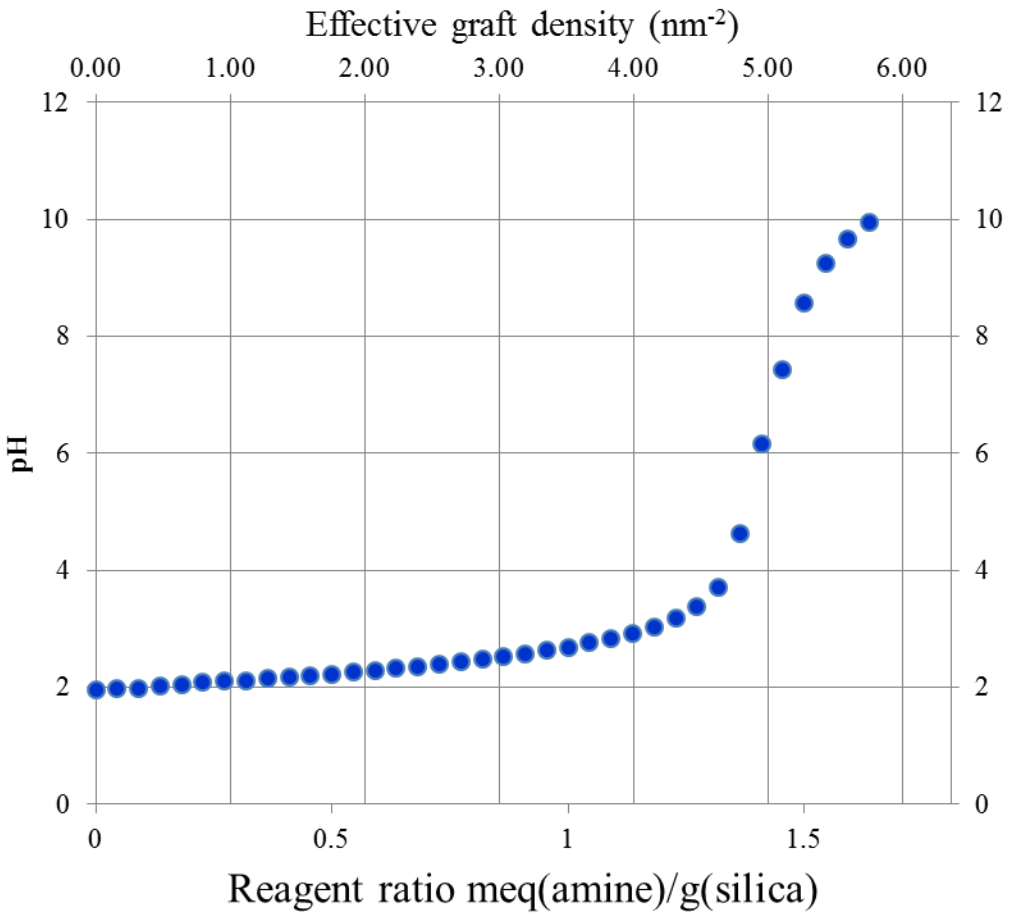

Figure 4.2: Titration curve for sulfonated silica vs. amine, showing the equivalent point. The upper axis displays the equivalent grafting density at each point.

		Molecular Weight				
		2000	5000	10000	20000	30000.00
Graft density	0.10	0.946	0.876	0.779	0.638	0.541
	0.17	0.909	0.799	0.665	0.498	0.398
	0.31	0.848	0.691	0.528	0.358	0.271
	0.56	0.758	0.557	0.386	0.239	0.173
	1.0	0.638	0.414	0.261	0.150	0.105
	1.7	0.498	0.284	0.166	0.090	0.062
	3.1	0.358	0.183	0.100	0.053	0.036
	5.6	0.239	0.112	0.059	0.030	0.021
	7.8	0.185	0.083	0.043	0.022	0.015
	10	0.150	0.066	0.034	0.017	0.012

Table 4.1: Particle weight fraction as a function of effective graft density and molecular weight for the samples studied.

4.3 General Discussion:

Building from the Daoud-Cotton model for star polymers, while accounting for the finite radius of curvature of the nanoparticle surface, Fukuda and coworkers have derived a model that describes several regimes for the polymer structure at the surface of the nanoparticle. While their results were calculated for dilute solutions of polymers, the behavior is expected to hold for melts, due to the Flory principle that a polymer melt is equivalent to a solution in a theta solvent.[13–15]

For low graft densities the polymer is "pancaked" onto the particle. As the graft density increases, the brush begins to stretch away when $\left(2R_g \leq \frac{1}{\sigma}\right)$ to form a semi-dilute brush (SDPB).

The portion of the chain nearest the surface is stretched to form a concentrated polymer brush (CPB) The CPB region grows as σ increases. Since the available volume per polymer chain increases away from the surface, there is a transition radius between the CPB and SDPB (assuming the polymer is long enough to enter this regime) is given by:

$$R_C = R_{CORE}\frac{\sigma^{1/2} l_0 \sqrt{4\pi}}{\frac{1}{2} - \chi} \qquad (1)$$

Where R_{CORE} is the particle radius, σ is the grafting density, l_0 is the monomer size, and χ is the Flory polymer-solvent interaction parameter (χ = 0 for polymer melts). The height of the brush is given by solution to:

$$\frac{h}{H_0}\left(1 + \frac{3h}{4\omega H_0} + \frac{1}{5}\left(\frac{h}{\omega H_0}\right)^2\right) = 1 \qquad (2)$$

Where $\omega = \frac{R_{CORE}}{H_0}$ and $H_0 = \left(\frac{8}{\pi}\left(\frac{1}{2} - \chi\right)\sigma\right)^{\frac{1}{3}} l_0^{\frac{5}{3}} N$ is the unperturbed brush length on a flat surface. While this model has been shown to be only approximate, it is believed to capture the essence of the behavior of the brush.

There are thus a number of distinct regimes for the particle-polymer system, as summarized in Figure 4.3. They are:

$\boldsymbol{2R_g < 1/\sigma}$**:** The polymer is in the "pancaked" regime.

$\boldsymbol{R_{CORE} > R_C}$**,:** The polymer is in the flexible SDPB regime (i.e, the transition radius is "inside" the particle).

$\boldsymbol{R_{CORE} + h > R_C}$**:** The inner portion of each polymer is in CPB, while the outer portion is in SDPB.

$\boldsymbol{R_{CORE} + h < R_C}$**:** All the polymer is in the CPB regime.

$\boldsymbol{\sigma > \sigma_C}$**:** The system enters the multilayer regime.

Finally, there is $\boldsymbol{\sigma > \sigma_{MAX}}$: There is excess polymer that is not associated with the particle. In our case, this situation arises when the acidic capacity of the particle has been exceeded.

Once the graft density exceeds the threshold value σ_C, additional polymers cannot access the surface of the particle, but are still held in place by electrostatic attractions. This graft threshold is difficult to calculate directly, since it depends on a wide range of variables, including the energy of interaction and the reaction conditions (time, concentration of each component, etc.).[7] However, following Oyerokun and Vaia, it is possible to argue that, with all other factors held constant, the grafting-to reaction proceeds until the binding energy of the interaction no longer offsets the loss of entropy of the polymer as it leaves the solution and enters the canopy. Since the entropy of a random coil in solution scales as 1/N, as a first approximation, the

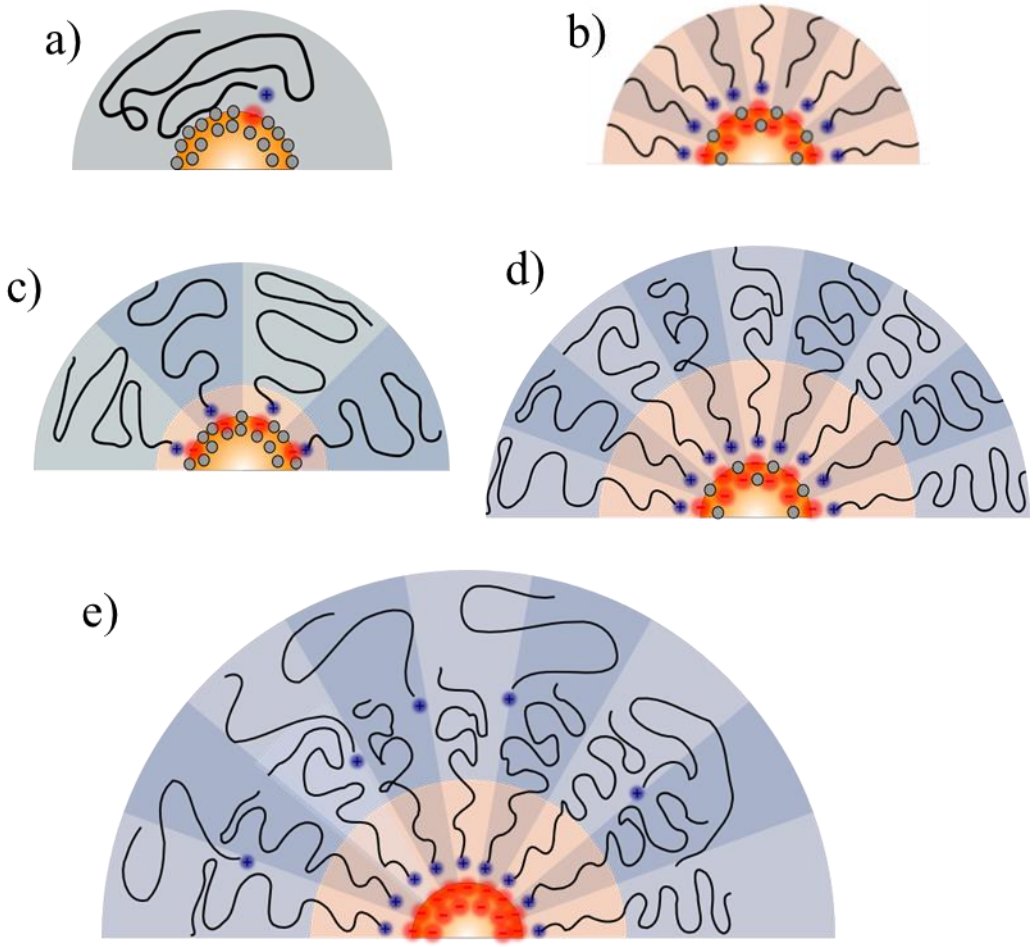

Figure 4.3: Predicted behavior of the canopy with graft density and molecular weight variations. (a) "pancaked." (b) CPB only. (c) SDPB only. (d) CPB transitioning to SDPB. (e) Multilayered canopy.

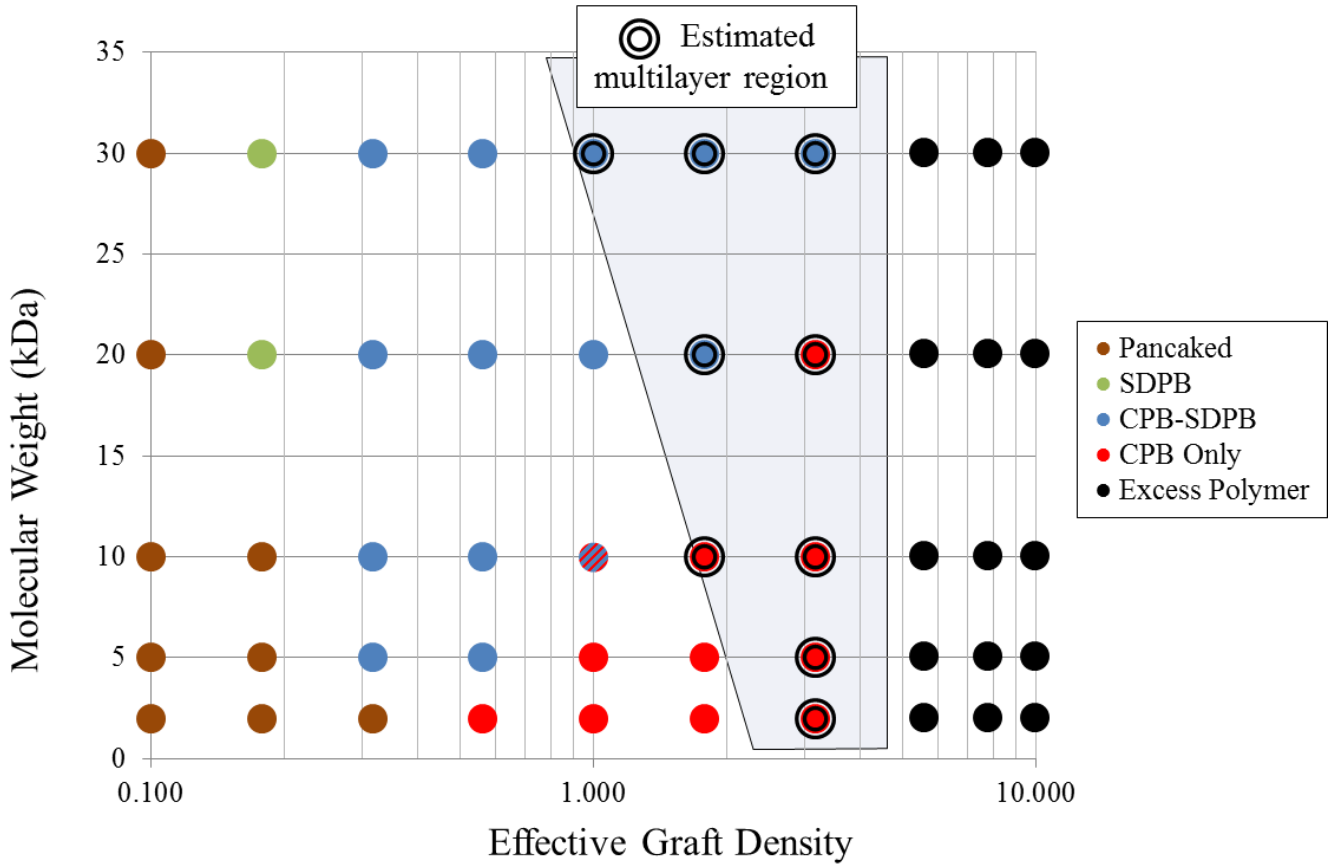

Figure 4.4: Predicted phase map of calculated canopy behavior for the samples studied from theory. The estimated region of a multilayer canopy is depicted by the shaded area and the double line around the symbol.

maximum graft density can also be expected, as a zero-order approximation, to scale accordingly.

A number of studies of grafting-to type reactions report varying grafting densities, ranging from 0.1 to approximately 2 nm^{-2}.[6,16–22] The most relevant is the study by Agarwal *et al.*, which also utilizes a similar system, with the same amine-sulfonate interactions, and the same poly(ethylene oxide) backbone.[16] The maximum grafting density achieved for a 5000 MW polymer was 2.2 nm^{-2} in a system where thorough washing could be argued to have driven off the outer, weakly bound layers. Thus, it is possible to estimate this region based on the proportion of the canopy in the CPB regime, as the loss of entropy is significantly less for the portion of the canopy in the SDPB regime.

All these regions have been summarized in a phase map in Figure 4.4, where each point has been color coded according to the expected conformation for that sample. The expected multilayer region has been shaded, based on literature reports of the largest graft densities seen in comparable systems as well as an approximate scaling argument discussed above. The location of this region is based on speculation, but as seen below, it is possible to get a more accurate estimate for its onset.

In the sections to follow, various experimental techniques are used to interrogate samples in this phase diagram.

4.4 Dynamic Light Scattering

Dynamic Light Scattering (DLS) monitors the fluctuation of intensity of laser light that is scattered from a solution of particles due to their Brownian motion through a solvent. In the case of the instrument used, backscattered light was used. The second-order autocorrelation of the sample $g_2(q,\tau) = \frac{\langle I(t)I(t+\tau)\rangle}{\langle I(t)\rangle^2}$ is extracted, and from that, the first order autocorrelation $g_1(\tau) =$

$\sqrt{\frac{g_2(\tau)-1}{\beta}}$ is calculated. From this equation, an approximate decay rate $\Gamma = q^2 D_t$ is calculated, where $g_1(\tau, q) = e^{-\Gamma\tau}$, and D_t is the translational diffusion coefficient. Thus, using the Stokes-Einstein equation, an approximate hydrodynamic diameter can be calculated.[23] Note that this is effectively the collision diameter of the particle/polymer hybrid, and includes all ions associated with the particle. The resulting estimated canopy height $h_{DLS} = \frac{D-2R_{CORE}}{2}$ is plotted as a function of graft density in figure 4.5. There are two features to note here. The first is that above an effective graft density of $\sigma = 5$ nm^{-2}, the canopy height reaches a plateau value. This plateau can be related to the titration curve shown in Figure SDF by noting that above this graft density, the pH has risen to the point that any additional polymer will not ionize. Therefore, additional polymer molecules will not associate with the particle, and the true graft density has reached its maximum.

Secondly, h_{DLS} increases rapidly after a threshold value of the graft density σ_T which varies with molecular weight. This is especially evident in the points for the 20 kDa and 30kDa series. This finding suggests that this is the point at which additional polymer is no longer able to directly access the surface of the particle, and is forced to remain in outer layers, still associated with the particle, but much more loosely conformed and with a greater fluctuation in distance.

Figure 4.6 shows the variation in size for the 20 kDa polymer, along with calculated values for Equation (2), using the appropriate parameters ($\chi_{WATER\text{-}PEO} = 0.24$[24], $l_0 = 0.37$ nm). The predicted value is offset, but appears to scale appropriately until $\sigma = 2.5$ nm^{-2}, at which point the measured values become much greater than the predicted values. This breakdown in the scaling can be attributed to the multi-layer formation discussed above.

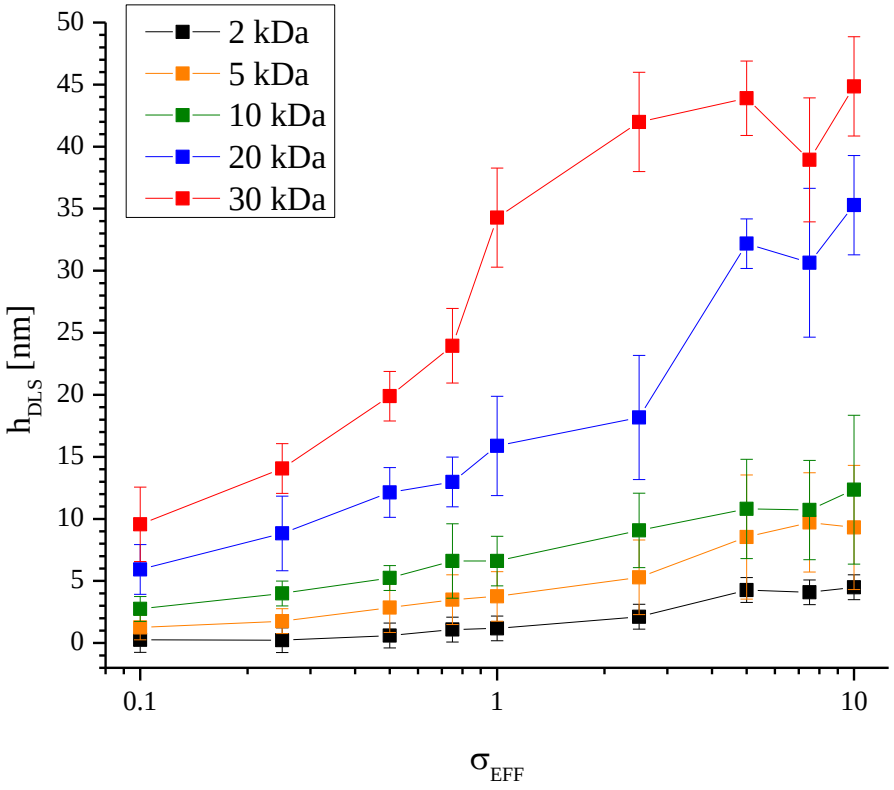

Figure 4.5: Dynamic light scattering results for varied molecular weights and effective graft density. Note the plateauing of the system at graft densities greater than 5.

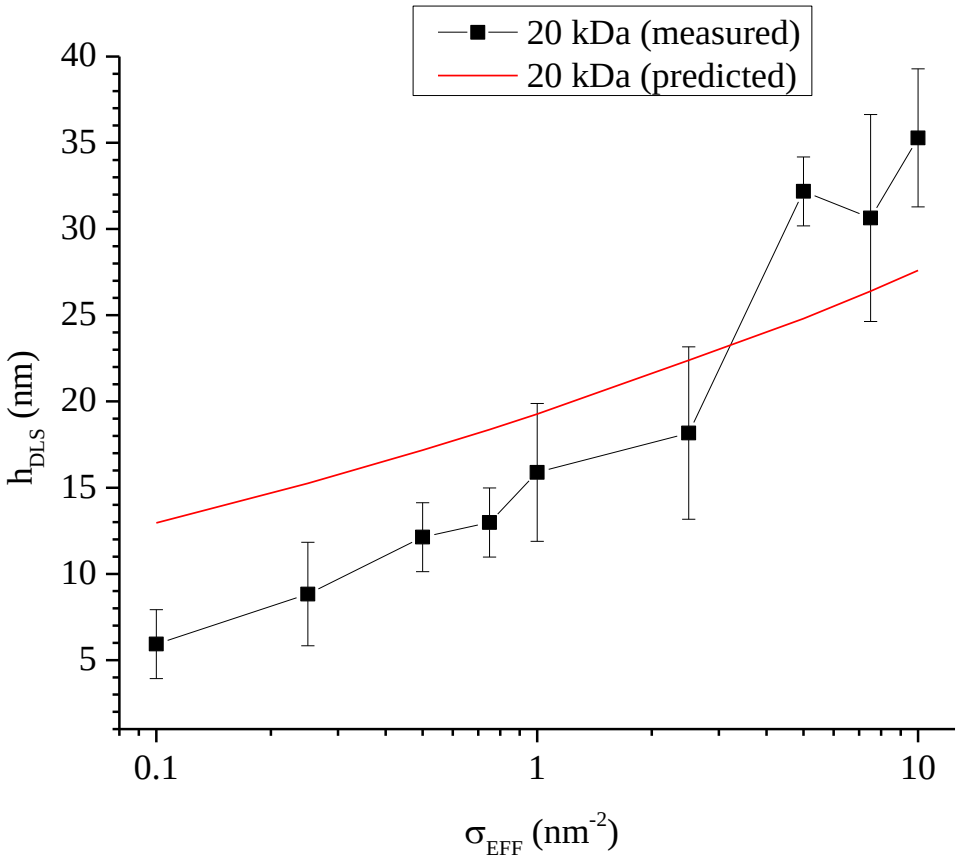

Figure 4.6: Measured change in canopy height for 20 kDa canopy, as well as a predicted value from the model discussed above. Note the divergence at an effective graft density of about 2.

4.5 Rheology

When heated to 75 °C (above the melting point of PEO), samples exhibited a range of behavior – some melted entirely, some softened, and others remained essentially unchanged. All rheology was carried out at 75°C to ensure that the dynamics of the polymer were not frozen.

The stability of the particle/polymer system against aggregation of nanoparticles is shown by carrying out rotational shear experiments, where the upper plate of the rheometer was moved at defined, increasing shear rate $\dot{\gamma}$, and the torque T (and thus the shear stress on the sample) required was monitored. From this experiment, the viscosity as a function of shear rate $\eta(\dot{\gamma})$ can be calculated. Not all samples were suitable for characterization, as more brittle samples were simply expelled from between the plates, but in the rest, two behaviors were seen – either $\eta(\dot{\gamma})$ was independent of $\dot{\gamma}$, indicating a Newtonian fluid, or $\eta(\dot{\gamma})$ decreased with increasing $\dot{\gamma}$, indicating a shear-thinning fluid. Both these indicate a stable dispersion of particles, with shear-thinning suggesting that some energy was required to break down some inherent structure in the system before free flow.[25,26] This behavior is contrasted, for example, with silica particles in ionic liquids, which show flocculation behavior exhibited by shear thickening of the suspension, leading to a rise in viscosity as a function of shear rate.[27,28]

To further characterize the materials, an oscillating amplitude strain of the form $\gamma(t) = \gamma_0 \sin \omega t$ is imposed and the shear stress is measured. The response can be written as $\tau(t) = \tau_0(\omega) \sin[\omega t + \delta(\omega)] = \gamma_0[G'(\omega) \sin \omega t + G''(\omega) \cos \omega t]$, where G' is the storage modulus, which is a measure of the energy stored in the system, and G'' is the loss modulus, which is a measure of the energy lost in the system due to dissipation.

Two distinct responses are seen in the samples studied (examples shown in figure 4.7(a)). For liquid samples, G''>G' over the whole range tested. These materials are (at this temperature)

observed to flow slowly. For more solid samples, three regions can be seen – i) a solid-like response at low strain in the linear viscoelastic region (LVE), ii) a region where G' decreases while G'' increases to a maximum, and iii) a region where G''>G' and both decrease, also known as shear melting. In all samples, these are the only two classes of behavior noted. The peak in G'' indicates the presence of a jammed (soft glassy) material, with the strength of the peak corresponding to the energetic barrier that has to be surmounted to break the jamming.[16,19,21] As seen in Figure 4.7(b), the strength of the peak increases with decreasing graft density for a given molecular weight.

Finally, a sample was classified as "powdery" when it was unable to maintain its cohesion when lifted gently from the bottom plate of the rheometer. These powdery materials also display the peak in G'' mentioned above.

Figure 4.8 shows the LVE loss tangent $\tan\delta = \frac{G''}{G'}$ as a function of the volume fraction (a) and graft density (b) for each molecular weight. It can be seen that each molecular weight has a different liquid-solid transition ($\tan\delta = 1$) volume fraction, and the volume fraction at which a system becomes solid decreases with molecular weight. Note that lower molecular weight samples have a higher tan δ in the liquid region, indicating more fluidity with shorter polymers for a given core volume fraction. Simulations of covalently grafted hairy particles by Goyal and Escobedo, as well as by Chremos *et al.* suggest that fluidity in single layer canopy nanoparticle systems is caused by relaxed polymer chains in the semi-dilute brush regime being able to freely move in the interstices between the particles, thus suggesting that higher molecular weights should lead to more fluid samples.[29,30] The opposite is observed, suggesting that the fluidity of the samples is mediated by diffusive transport of the polymer, as suggested by Jespersen *et al.*

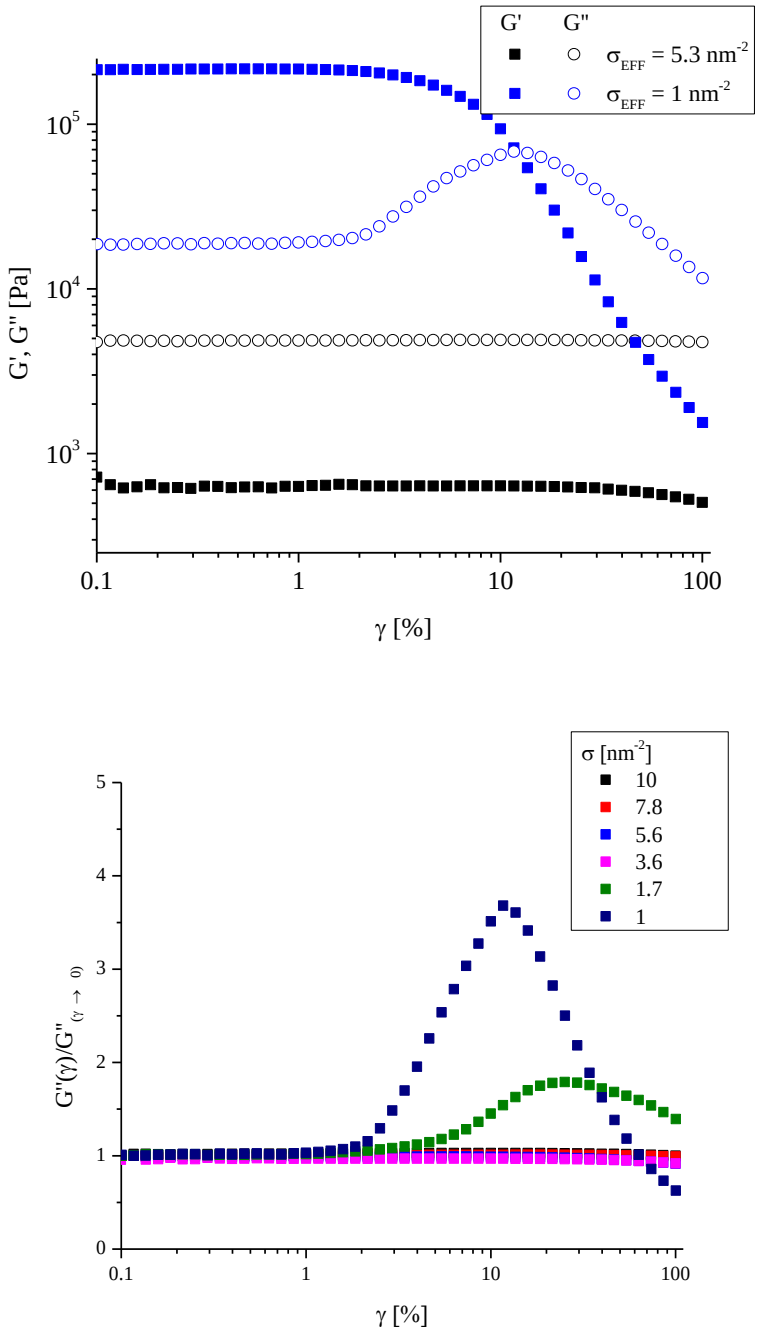

Figure 4.7: (a) examples of soft glassy and liquid behavior as seen by G',G'' strain sweeps, and (b) increase in the magnitude of the loss peak with decreasing graft density, indicating increased jamming.

A portion of the solid samples all have the same value of tan δ (0.05-0.07), independent of molecular weight. This subset of samples corresponds identically with the subset described as "powdery" earlier, suggesting that they are essentially completely jammed solids, with any measured G' purely arising from slippage of the rheometer plates over the upper surface of the sample.[31]

Using these three classifications (liquid, soft glass, powder) it is possible to construct a phase diagram of the behavior of the materials, as shown in Figure 3.9. The regions of fluid-like behavior occurs at somewhat higher effective graft densities than earlier hypothesized. In essence, the phase diagram is divided into three parts (summarized by the schematics above each section) – the portion where the excess polymer or multilayered canopy can act as a solvent, the region where the "hairy" particle is essentially jammed, and the region where the material is powdery because there is insufficient polymer to fill the interstitial spaces.

As the rheology phase diagram appears to support the hypothesis that liquid behavior occurs at the onset of the multilayer regime, it is possible to further refine the measurement to get a better estimate for this onset. From figure 4.8(a) the particle volume fraction $\phi(M)$ that shows the onset of jamming can be estimated, where M is the molecular weight of the canopy. Noting that the total volume fraction for jamming must be at $\varphi = \varphi_C = 0.63$, we can write:

$$\phi_{CORE} + \psi_{CANOPY} + \psi_{INTERSTITIAL} = 1 \quad (3)$$

and

$$\phi_{CORE} + \psi_{CANOPY} = \phi_C \quad (4)$$

where ψ represents the polymer volume fractions in the canopy and the interstices.

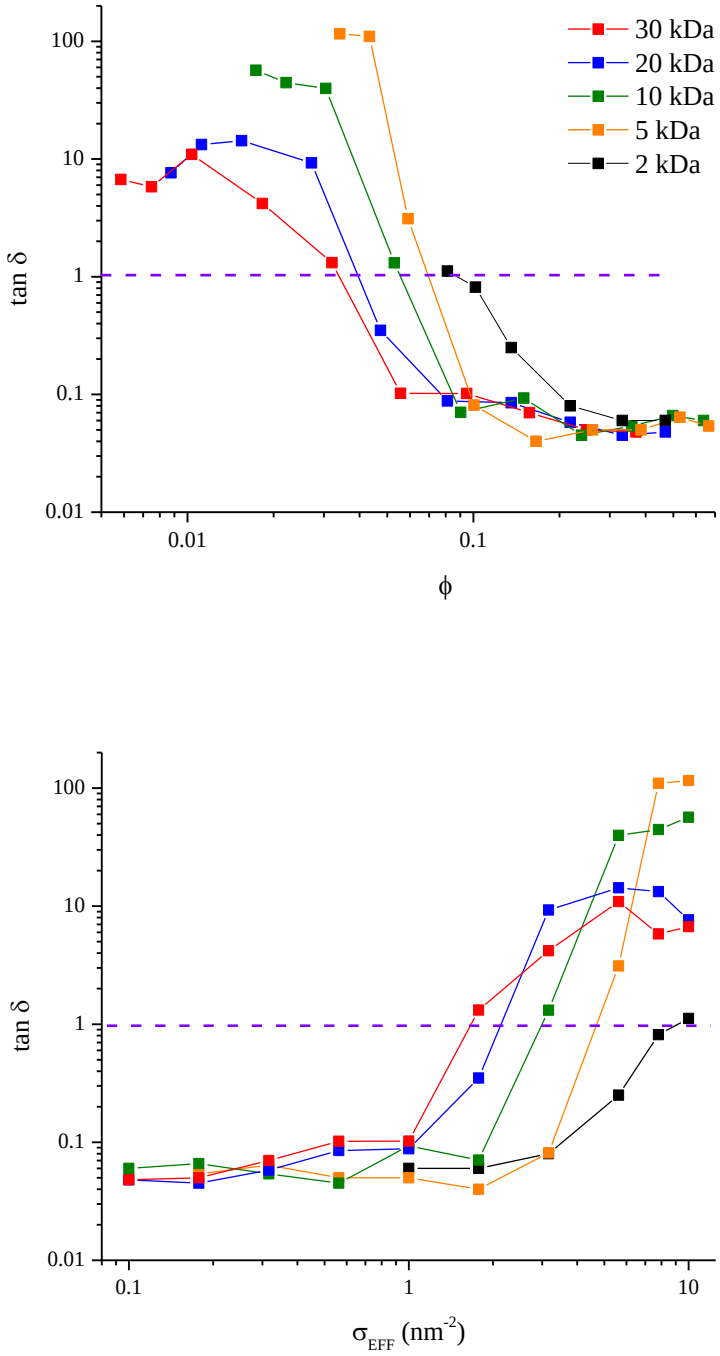

Figure 4.8: Damping factor as a function of (a) particle volume fraction, and (b) effective graft density.

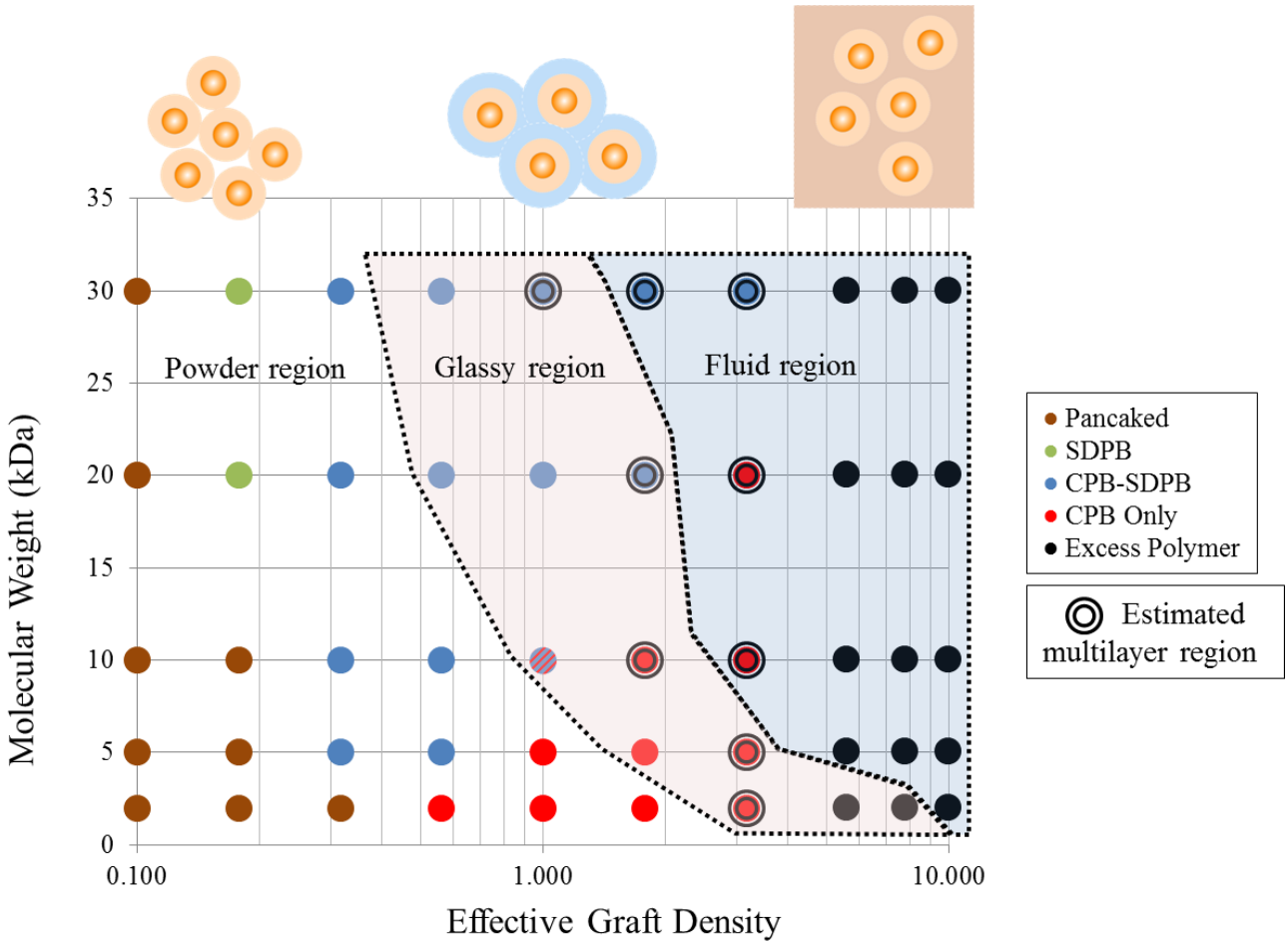

Figure 4.9: Phase diagram with an overlay showing the mechanical properties of the material. The cartoons above show the hypothetical morphology of the systems.

Molecular Weight (Da)	**φ**	**Indicated σ_{EFF} (nm^{-2})**	**Corrected σ_{EFF} (nm^{-2})**
30000	0.034	1.66	1.0
20000	0.04	2.14	1.3
10000	0.056	2.98	1.8
5000	0.070	4.69	2.8
2000	0.090	8.9	5.3

Table 4.2: Corrected effective graft densities for the onset for the multilayer effect, using a model suggesting jammed behavior in the particle system.

Now treating the particle and canopy system in isolation, the corrected volume fractions are given by rescaling the volume fractions to 0.63. Then the weight fraction of the particle can be calculated as

$$\alpha = \frac{\rho_{CORE}\phi}{\rho_{CORE}\phi + \rho_{POLY}(1-\phi)} \tag{5}$$

and

$$\sigma_{EFF} = \frac{R_{CORE}}{3}\frac{\rho_{CORE}N_A}{M}\left(\frac{1-\alpha}{\alpha}\right) \tag{6}$$

The calculated effective graft densities are tabulated in Table 4.2, and correspond well to values reported in the literature, as discussed above, for the maximum grafting density seen for a single layer. As the graft density increases beyond this point, the samples still exhibit jammed behavior, as the interstitial gaps are not completely full. The visible onset of fluid-like behavior occurs when all the interstices are full, which occurs at a higher apparent graft density.

It is important to note here that this change in behavior has been noted by Agarwal *et al.* as a transition from glassy to liquid behavior for a fraction of samples in that study, suggesting that this too was due to the onset of a multilayer canopy formation.[16] Further, while this behavior is apparently contradicted by earlier work that shows that a 20 kDa polymer grafted at 1 nm^{-2} on a 16 nm particle is actually a liquid, the earlier report was for a system with weaker Si-OH···H_2N-PEO bond which had arguably more hydrogen-bonding and less fully ionic character.[32] Thus the multilayer effect would be expected to start earlier in that system, showing fluidity at a lower grafting density.

4.6 Differential Scanning Calorimetry.

DSC allows the examination of the latent heat of melting of the polymeric portion of each sample. Second-heating DSC traces for a representative set of samples with canopy molecular

weight of 5 kDa are shown in Fig. 4.10. By integrating these curves over the downward (endothermic) peak of the melting of the polymer, the latent heat of the transition is obtained. The degree of crystallinity of the sample can then be calculated by correcting for the weight of the polymer in each sample, and then taking the ratio against the theoretical latent heat of fusion for the pure polymer ($\Delta H_{PEO} = 188$ J/g).[33]

$$\chi_C = \frac{1}{(1-\alpha)} \frac{\Delta H_{sample}}{\Delta H_{PEO}} \tag{7}$$

where α is the particle weight fraction. None of the samples achieved a degree of crystallinity of 1 – when the pure polymer was measured, it reached a maximum χ_C of 0.8 under these experimental conditions due to the finite cooling rate involved.

Figure 4.11 shows the degree of crystallinity as function of graft density (a), and polymer volume fraction ψ (b). In the latter plot, samples with negligible degrees of crystallinity have been omitted. The remaining samples, for molecular weights 5 kDa, 10kDa, 20kDa, and 30kDa, collapse onto a single straight line, fitted to

$$\chi_C = A(\psi - \psi_0) \tag{8}$$

Where $\psi_0 = 0.37$ is the volume fraction at which the crystallinity effectively disappears. It can be inferred, therefore, that this fraction of polymer is in a shell around the sample that is essentially unable to crystallize due to confinement near the particle surface forming a rigid amorphous phase that has been seen for other polymer-nanoparticle systems.[34] Ψ_0 corresponds to a particle volume fraction of a polymer shell thickness of

$$h = \left(\left(\frac{1}{1-\psi} \right)^{\frac{1}{3}} - 1 \right) R_{CORE} = 1.28 \text{ nm} \tag{9}$$

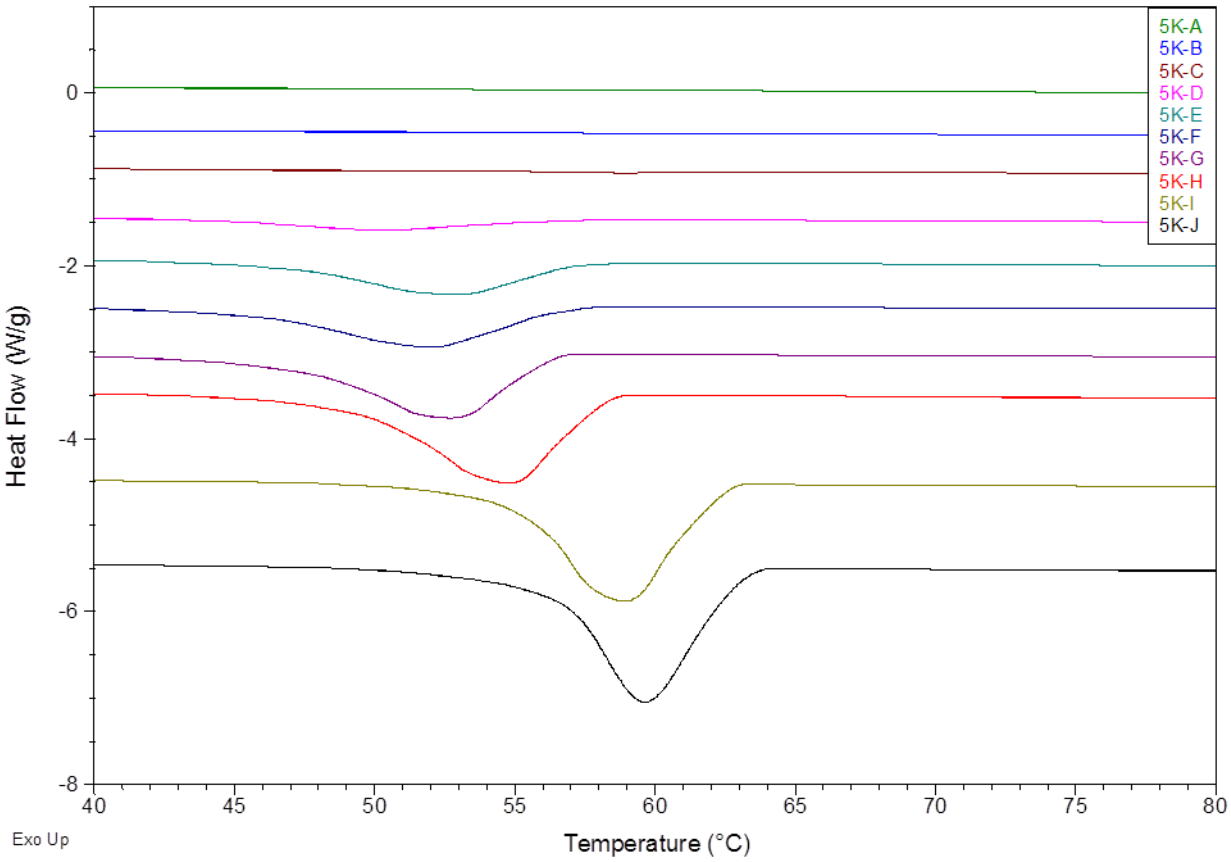

Figure 4.10: Differential Scanning Calorimetry traces on second heating for 5 kDa samples indicating a melting transition (endotherms down). The fraction of silica increases up the plot. Lines are arbitrarily offset for clarity.

		Molecular weight				
		2000	5000	10000	20000	30000.00
Graft density	0.10	0.06	0.04	0.01	0.25	0.38
	0.17	0.06	0.01	0.18	0.46	0.62
	0.31	0.04	0.06	0.45	0.60	0.75
	0.56	0.02	0.30	0.59	0.69	0.77
	1.0	0.05	0.58	0.68	0.77	0.85
	1.7	0.01	0.60	0.74	0.86	0.89
	3.1	0.45	0.71	0.86	0.89	0.88
	5.6	0.89	0.84	0.88	0.87	0.88
	7.8	0.66	0.90	0.94	0.91	0.87
	10	0.78	0.91	0.93	0.92	0.88

Table 4.3: Degree of crystallinity of the samples as a function of molecular weight and graft density.

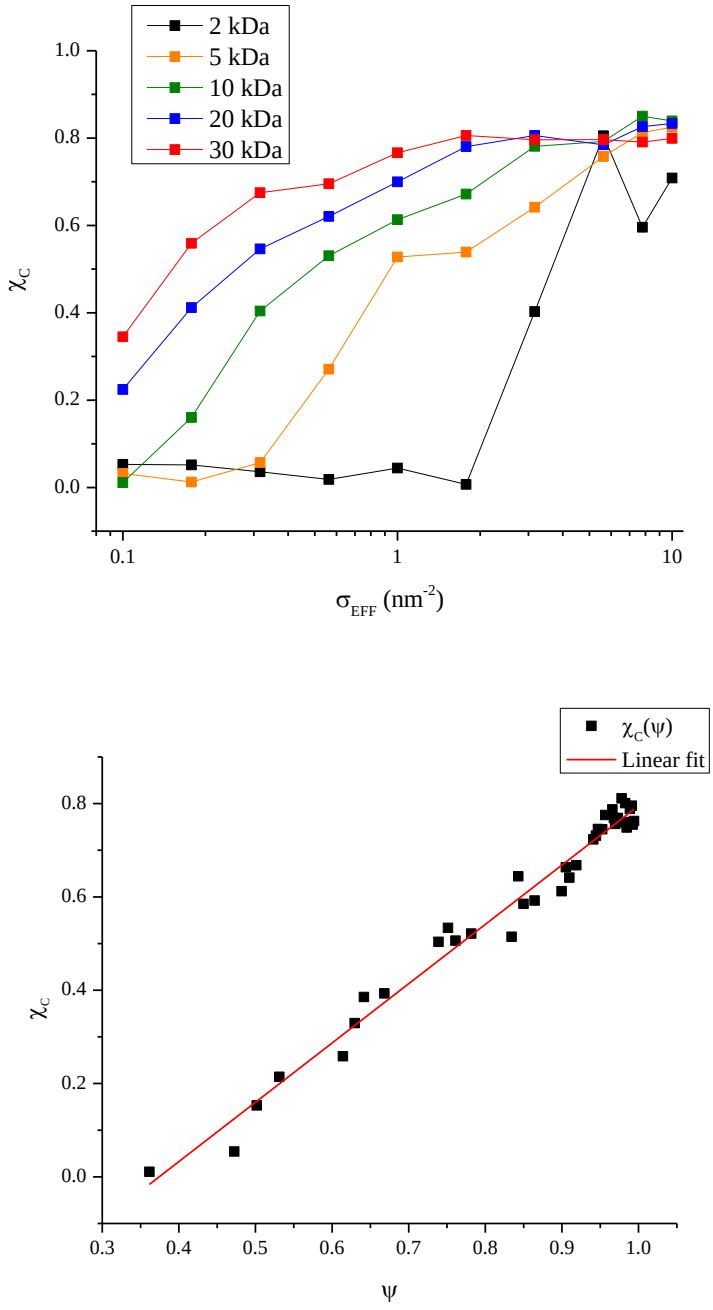

Figure 4.11: Degree of crystallinity as a function of (a) effective graft density, and (b) polymer volume fraction.

A polymer volume fraction of 0.37 is small compared to the volume fractions discussed above in rheology measurements. Therefore the polymer's local behavior is relatively unaffected by the presence of the particle except in the immediate vicinity of the particle, thus validating the general modeling approach taken above. This insensitivity of local dynamics of the polymer chains to the surface of the particle has also been seen in NMR studies.[11,12]

Samples with canopy molecular weights of 2 kDa display anomalous behavior, with samples with up to $\psi = 0.66$ (corresponding to h = 3.5 nm, $\sigma = 1.77$ nm^{-2}) showing a low χ_C. This can be explained by noting that, in the theoretical phase diagram shown in Figure 4.4, that with increasing graft densities, the samples with canopy molecular weights of 2kDa move directly from the "pancaked" region to the "CPB-only" region. Thus, through the entire sample set, all polymer chains are either confined to the surface of the particle, or confined in the CPB regime by neighboring chains, inhibiting crystal formation. It is only once the particles have reached what is expected to be the multilayer threshold that polymers filling the interstitial spaces between the particles can crystallize, and a crystalline peak appears in the DSC.

4.7 Conclusions:

Using dynamic light scattering, rheology, and differential scanning calorimetry, the behavior of a range of Nanoparticle Ionic Materials was studied. Based on Fukuda and coworker's adaptation of the Daoud-Cotton model, as well as observations made by Jespersen *et al.* on multiple dynamics observed in the canopies of these systems, a model for the canopy structure was constructed to explain the anomalous grafting densities observed when the state of the grafting-to reaction was monitored using acid/base titration curves. Dynamic Light Scattering confirmed that the titration curves did in fact represent particle/polymer reaction at grafting densities higher than previously reported for surface grafting of polymers.

A phase diagram was created to fully map the effect of graft density and molecular weight on the rheological properties. It was observed that the transition between soft glass behavior and Newtonian flow occurred near the onset of the expected multilayer transition. Using a criteria that expected glassy behavior to occur near the jamming threshold volume fraction, and correcting for the volume of polymer required to fill the interstices between the particle-polymer spheres, a corrected threshold density for the onset of the multiple layer effect was predicted.

The crystallization behavior of the polymer was also studied using differential scanning calorimetry. In most cases, the degree of crystallinity scaled linearly with polymer volume fraction, essentially vanishing completely at a volume fraction of 0.36. This volume fraction translated to a 1.28 nm layer around the particle, which is believed to be in a rigid amorphous phase seen in other nanocomposite systems. The relatively small thickness of this rigidly amorphous phase suggests that the behavior of the bulk canopy is not affected by interactions with the particles.

REFERENCES

(1) Fernandes, N. J.; Koerner, H.; Giannelis, E. P.; Vaia, R. A. Hairy nanoparticle assemblies as one-component functional polymer nanocomposites: opportunities and challenges. *MRS Commun.* **2013**, *3*, 13–29.

(2) Fernandes, N. J.; Wallin, T. J.; Vaia, R. A.; Koerner, H.; Giannelis, E. P. Nanoscale Ionic Materials. *Chem. Mater.* **2013**, 131009111600003.

(3) Rodriguez, R.; Herrera, R.; Bourlinos, A. B.; Li, R.; Amassian, A.; Archer, L. A.; Giannelis, E. P. The synthesis and properties of nanoscale ionic materials. *Appl. Organomet. Chem.* **2010**, *24*, 581–589.

(4) Bourlinos, A. B.; Giannelis, E. P.; Zhang, Q.; Archer, L. A.; Floudas, G.; Fytas, G. Surface-functionalized nanoparticles with liquid-like behavior: the role of the constituent components. *Eur. Phys. J. E. Soft Matter* **2006**, *20*, 109–17.

(5) Schaefer, J. L.; Lu, Y.; Moganty, S. S.; Agarwal, P.; Jayaprakash, N.; Archer, L. A. Electrolytes for high-energy lithium batteries. *Appl. Nanosci.* **2011**, *2*, 91–109.

(6) Kim, D.; Archer, L. A. Nanoscale Organic-Inorganic Hybrid Lubricants. *Langmuir* **2011**, *27*, 3083–3094.

(7) Oyerokun, F. T.; Vaia, R. A. Distribution in the Grafting Density of End-Functionalized Polymer Chains Adsorbed onto Nanoparticle Surfaces. *Macromolecules* **2012**, *45*, 7649–7659.

(8) Carvalho, B. L.; Tong, P.; Huang, J. S.; Witten, T. a.; Fetters, L. J. Adsorption of end-functionalized polymers on colloidal spheres. *Macromolecules* **1993**, *26*, 4632–4639.

(9) Penn, L. S.; Huang, H.; Sindkhedkar, M. D.; Rankin, S. E.; Chittenden, K.; Quirk, R. P.; Mathers, R. T.; Lee, Y. Formation of Tethered Nanolayers: Three Regimes of Kinetics. *Macromolecules* **2002**, *35*, 7054–7066.

(10) Jespersen, M. L.; Mirau, P. A.; von Meerwall, E.; Vaia, R. A.; Rodriguez, R.; Giannelis, E. P. Canopy dynamics in nanoscale ionic materials. *ACS Nano* **2010**, *4*, 3735–42.

(11) Jespersen, M. L.; Mirau, P. A.; Meerwall, E. Von; Vaia, R. A.; Rodriguez, R.; Fernandes, N. J.; Giannelis, E. P. NMR Characterization of Canopy Dynamics in Nanoscale Ionic Materials. In *NMR Spectroscopy of Polymers: Innovative Strategies for Complex Macromolecules*; American Chemical Society, 2011; Vol. 1077, pp. 149–160 SE – 9.

(12) Jespersen, M. L.; Mirau, P. A.; von Meerwall, E. D.; Koerner, H.; Vaia, R. A.; Fernandes, N. J.; Giannelis, E. P. Hierarchical Canopy Dynamics of Electrolyte-Doped Nanoscale Ionic Materials. *Macromolecules* **2013**, 131204112651000.

(13) Ohno, K.; Morinaga, T.; Takeno, S.; Tsujii, Y.; Fukuda, T. Suspensions of Silica Particles Grafted with Concentrated Polymer Brush: Effects of Graft Chain Length on Brush Layer Thickness and Colloidal Crystallization. *Macromolecules* **2007**, *40*, 9143–9150.

(14) Ohno, K.; Morinaga, T.; Takeno, S.; Tsujii, Y.; Fukuda, T. Suspensions of Silica Particles Grafted with Concentrated Polymer Brush: A New Family of Colloidal Crystals. *Macromolecules* **2006**, *39*, 1245–1249.

(15) Wang, Z.-G. Chain Dimensions in Amorphous Polymer Melts. *Macromolecules* **1995**, *28*, 570–576.

(16) Agarwal, P.; Qi, H.; Archer, L. A. The ages in a self-suspended nanoparticle liquid. *Nano Lett.* **2010**, *10*, 111–5.

(17) Agarwal, P.; Kim, S. A.; Archer, L. A. Crowded, Confined, and Frustrated: Dynamics of Molecules Tethered to Nanoparticles. *Phys. Rev. Lett.* **2012**, *109*, 258301.

(18) Srivastava, S.; Agarwal, P.; Archer, L. A. Tethered nanoparticle-polymer composites: phase stability and curvature. *Langmuir* **2012**, *28*, 6276–81.

(19) Agarwal, P.; Srivastava, S.; Archer, L. Thermal Jamming of a Colloidal Glass. *Phys. Rev. Lett.* **2011**, *107*, 268302.

(20) Schaefer, J. L.; Moganty, S. S.; Yanga, D. a.; Archer, L. a. Nanoporous hybrid electrolytes. *J. Mater. Chem.* **2011**, *21*, 10094.

(21) Srivastava, S.; Shin, J. H.; Archer, L. A. Structure and rheology of nanoparticle–polymer suspensions. *Soft Matter* **2012**, *8*, 4097.

(22) Corbierre, M. K.; Cameron, N. S.; Lennox, R. B. Polymer-stabilized gold nanoparticles with high grafting densities. *Langmuir* **2004**, *20*, 2867–73.

(23) Berne , Pecora, Robert,,, B. J. *Dynamic light scattering : with applications to chemistry, biology, and physics*; Wiley: New York, 1976.

(24) Malmsten, M.; Linse, P.; Zhang, K. W. Phase behavior of aqueous poly(ethylene oxide)/poly(propylene oxide) solutions. *Macromolecules* **1993**, *26*, 2905–2910.

(25) Barnes Hutton, J. F., Walters, Kenneth.,, H. A. *An introduction to rheology*; Elsevier : Distributors for the U.S. and Canada, Elsevier Science Pub. Co.: Amsterdam; New York, 1989.

(26) Larson, R. G. *The structure and rheology of complex fluids*; Oxford University Press: New York, 1999.

(27) Ueno, K.; Inaba, A.; Kondoh, M.; Watanabe, M. Colloidal stability of bare and polymer-grafted silica nanoparticles in ionic liquids. *Langmuir* **2008**, *24*, 5253–9.

(28) Ueno, K.; Imaizumi, S.; Hata, K.; Watanabe, M. Colloidal interaction in ionic liquids: effects of ionic structures and surface chemistry on rheology of silica colloidal dispersions. *Langmuir* **2009**, *25*, 825–31.

(29) Goyal, S.; Escobedo, F. a Structure and transport properties of polymer grafted nanoparticles. *J. Chem. Phys.* **2011**, *135*, 184902.

(30) Chremos, A.; Panagiotopoulos, A. Z.; Koch, D. L. Dynamics of solvent-free grafted nanoparticles. *J. Chem. Phys.* **2012**, *136*, 044902.

(31) Walls, H. J.; Caines, S. B.; Sanchez, A. M.; Khan, S. A. Yield stress and wall slip phenomena in colloidal silica gels. *J. Rheol. (N. Y. N. Y).* **2003**, *47*, 847.

(32) Fernandes, N. J.; Akbarzadeh, J.; Peterlik, H.; Giannelis, E. P. Synthesis and Properties of Highly Dispersed Ionic Silica-Poly(ethylene oxide) Nanohybrids. *ACS Nano* **2013**, *7*, 1265–71.

(33) Yuan-huffman, Q. W. Poly(ethylene oxide). *Polymer data handbook*; Mark, J. E., Ed.; Oxford University Press: New York, NY, 2009; Vol. 2.690–700.

(34) Klonos, P.; Panagopoulou, A.; Bokobza, L.; Kyritsis, A.; Peoglos, V.; Pissis, P. Comparative studies on effects of silica and titania nanoparticles on crystallization and complex segmental dynamics in poly(dimethylsiloxane). *Polymer (Guildf).* **2010**, *51*, 5490–5499.

CHAPTER 5

IONIC CROSSLINKING OF NANOPARTICLES WITH MULTIFUNCTIONAL POLY(ETHYLENE OXIDE)

5.1 Introduction:

"Hairy" nanoparticles, consisting of a nanoparticle core offer a new materials platform with significant advantages in scalability and tunable synthesis.[1] A wide range of materials and applications have been discussed that have focused on the ability of NIMs to form highly dispersed, often liquid-like materials.[2] However, the presence of the ionic bond opens new avenues for creation of novel ionic materials such as self-healing materials and elastomers.

Elastomers can be classified as thermoset or thermoplastic based on the nature of the crosslinks. Thermosets have covalent crosslinks, which have to be formed (by curing/vulcanization) after the material has been shaped. Once these crosslinks are broken, reforming them is difficult. This causes thermosets to be hard to process or recycle after they have been cured. Thermoplastics, on the other hand, rely on dynamic linkages. A common platform for thermoplastic elastomers is the use of phase separation: For example, one approach is to use triblock copolymers, such as polystyrene-block-polybutadiene-block-polystyrene. Microphase separation forms hard spheres of polystyrene connected by flexible polybutadiene. Thus, the polystyrene phase forms the crosslinks for the polybutadiene phase. Another approach is exemplified by the use of linear polypropylene with alternating isotactic and atactic blocks, where isotactic blocks crystallize to form crosslinks.[3,4]

Another platform involves hydrogen or ionic bonding to form dynamic crosslinks. Ionomers, for example, have been used as thermoplastic elastomers, and have been commercially available as Surlyn and Hycar.[5] Cordier et al. have demonstrated the creation of a self-healing elastomer by using a mixture of hydrogen bond donors and acceptors.[6] Additionally, self-healing ionic crosslinks have been demonstrated in catechol-functionalized polymers when mixed with Fe^{3+} ions at different pHs.[7]

It has been shown that harnessing ionic bonds as the interaction force between end-functionalized polymers and nanoparticles leads to highly dispersed systems with a uniform distribution of nanoparticles through the polymer.[8] This offers avenues for nanoparticle loadings to create optically, electronically, or magnetically responsive systems, thus allowing for additional functionality in applications areas traditionally limited to organic polymeric materials.[1] Theoretical studies have shown that the presence of ionic or hydrogen bonds improves the fracture strength of a crosslinked network of nanoparticles, and induces self-healing behavior.[9,10] A self-healing elastomeric electrically conductive material has already been demonstrated by filling a hydrogen-bonded elastomer with Ni particles.[11] However, to date the creation of crosslinked nanoparticle-based materials where the nanoparticle is an integral part of the system has been limited to relatively low molecular weight polymers.[12] The creation of nanoparticle-linked elastomers, therefore, is a fertile avenue for research and development.

In this study, a previously reported "corona-free" synthesis of Nanoparticle Ionic Materials (NIMs) based on silica and poly(ethylene oxide) is extended to create crosslinked networks (Figure 5.1) using multifunctional end-terminated polymers, as opposed to the monofunctional polymers used in previous studies of ionic materials. [8]

Although poly(ethylene oxide) is often used for the creation of hydrogels, it is not typically preferred for elastomeric applications as it has a high melting point, making it crystalline at room temperature. However, in this case, it provides some practical advantages: It is stable (and frozen) at room temperature, thus making it easy to control thermal aging of the material; it is water-soluble, simplifying synthesis; and it is available in high purity from a number of chemical suppliers, due to its applications in biotechnology.

The corona-free synthesis referred to above is a method of creating ionic hybrid materials utilizing the surface hydroxyl groups of silica. Under basic conditions, such as a salt-free solution of amine-terminated poly(ethylene) oxide, the surface hydroxyls are acidic and deprotonate. The proton is then exchanged to the base, in this case the amine group, thus creating an anionic nanoparticle and a cationic polymer molecule. The ionic hybrid is then the salt formed by these materials when all solvent (i.e. water) is removed.

5.2 Materials and Methods:

The hybrid materials were created as in a previously reported corona-free method. Briefly, silica was prepared by taking as-obtained Ludox® colloidal silica (HS-30, from Sigma-Aldrich), diluting it to 5% w/w in de-ionized water, and passing it over a cationic ion exchange resin (Dowex Marathon C, Sigma Aldrich) to remove the stabilizing sodium ions to form a hydroxylated form of silica.

To create the hybrid materials, first an appropriate amount of poly(ethylene oxide) was dissolved in water to create a 4% w/w solution. All poly(ethylene oxide) samples were obtained from Laysan Bio and had PDIs in the range of 1.02-1.05. An appropriate amount of hydroxylated silica dispersion was then added, and the mixture was rapidly stirred for 12 hours. The samples were frozen by immersing the vials in liquid nitrogen, and the water was removed by lyophilizing (-56C, ~256 μBar) followed by annealing in vacuum for 24 hours at 80°C. Resulting materials showed no weight loss at 100°C on thermogravimetric analysis, indicating an upper limit of less than 0.1% water. A number of samples were created as summarized in Table 5.1. All samples were created such that the effective grafting density was 1 amine group per nm^2 of silica particle surface.

Rheological and mechanical testing was carried out on an Anton-Paar MCR 301 Physica rheometer with 10 mm parallel plate setup, with a measuring gap maintained at 0.6mm. All measurements were carried out at 75°C.

Differential scanning calorimetry was carried out on a TA Instruments Q2000 Differential Scanning Calorimeter. ~4mg samples were weighed to an accuracy of 0.01 mg, and sealed in pre-weighed TZero™ hermetic aluminum pans. The samples were first heated to 100°C to erase any thermal history, and then cooled to -50°C and heated up to 100°C at 5°C per minute. All data is reported from the second heating.

Transmission Electron Microscopy images were obtained using an FEI T12 Spirit TEM/STEM. The T12 is a 120 kV field emission TEM, equipped with a LaB_6 filament and an SIS Megaview II CCD camera. Samples were prepared from solution by dropping a 1% aqueous solution of the sample on a copper grid, and blotting away excess liquid before drying and then annealing the grid at 75°C in vacuum.

Small Angle X-Ray scattering data was taken at the Cornell High Energy Synchrotron Source on the D-line, with a wavelength of 1.155 Å, and a sample to detector distance of 1338 mm. The samples were held in a hole in an aluminium plate holder using Kapton ™ tape, and equilibriated at 75°C before exposure. Images were taken with a camera with a 46.9 μm pixel size, and integrated using FIT2D software.

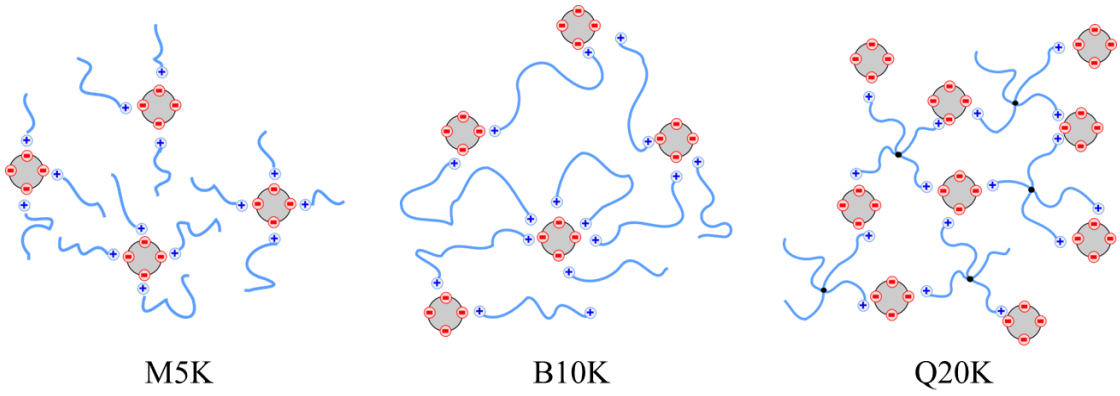

Figure 5.1: Schema illustrating the structural differences between A) mono-amine M5K, bi-amine B10K, and tetra-amine Q20K based ionic nanohybrids.

Sample	Polymer	Notes
S-M5K	M5K (5 kDa monoamine)	
S-B10K	B10K (10 kDa bi-amine)	
S-Q20K	Q20K (20 kDa tetra-amine)	
S-M10K	10K monoamine	For TEM comparison only
S-M20K	20K monoamine	
S-M$_{8}$B$_{2}$	80% M5K, 20% B10K	
S-M$_{6}$B$_{4}$	60% M5K, 40% B10K	
S-M$_{4}$B$_{6}$	40% M5K, 60% B10K	
S-M$_{2}$B$_{8}$	20% M5K, 80% B10K	

Table 5.1: Summary of samples created, and the polymers used. All samples had an inorganic content of 41.4% by weight, in order to maintain a constant acidic hydroxyl/amine ratio.

5.3 Results and Discussion.

Three poly(ethylene oxide) polymers were used for the majority of this study. M5K, which is mono-amine functionalized with a molecular weight of about 5 kDa; B10K, which has a molecular weight of about 10 kDa and is amine-terminated at both ends; and Q20K, which has a molecular weight of 20 kDa, and consists of four arms joined to a central point, with each arm terminated by an amine. The polymers were selected such that each polymer has the same (5 kDa) molecular weight per amine group (Figure 5.1), and vary only in the number of particles they can link together.

The acidity of the hydroxyl form silica of this silica is approximately $\Sigma = 1$ acid group/nm^2, which translates to 0.28 meq (acidic groups)/g(silica) or 800 acidic groups per particle.[8] Thus, in order to neutralize the acidic silica, this equivalent number of amine groups, were chosen for each sample. Since the polymer MW per amine group is a constant for all samples, all samples have the same organic/inorganic composition, consisting of 41.4% silica by weight, or a volume fraction $\varphi = 0.26$, assuming a density of 2.2 g/cm^3 for the silica and a density of 1.1 gm/cm^3 for the PEO. Note that this volume fraction is significantly lower than the jamming threshold for hard spheres, $\varphi_C = 0.63$, but is still within the threshold for which solid-like behavior is seen in solvent-free nanoparticle ionic materials.[13,14]

Figure 5.2(a, b c) show TEM images of the three samples, showing dense packing but no aggregation – each particle is well separated from its neighbors. Remarkably, S-M5K, S-B10K, and S-Q20K samples look identical in the micrographs. To highlight this similarity, analogous mono-amine samples with the same effective graft density but higher molecular weights, S-M10K (with a 10kDa monoamine) and S-M20K (with a 20kDa monoamine), (Figure 5.2(d,e)), show an increase in particle spacing, which as expected for an increase in polymer size.

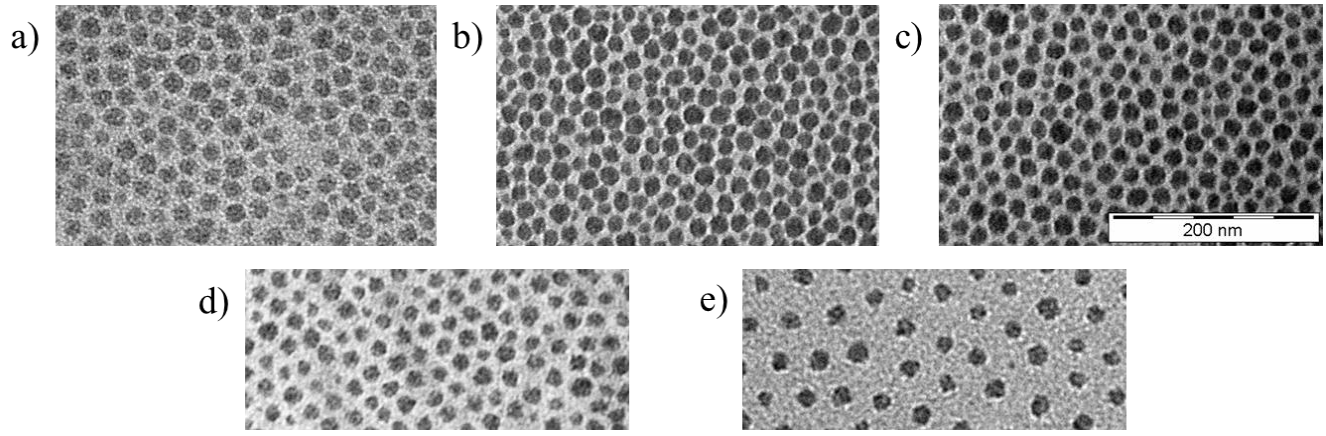

Figure 4.2: TEM Micrographs showing (a) M5K, (b) B10K, (c) Q20K. Samples M10K (d), and M20K (e) were created with the same graft density as M5K, but higher molecular weights (10 kDa and 20 kDa monoamines respectively) and are shown for comparison. Note that (a), (b) and (c) are essentially indistinguishable despite the difference in polymer molecular weights, while (d) and (e) show increased spacing due to the increased thickness of the polymer shell around each particle.

From the SAXS profiles (Figure 5.3), it is possible to characterize the morphology of the particles. As shown in figure 5.3(a), the scattering profiles show strong ordering, with peaks appearing in the intensity profiles at $q^*_{S-M5K} = 0.31$ nm^{-1},$q^*_{S-B10K} = 0.30$ nm^{-1}, and $q^*_{S-Q20K} = 0.33$ nm^{-1}. The Hansen-Verlet melting criterion, a method for distinguishing crystalline from fluid ordering, states that a sample is crystalline if $S_{max}(q) \geq 2.85$, where the structure factor $S(q) = \frac{I(q)}{P(q)}$ is given by the ratio of the scattering intensity of the sample to the scattering intensity of a dilute aqueous solution of the particles, normalized such that $S(q \to \infty) = 1$.[15–17] Using this criteria, we get $S(q_{S-M5K}) = 1.5$, $S(q^*_{S-B10K}) = 1.1$ and $S(q^*_{S-Q20K}) = 1.9$, demonstrating that the three samples are, despite the seeming order in the TEM grids, essentially amorphous.

Differential Scanning Calorimetry was used to examine the morphology of the poly(ethylene oxide) in the samples. Pure poly(ethylene oxide) is crystalline, with a theoretical latent heat of melting of 188 J/g.[18,19] It is to be expected that the confinement of the polymer between the nanoparticles would affect its crystallinity. By performing cyclic heating/cooling measurements on the samples, and integrating over the melting peak in the heat flow thermogram, it is possible to estimate the crystallinity of the polymeric component as given by $\chi_C = \frac{\Delta H_{Sample}}{\beta \Delta H_{Polymer}}$, where β is the weight fraction of polymer in the sample.[20] Traces are shown in Figure 4.4, and the results are summarized in Table 5.2. It can be seen that although the crystallinity of pure M5K and Q20K are very similar, the crystallinity of the polymer in the nanohybrids are not, with S-M5K having the same crystallinity as the pure polymer, and significantly more crystallinity than

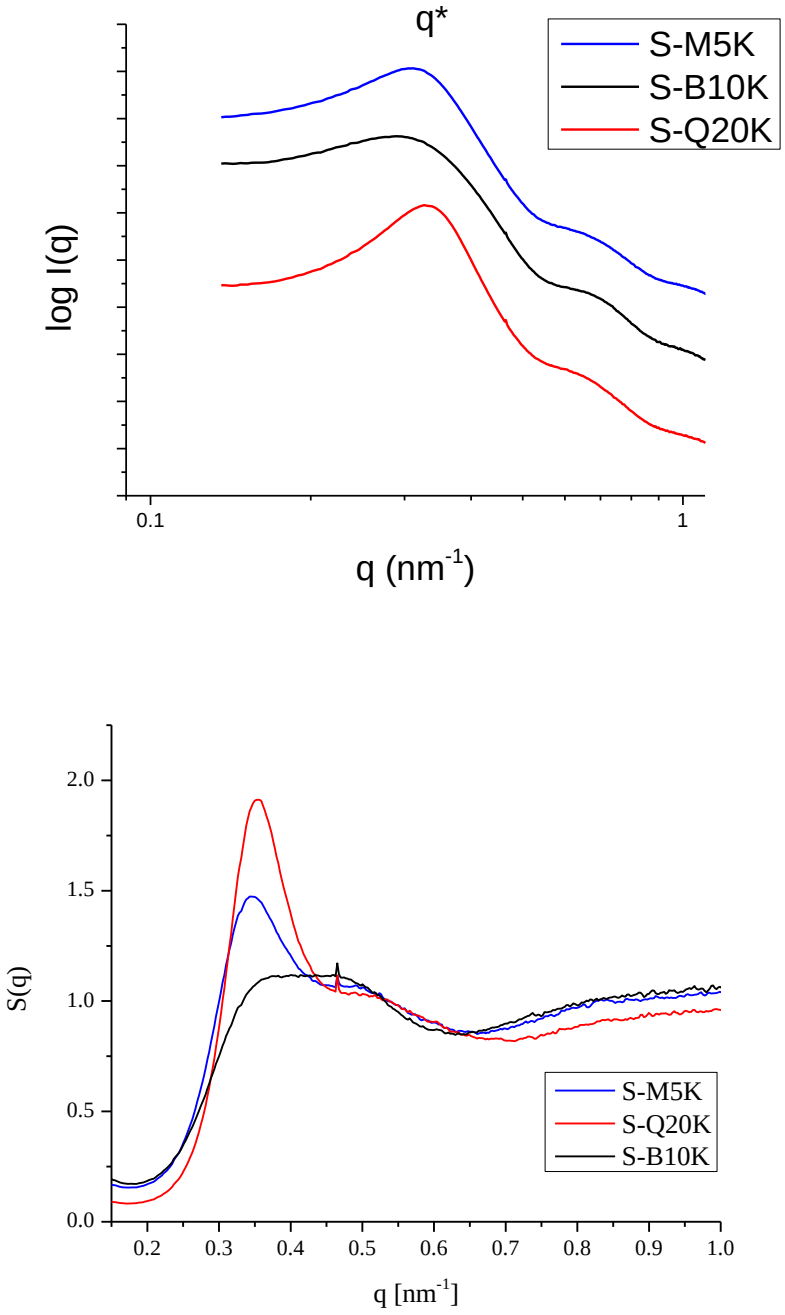

Figure 5.3: (a) Intensity profiles and structure factors (b) for three samples. The intensity profiles are arbitrarily offset for clarity.

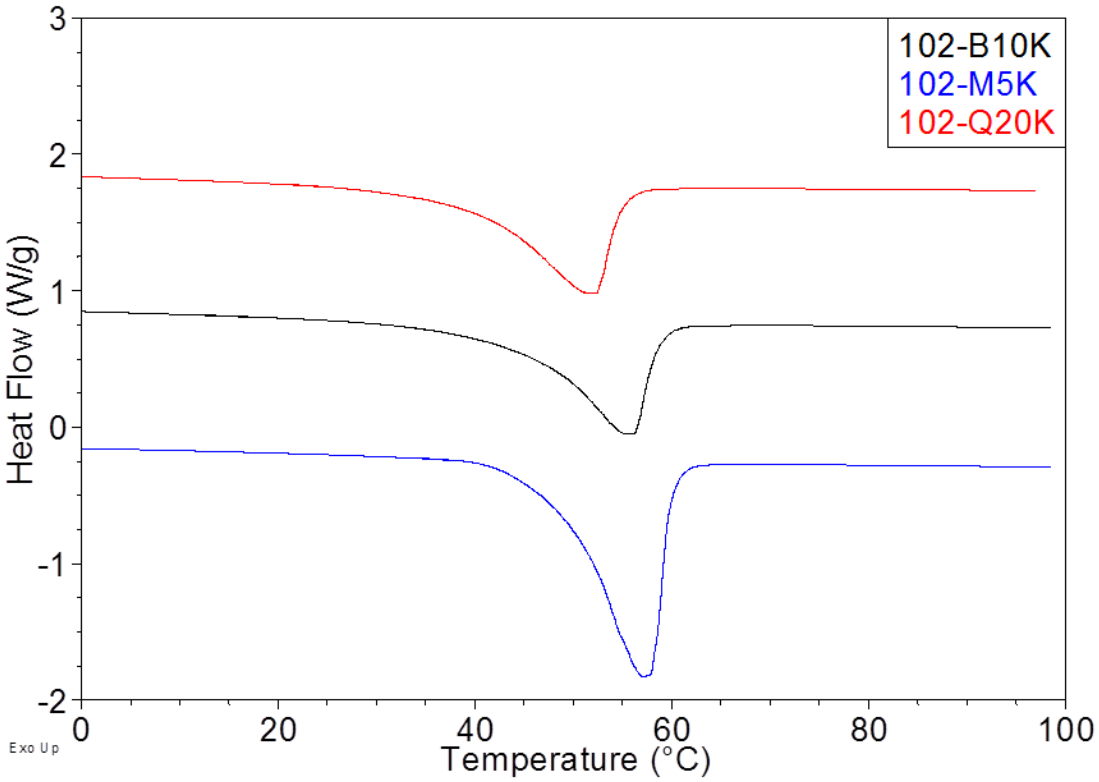

Figure 5.4: DSC melting thermograms. Curves have an arbitrary offset for clarity.

Sample	T_m (°C)	ΔH_m (J/g)	χ_C
M5K	60.2	147.2	0.75
Q20K	56.2	144.2	0.73
S-M5K	57	143	0.73
S-B10K	55	61.9	0.53
S-Q20K	52	61.2	0.53

Table 5.2: Summary of DSC melting data for two pure polymers and three samples.

S-B10K or S-Q20K. An increase in cross-linking thus leads to a decrease in crystallinity. However, there is no significant change in polymer crystallinity between S-B10K and S-Q20K, suggesting that the polymer conformation does not undergo significant change between the two samples.

To examine the mechanical properties of the materials, the response to oscillatory shear in a rheometer was measured. If an oscillating strain $\gamma(t) = \gamma_0 \sin \omega t$ is imposed and the shear stress is measured, the response can be written as $(t) = \sigma_0(\omega) \sin[\omega t + \delta(\omega)] = \gamma_0[G'(\omega) \sin \omega t + G''(\omega) \cos \omega t]$, where G' is the storage modulus, G'' is the loss modulus, and δ is the damping angle, given by $\tan \delta = \frac{G''}{G'}$. By varying γ while keeping ω constant, the behavior of the material under varying strains can be determined.[21,22]

From the moduli curves as a function of strain for S-M5K (Figure 5.5), we can see three distinct regions – i) a linear region, where G'> G'', and both are independent of the amplitude; ii) a nonlinear region where G' decreases but G'' increases, and iii) a flow region where G' < G'' and they both decrease with increasing strain, indicating shear melting of the material. The region in which G'' increases as a function of strain is a unique feature of jammed glasses, with the strength of the peak (normalized to $G'_{\gamma \to 0}$) indicating the degree of jamming.[13,23–25] Thus, although the volume fraction is lower than φ_C, the systems still display jammed behavior.

It is apparent from the strain sweeps that in the low strain linear region, the storage modulus increases from S-M5K to S-B10K to S-Q20K, with $G'_{S-M5K} = 2.22 \times 10^5$ Pa, $G'_{S-B10K} = 1.06 \times 10^6$ Pa, and $G'_{S-Q20K} = 1.68 \times 10^6$ Pa.

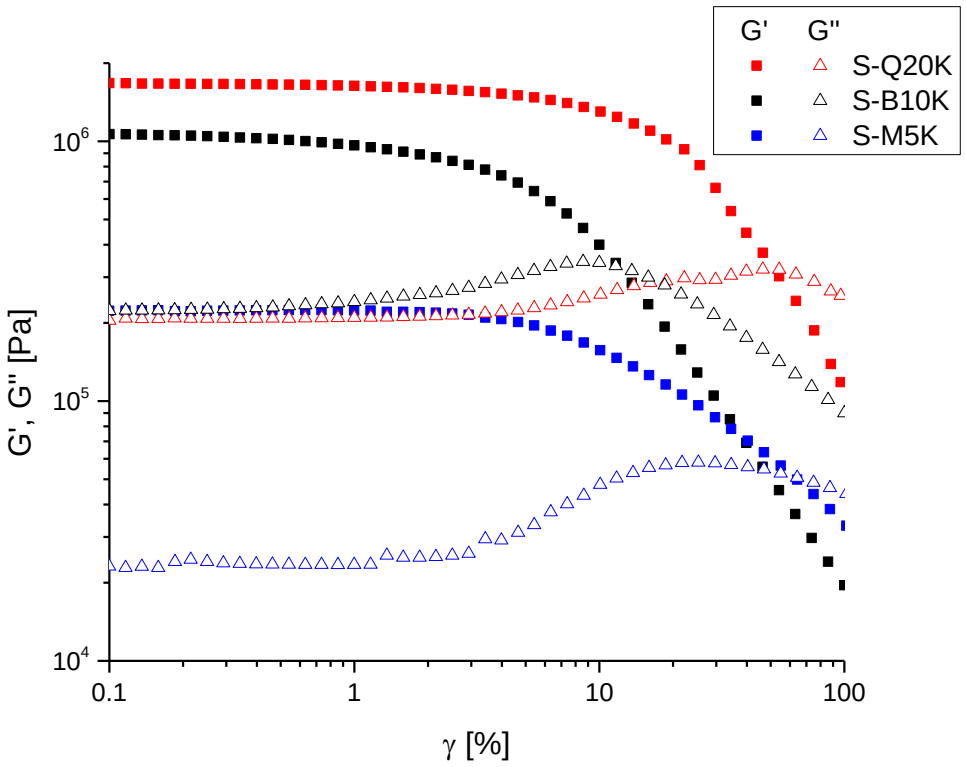

Figure 5.5: Amplitude sweeps of S-M5K (blue), S-B10K (black), and S-Q20K (red) showing the large increase in modulus with crosslinking.

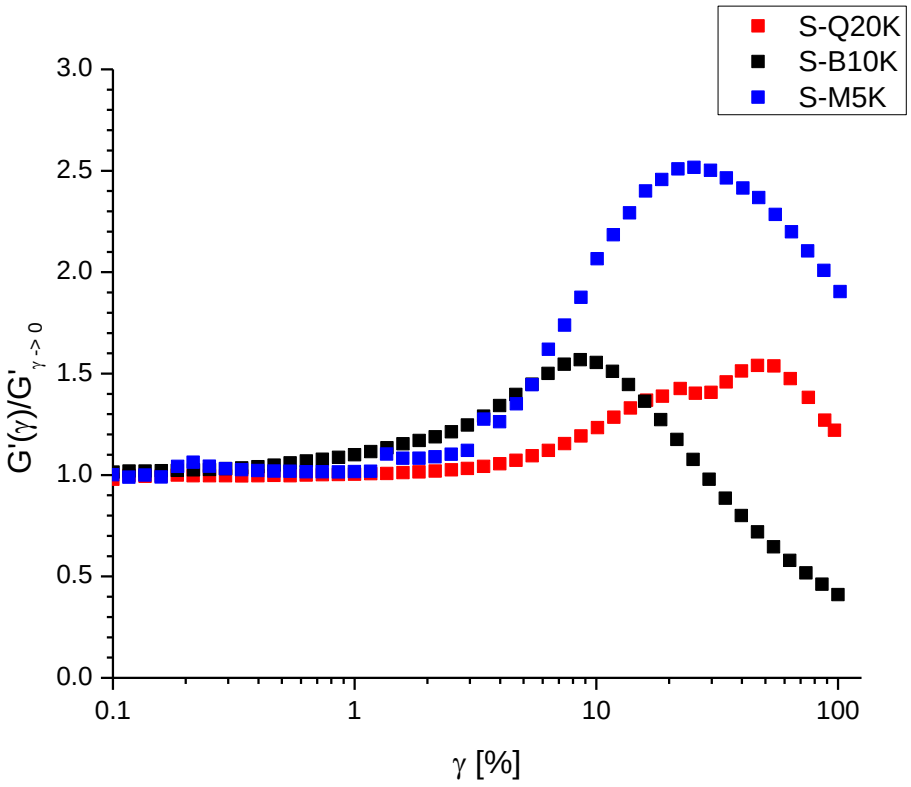

Figure 5.6: Normalized loss modulus $\frac{G''(\gamma)}{G''(\gamma \to 0)}$ as a function of γ, showing the distinctive loss peaks arising from jamming of the polymer-stabilized nanoparticles. The extended loss peak for S-Q20K at higher strains suggests that the entire loss process is due to slipping of the sample between the plates.

For crosslinked systems such as hydrogels, it has been shown that $G' = \nu RT$, where ν is the volume density of crosslinks, R is the universal gas constant, and T is the temperature.[26] For S-B10K, the volume density of crosslinks can be calculated by assuming that if the definition of a crosslink is a link between two polymer molecules, then each particle provides $2\pi R_{CORE}^2 \Sigma$ crosslinks. Using the density data given above, at 75°C, an estimate for $G'_{S-B10K} \sim 2 \times 10^5$ Pa, which is 5 times lower than the measured value. This discrepancy is attributed to the fact that the hydrogel theory is based on point crosslinks in relatively flexible polymers, while the systems under consideration consist of extended "crosslink" particles that are large in respect to the polymers, leading to a significantly higher modulus due to the high solid content and jamming of these particles.

In going from S-B10K to S-Q20K, the number of particle-mediated crosslinks remains constant. However, each Q20K polymer is equivalent to two B10K polymers joined at a central point. Using this equivalent system, therefore, there is one additional crosslink for every two B10K polymers, or half a crosslink per B10K polymer, increasing the total crosslink density by a factor of 1.5 and giving a predicted value (using the measured value for G'_{S-B10K}) of $G'_{S-Q20K} = 1.6 \times 10^6$ Pa. This is within 5% of the measured value, showing that while the absolute modulus of S-B10K could not be predicted, the scaling to S-Q20K is as expected.

On examining the normalized loss modulus $G''(\gamma)/G''_{\gamma \to 0}$, (Figure 4.6) it can be seen that the peak at higher strains, caused by cage breaking as particles are forced past each other, decreases in strength in from S-M5K to S-B10K, thus indicating a reduction in jamming, and a transition to a more rubbery material. It then remains roughly the same for S-Q20K, but moves to

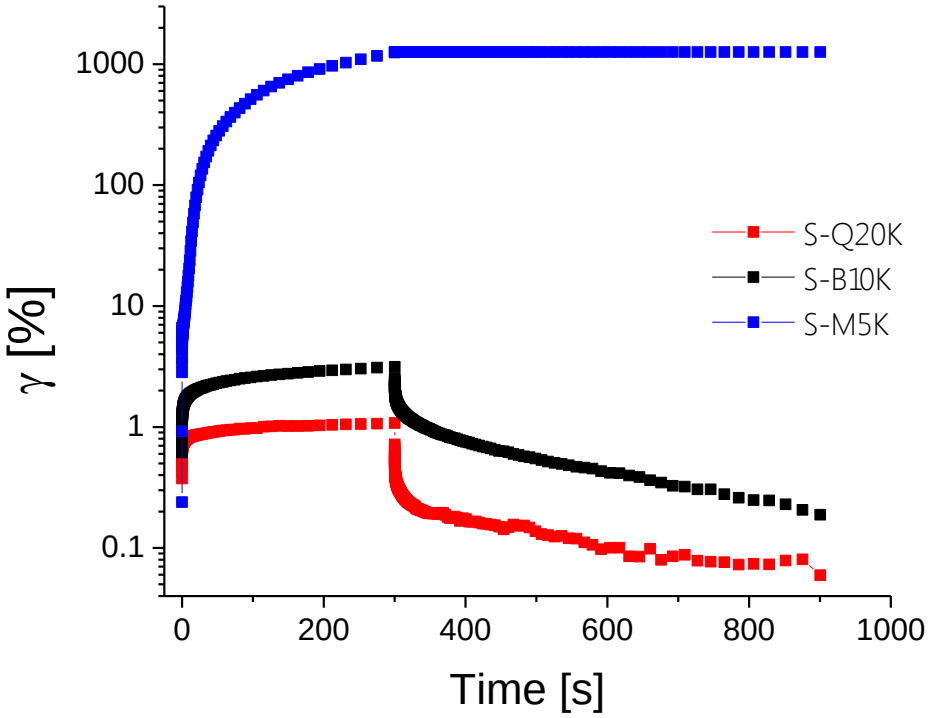

Figure 5.7: Time-strain plots for the sample during application of a constant σ = 20000 Pa shear stress (0<t<300s) and after the stress is turned off (t>300s), showing the recovery of strain for the two crosslinked samples.

higher strains and takes on an elongated appearance with multiple peaks, which is attributed to slip of the entire sample against the rheometer plates.[27]

The increase in the elastic or rubbery character of the material can be determined by looking at creep-recovery plots (Figure 5.7). Here a given shear stress ($\sigma = 20000$ Pa) was imposed for a fixed length of time t = 300s until the slope $\frac{\gamma}{t}$ achieved its terminal creep value. After this time, the stress was released, and the strain recovery was monitored. It can be seen that first, the strain is much greater for S-M5K than the two crosslinked samples. After the stress was released, S-M5K did not recover – the deformation was permanent. However, both S-B10K and S-Q20K recovered almost all their deformation, with the residual deformation at t = 900 being approximately 6% of the maximum value in both cases.

To examine the effect of gradually changing the density of crosslinks, samples S-M_xB_y were made with blends of M5K and B10K polymer, where *x* represents the fraction of M5K and *y* represents the fraction of B10K. There are two crosslinks per B10K molecule, and 0 crosslinks per M5K molecule, and the molecular weight of B10K is twice that of M5K, thus indicating that the number of crosslinks per unit mass (and thus the crosslink density *v*) is linear with *y*.

Figure 5.8 shows the strain sweeps for S-M_xB_y samples (in addition to S-M5K and S-B10K). The storage modulus as a function of *y* is presented in Figure 5.9. It can be seen that there is an increase in modulus, with a large jump (about a factor of 4) from S-M-5K to S-M_8B_2. It further increases for SM_6B_4, but then plateaus for S-M_4B_6, S-M_2B_8, and S-B10K. Adding additional B10K polymer beyond a fraction of 0.6 does not increase the degree of crosslinking in the material, which is likely due to the fact that additional B10K cannot "bridge" particles due to steric hindrance, thus not counting towards the crosslink density. However, the value of the damping

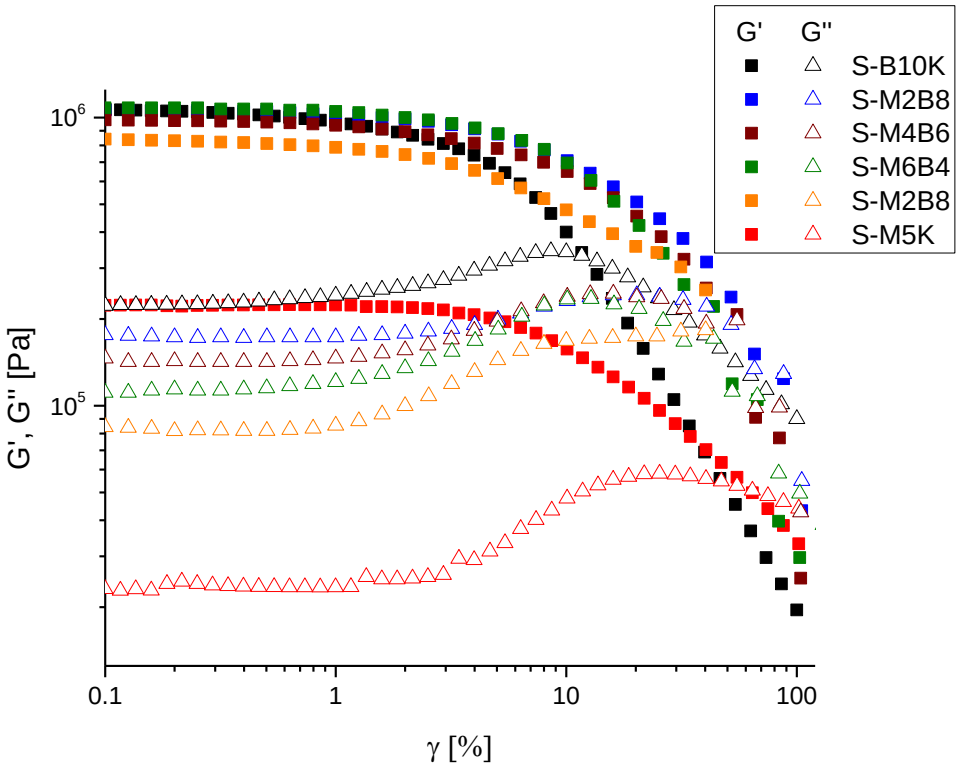

Figure 5.8: Amplitude sweeps for S-M_xB_y samples, showing the increase in modulus as the fraction of B10K (y) is increased.

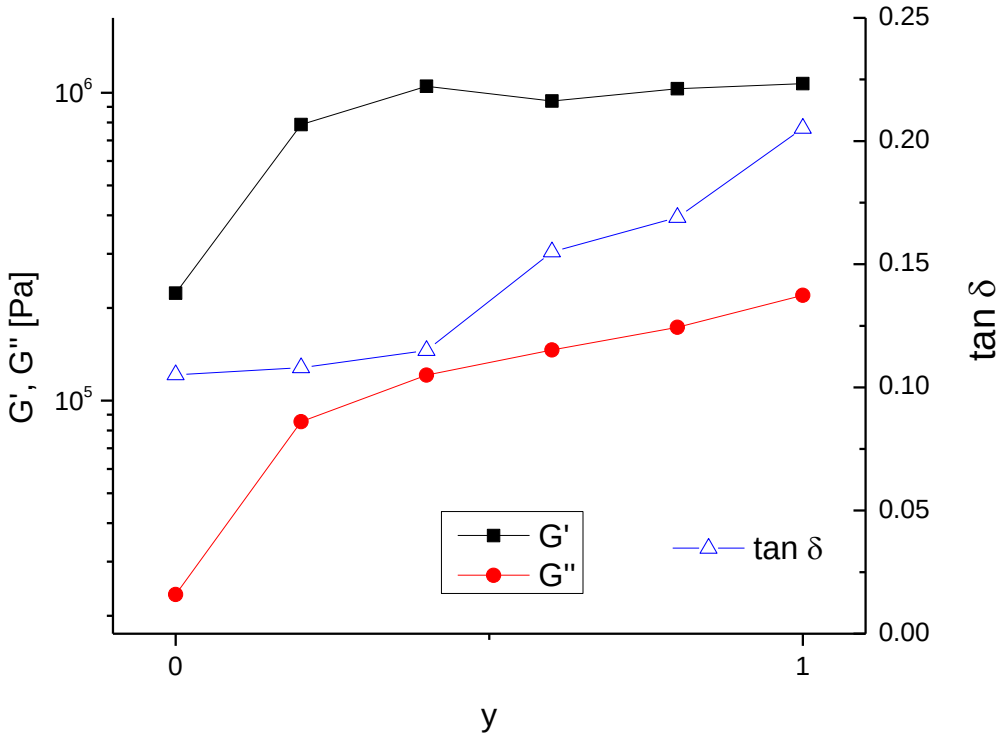

Figure 5.9: Evolution of storage and loss moduli (left) and damping factor tan δ (right) with increasing B10K fraction in S-M_xB_y samples.

factor $\tan\delta = \frac{G''}{G'}$ increases with increasing *y*, indicating that the samples have a slight increasing liquid character. This may be attributed to the fact that if an additional B10K polymer cannot bridge the polymer molecules, it must have one end relatively free. Due to its higher molecular weight, the free end is further from the particle surface, and thus is able to relax more freely, contributing a small flow component to the particles.

5.4 Conclusions

A method of creating ionically crosslinked nanoparticle-polymer hybrids is demonstrated using silica and poly(ethylene oxide). The ionic interactions between the acidic hydroxyls of the silica and the amine end groups of the polymers create a solvent-free system with high nanoparticle loading and good nanoparticle dispersion. When a simple "hairy" particle is created using a monofunctional amine, the material exhibits soft-glass behavior. However, when bifunctional and tetrafunctional polymers are used, keeping particle volume fraction constant, there is a large increase in the shear storage modulus, and the resulting materials are elastic, showing significant strain recovery. In particular, the change from bifunctional to tetrafunctional polymers follows the expected scaling for changing crosslink density. This crosslinking motif may offer alternative methods of creating nanohybrid materials with high inorganic particle loadings, or of creating highly toughened polymers. The dynamic nature of the ionic bond is expected to impart self-healing properties to these composites, but further work remains to be done on characterizing this self-healing behavior.

REFERENCES

(1) Fernandes, N. J.; Koerner, H.; Giannelis, E. P.; Vaia, R. A. Hairy nanoparticle assemblies as one-component functional polymer nanocomposites: opportunities and challenges. *MRS Commun.* **2013**, *3*, 13–29.

(2) Fernandes, N. J.; Wallin, T. J.; Vaia, R. A.; Koerner, H.; Giannelis, E. P. Nanoscale Ionic Materials. *Chem. Mater.* **2013**, 131009111600003.

(3) Rodriguez, F.; Cohen, C.; Ober, C. K.; Archer, L. A. *Principles of Polymer Systems*; 5th Editio.; Taylor & Francis: New York, 2003.

(4) Bhowmick , Stephens, Howard L.,,, A. K. *Handbook of elastomers*; M. Dekker: New York, 2001.

(5) Tant , Mauritz, K. A., Wilkes, G. L.,, M. R. *Ionomers : synthesis, structure, properties, and applications*; Blackie Academic & Professional: London; New York, 1997.

(6) Cordier, P.; Tournilhac, F.; Soulié-Ziakovic, C.; Leibler, L. Self-healing and thermoreversible rubber from supramolecular assembly. *Nature* **2008**, *451*, 977–80.

(7) Holten-Andersen, N.; Harrington, M. J.; Birkedal, H.; Lee, B. P.; Messersmith, P. B.; Lee, K. Y. C.; Waite, J. H. pH-induced metal-ligand cross-links inspired by mussel yield self-healing polymer networks with near-covalent elastic moduli. *Proc. Natl. Acad. Sci. U. S. A.* **2011**, *108*, 2651–5.

(8) Fernandes, N. J.; Akbarzadeh, J.; Peterlik, H.; Giannelis, E. P. Synthesis and Properties of Highly Dispersed Ionic Silica-Poly(ethylene oxide) Nanohybrids. *ACS Nano* **2013**, *7*, 1265–71.

(9) Iyer, B. V. S.; Salib, I. G.; Yashin, V. V.; Kowalewski, T.; Matyjaszewski, K.; Balazs, A. C. Modeling the response of dual cross-linked nanoparticle networks to mechanical deformation. *Soft Matter* **2013**, *9*, 109.

(10) Kolmakov, G. V; Matyjaszewski, K.; Balazs, A. C. Harnessing labile bonds between nanogel particles to create self-healing materials. *ACS Nano* **2009**, *3*, 885–92.

(11) Tee, B. C.-K.; Wang, C.; Allen, R.; Bao, Z. An electrically and mechanically self-healing composite with pressure- and flexion-sensitive properties for electronic skin applications. *Nat. Nanotechnol.* **2012**.

(12) Agarwal, P.; Chopra, M.; Archer, L. A. Nanoparticle netpoints for shape-memory polymers. *Angew. Chem. Int. Ed. Engl.* **2011**, *50*, 8670–3.

(13) Agarwal, P.; Srivastava, S.; Archer, L. Thermal Jamming of a Colloidal Glass. *Phys. Rev. Lett.* **2011**, *107*, 268302.

(14) Agarwal, P.; Qi, H.; Archer, L. A. The ages in a self-suspended nanoparticle liquid. *Nano Lett.* **2010**, *10*, 111–5.

(15) Goel, V.; Pietrasik, J.; Dong, H.; Sharma, J.; Matyjaszewski, K.; Krishnamoorti, R. Structure of Polymer Tethered Highly Grafted Nanoparticles. *Macromolecules* **2011**, *44*, 8129–8135.

(16) Hansen, J.; Verlet, L. Phase transitions of the Lennard-Jones system. *Phys. Rev.* **1969**, *184*, 151–161.

(17) Löwen, H.; Palberg, T.; Simon, R. Dynamical criterion for freezing of colloidal liquids. *Phys. Rev. Lett.* **1993**, *70*, 1557–1560.

(18) Yoshihara, T.; Tadokoro, H.; Murahashi, S. Normal Vibrations of the Polymer Molecules of Helical Conformation. IV. Polyethylene Oxide and Polyethylene-d4 Oxide. *J. Chem. Phys.* **1964**, *41*, 2902.

(19) Wunderlich ,, B. Thermal analysis of polymeric materials **2005**.

(20) Kavesh, S.; Schultz, J. M. Meaning and measurement of crystallinity in polymers: A Review. *Polym. Eng. Sci.* **1969**, *9*, 452–460.

(21) Larson, R. G. *The structure and rheology of complex fluids*; Oxford University Press: New York, 1999.

(22) Barnes Hutton, J. F., Walters, Kenneth.,, H. A. *An introduction to rheology*; Elsevier : Distributors for the U.S. and Canada, Elsevier Science Pub. Co.: Amsterdam; New York, 1989.

(23) Erwin, B. M.; Vlassopoulos, D.; Cloitre, M. Rheological fingerprinting of an aging soft colloidal glass. *J. Rheol. (N. Y. N. Y).* **2010**, *54*, 915.

(24) Vlassopoulos, D.; Fytas, G. High Solid Dispersions. In *Advances in Polymer Science: High Solid Dispersions*; Cloitre, M., Ed.; Springer Berlin Heidelberg: Berlin, Heidelberg, 2010; Vol. 236, pp. 1–54.

(25) Sollich, P.; Lequeux, F.; Hébraud, P.; Cates, M. Rheology of Soft Glassy Materials. *Phys. Rev. Lett.* **1997**, *78*, 2020–2023.

(26) Jiang, H.; Su, W.; Mather, P. T.; Bunning, T. J. Rheology of highly swollen chitosan/polyacrylate hydrogels. *Polymer (Guildf).* **1999**, *40*, 4593–4602.

(27) Walls, H.; Caines, S.; Sanchez, A.; Khan, S. Yield stress and wall slip phenomena in colloidal silica gels. *J. Rheol. (N. Y. N. Y).* **2003**.

CHAPTER 6

POLY(DIMETHYLSILOXANE)/SILICA CROSSLINKED IONIC HYBRIDS AS SELF-HEALING ELASTOMERS

6.1: Introduction

Nanoscale inorganic fillers have long been used to provide reinforcement to polymeric materials, leading to increases in modulus and yield stress.[1–4] These increases are believed to arise from mechanical reinforcement caused by percolating networks of nanoparticles.[2,3,5] There has been growing interest in creating highly dispersed nanoparticles by attaching the polymer to the particle directly, creating materials where the dispersion of the particle is achieved by tsteric means rather than by creation of kinetically trapped mixtures.[6,7] A subset of these nanoparticle polymer hybrids consists of polymer chains joined to particles by ionic bonds.[8] These hybrids have been created with a wide variety of core particles and polymers, and are seen as a method of creating stable dispersions of nanoparticles in polymers. A similar approach has been shown to be a versatile method of creating solvent-free nanoparticle fluids, due in part to the dynamic nature of the ionic bond,[9,10] as well as jammed soft glasses due to the flexibility of the polymeric layer that is strongly attached to the nanoparticle.[11,12] There has also been work done on post-assembly crosslinking of the polymeric canopy to create shape-memory materials.[13] Typical synthesis in this area focuses on the irreversible post-synthesis crosslinking using curing agents. Since these crosslinks are covalent bonds, any rupture of these is irreversible without the addition of fresh curing agent, either externally or by breakdown of pre-introduced micelles within the body of the material.[14]

In addition to the above, there has been significant work done in both academia and industry in the past several years on ionomers – polymer blends and block copolymers with a large proportion of ionic groups that undergo microphase separation into ionic-group rich blocks.[15] The phase structure of these blocks can be controlled by varying the degree of neutralization of

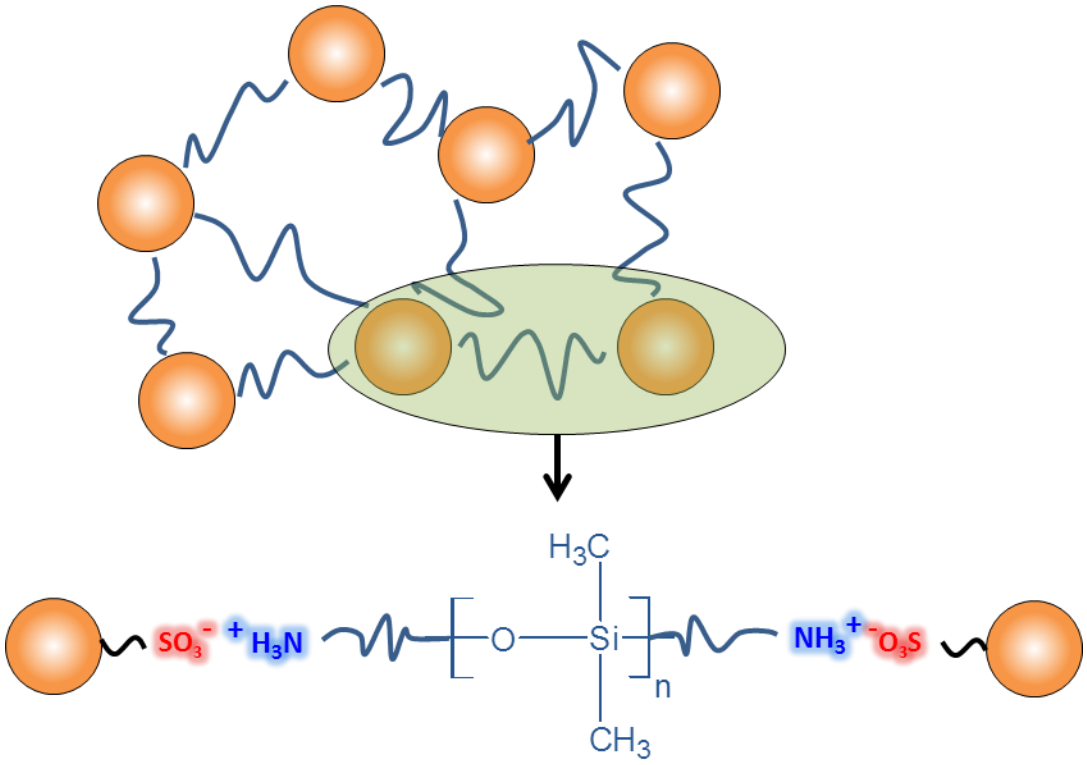

Figure 6.1. Schematic of ionic nanoparticle crosslinked materials.

the polymer. One crucial aspect of commercial exploitation of these ionomers is that neutralization is often carried out in the melt state, thus eliminating issues of solvent removal. Additionally, elastomeric materials based on ionic or hydrogen bonding between polymeric chains have been demonstrated. These materials have been shown to have self-healing behavior due to the dynamic nature of the bonding between the chains.[16,17]

These three seemingly disparate strands – ionomers, highly dispersed nanoparticle hybrids, and nanoparticle reinforced polymers can be unified to create extended networked materials where the crosslinks are formed by electrostatic attraction between polymer end groups and functionalized nanoparticle surfaces (Figure 6.1). Previously reported work (See chapter 5 of this dissertation) focused on poly(ethylene oxide) based materials as a proof of concept, with the crosslinks playing a role in toughening an otherwise brittle material. In this study, a system with real-world applications is considered. Poly(dimethylsiloxane) (PDMS) is a nontoxic polymer with applications in a wide range of areas, ranging from sealants and caulks to microfluidic devices, food additives, and cosmetics. It has a low glass transition temperature, and linear PDMS is liquid at room temperature even at relatively high molecular weights. Additionally, the synthesis used melt-mixing instead of previously reported solution chemistry, thus providing additional impetus to scale-up.

6.2 Materials and Methods:

Sulfonic acid functionalized silica was prepared by a previously reported method.[18] Briefly, Ludox HS-30 silica (Sigma Aldrich, 30% w/w in water) was diluted in de-ionized and added dropwise under stirring to a solution of 3-(trihydroxysilyl) propanesulfonic acid (Gelest, 30% w/w in water) in the ratio of 2g of silane to 1g of silica particles, and the pH was raised to

~5 by dropwise addition of aqueous 1M NaOH (Sigma Aldrich). The solution was then sealed and allowed to react at 70°C for 48 hours. The unreacted silane was then removed using tangential flow filtration. Finally, the resulting material was poured over a cation exchange resin (Dowex Marathon C) to remove residual sodium ions. The resulting sulfonated silica had an acid activity of 1.5 mmol/g(silica), as determined by titration. This solution was dehydrated in a lyophilizer to create a sulfonated silica powder.

To create the hybrid materials, the sulfonated silica powder was mixed with an appropriate mass of (α,ω) amino poly(dimethylsiloxane) (DMS A-31, MW ~25 kDa, Gelest). The mixing was carried out by a twin-screw extruder, with a small amount of water (2%) and tetrahydrofuran (1.5%) added as plasticizers. Extrusion time was 1 hour, with the first 30 minutes at 70^0C and the remainder cooling down to a final temperature of ~40°C. A series of samples was created with varied particle loadings (5%, 7.5%, 10%, 12.5%, 15%, and 20% by weight, as summarized in Table 6.1). For comparison, two control samples were synthesized at 15% loading by weight of silica. The first (CM) was created with a methyl terminated PDMS, and the second (CNa) was created using the amine-terminated PDMS with a silica that had been adjusted to pH 9 with NaOH before dehydration. After extrusion, the samples were annealed under vacuum for >24 hours at 90°C.

For samples that were compression molded, the molding was carried out by heating the samples to 80^0C and subjecting them to a pressure of 7 MPa.

In order to characterize the materials, an Anton Paar Physica rheometer (MCR 301/501) was used. The use of a rheometer in a manner analogous to a dynamic mechanical analyzer in shear mode allows comparison of liquid and solid samples under identical experimental parameters. The primary test was oscillatory strain sweeps to monitor storage modulus $G'(\gamma)$ and loss

Sample	Silica loading		σ_{EFF}	Reacted groups
	Weight fraction	**Volume fraction**	**nm^{-2}**	**mmol/g(silica)**
Pure PDMS	0	0	-	
S5	0.05	0.023	5.4	1.53
S7.5	0.075	0.035	3.5	0.99
S10	0.1	0.047	2.5	0.72
S12.5	0.125	0.06	2.0	0.56
S15	0.15	0.073	1.6	0.45
S20	0.20	.10	1.1	0.32

Table 6.1: Summary of samples studied, showing the relationship between silica loading by weight, volume fraction of silica, effective graft density of the polymer on the particle surface, and the number of amine-sulfonate pairs per gram of silica.

modulus $G''(\gamma)$ at a fixed frequency of $\omega = 10\ s^{-1}$. Liquid samples were measured with a cone and plate geometry with a diameter of 25mm and a cone angle of 1°. Solid samples were measured with a 10mm diameter parallel plate setup, with a gap of 0.6mm. All measurements were performed at 25°C unless otherwise specified.

In order to monitor the strength recovery of molded samples, the sample was loaded into the rheometer, which had been pre-heated at the appropriate temperature, and a small strain oscillation (γ = 0.1%, ω = 10 s^{-1}) was imposed. A new data point was measured every 30s. The initial portion of the recovery curve G'(t) was not utilized for fitting the recovery rate in order to ensure that the samples reached thermal equilibrium.

Differential Scanning Calorimetry was carried out using a Thermal Analysis Q2000 DSC instrument. In a typical experiment, a small quantity (2-10 mg) was weighed out into a hermetically sealed TZero™ pan. The sample was heated to 120^0C to erase any thermal history and then cooled to -150°C and heated to 100^0C at 5 °C/min.

6.3 Results and discussion

The acid functionality of the silica nanoparticles was determined by titration to be 1.5 mmols/g. Using an average radius R_{CORE} of 8 nm (determined independently by TEM), the surface activity was calculated to be $\sigma_{MAX} = 4$ SO_3H groups per nm^2. After mixing, the effective graft density of PDMS chains based on the inorganic fraction α, the effective molecular weight per amine group (M_{eff} = M/2 = 12.5 kg/mol), and the density of colloidal silica ρ_{CORE} is:

$$\sigma_{Eff} = \frac{R_{CORE}}{3}\frac{\rho_{CORE}N_A}{M_{Eff}}\left(\frac{1-\alpha}{\alpha}\right) \quad (1)$$

During the extrusion process, when the $–SO_3H$ groups from the particles approach the $–NH_2$ groups on the polymer, the reaction

$$\textit{(Particle)}\text{-}SO_3H + H_2N\text{-}\textit{Polymer} \rightleftharpoons \textit{(Particle)}\text{-}SO_3^{-}{}^{+}H_3N\text{-}\textit{Polymer} \qquad (2)$$

occurs, similar to the solution processes described earlier. While solid state reactions acid-base reactions have been reported[19], the presence of a trace amount of water is believed to be necessary for the above reaction to occur, as the absence of any water leads to an unstable slurry. Immediately after the extrusion process, the resulting material is a sticky soft gel. After annealing and solvent removal, the samples (other than S5 and S7.5) harden. The annealing is necessary both to remove any residual trace of solvent and to form crosslinks after the high-shear/high temperature environment of the extruder, a process that will be further discussed below.

The mechanical properties of the hardened materials are found to depend on the particle content. Oscillatory strain sweeps (Figure 6.2) were carried out to determine the response of the material to shear. It is easy to see that the moduli are largely independent of strain up to very high strains. The sweeps show that for samples with more than 10% by weight of silica, the annealed material is a rubbery solid, with G’ > G’’.

It is important to note here that S10, which is the first solid sample, has a particle core volume fraction of 0.047. This over an order of magnitude less than the jamming threshold of spheres in a colloidal suspension, eliminating jamming of the nanoparticles as a cause for this solid-like behavior. Further, the strain sweeps only show two regimes – a strain-independent region (also known as the linear viscoelastic regime) and a softening region. There is no region where G’ decreases as G’’ increases, thus suggesting that the material does not have the soft-glass character that has been seen for star polymers and non-crosslinked hairy nanoparticles in a

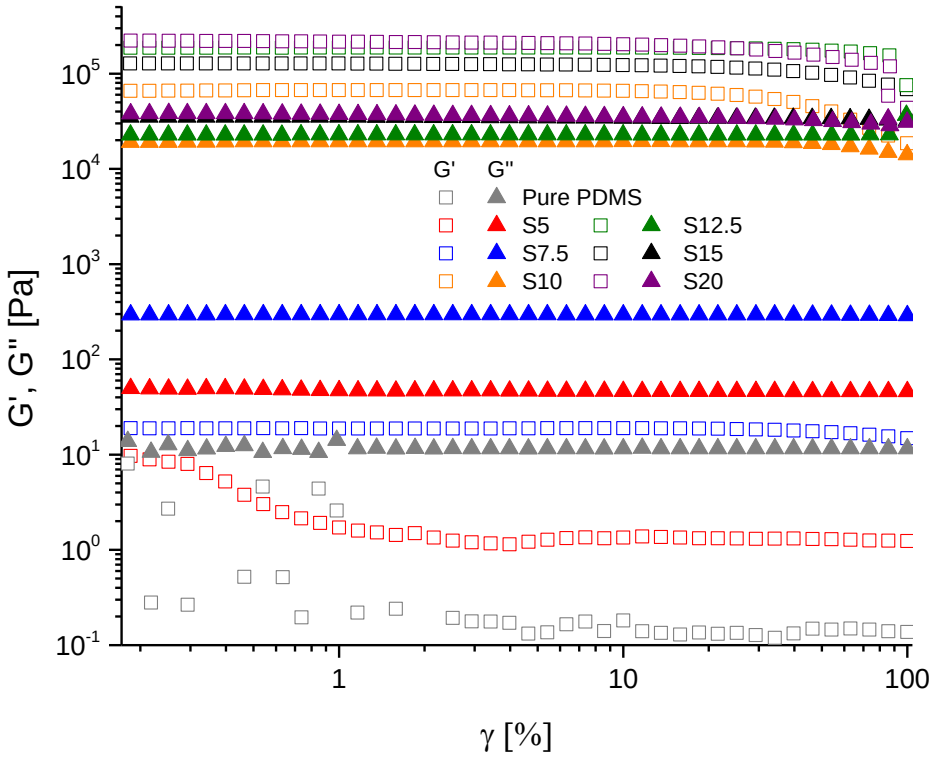

Figure 6.2. Strain sweeps for 7 different samples, from pure PDMS to a 20% by weight silica blend. Storage moduli G' (open squares) and loss moduli G'' (filled triangles) are shown.

‘

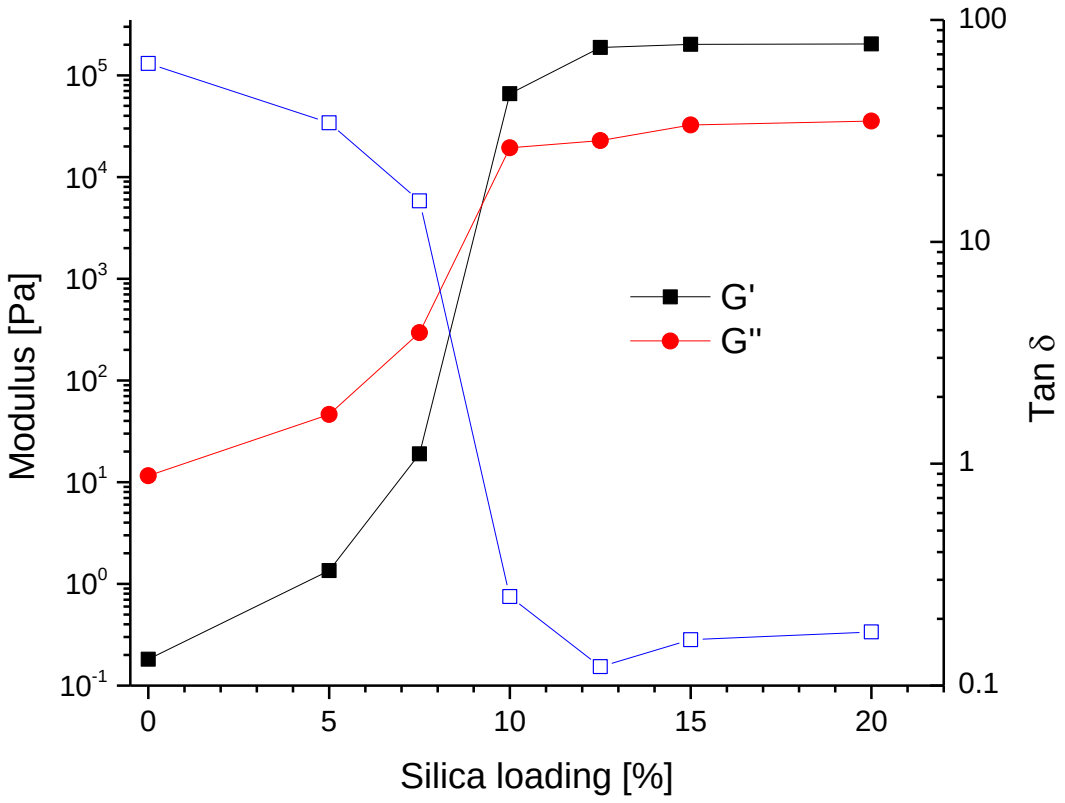

Figure 6.3: Moduli and damping factor as a function of silica loading. Lines are a guide to the eye.

jammed state.[11,12,20]

The solid/liquid nature of the materials can be determined by examining the damping factor $\tan\delta = \frac{G''}{G'}$ in the linear viscoelastic regime. Figure 6.3 shows tan δ as a function of particle loading and σ_{Eff}. The samples become more solid with increasing particle loading up to a point, with an increase of modulus of over six orders of magnitude from the pure polymer. The damping factor (and the moduli) are effectively unchanged after a critical loading of between 10% and 12.5% is reached. This translates to an effective graft density of 2 nm^{-2} for a particle loading of 12.5%, and a sulfonate-amine pair/silica ratio of 0.56 mmols/g(silica). The lack of change of modulus beyond this region indicates that the particle loading alone does not determine the mechanical properties of the hybrid.

This can be explained by considering the nature of the material. Since each particle can form at most $4\pi R_{CORE}^2 \sigma_{EFF}$ bonds with polymeric chains, if a crosslink is defined as the connection between two independent polymer chains, the number of crosslinks is $2\pi R_{CORE}^2 \sigma_{EFF}$ per particle. Low particle loadings then can be viewed as systems where fewer bridges are formed since a polymer whose α amine reacts with one particle is unable to also form a bond with its ω amine to another particle due to steric hindrance that prevents the amine group from approaching the surface of the second particle.

After the critical loading is reached, the system reaches a saturation number of bridges, where all the bridges that are possible have been formed. There are no unreacted amine sites left, so any additional particles merely act as filler, and not as additional crosslinking sites.

In several crosslinked systems, the shear storage modulus (for small strains) is linearly proportional to the crosslink density per volume.[21]

$$G' = RTv. \qquad (3)$$

This relationship does not hold for varied particle loading, as the polymer-rich systems cannot achieve all crosslinks due to steric hindrance, while the polymer-starved systems have been saturated with crosslinks. However, for a given system, it is possible to determine the change in crosslink density due to plastic disruption. Considering S12.5 as a fully crosslinked system, with ρ_{PDMS} = 980 kg/m^3 and ρ_{Silica} = 2200 kg/m^3, then $\rho_{S12.5}$ = 1100 kg/m^3. Thus, the concentration of silica particles is 225 kg/m^3. Since the ion-pair/silica ratio is 0.56 mmol/g for this system, if a crosslink is defined (as above) as two polymer chains linked by a particle, the volume density of crosslinks v = 63 mol/m^3 = 3.8x10^{25} crosslinks/m^3. Using the expression (3) above, the theoretical predicted value of G' is $G'_{S12.5} = RTv = 15700$ Pa, which is within 20% of the actually measured value of 18700 Pa. This agreement is remarkable when the imprecise definition of a crosslink is considered, since the relationship was held to be true for crosslinks defined a point intersection of just two chains, while in reality it consists of large nanoparticles with approximately 800 particles linked at the surface.

Additional evidence for the critical role of the ionic crosslinks can be determined by comparing control samples, where the ionic interactions have been turned off by a) using a methyl-terminated PDMS instead of an amine-terminated PDMS, and b) by using silica particles where the pH was adjusted to 9 with dilute NaOH. In both cases the resulting material was a viscous slurry of silica aggregates in a PDMS matrix. The samples were liquid, showed no strength increase on annealing, and phase separated over time (Figure 6.4).

The advantage of the ionic bonds are their essentially reversible character. Crosslinked PDMS swells in a good solvent; this property is used in standard swelling tests to determine crosslink density. However, when the sample S15 was placed in hexane, it dissolved completely

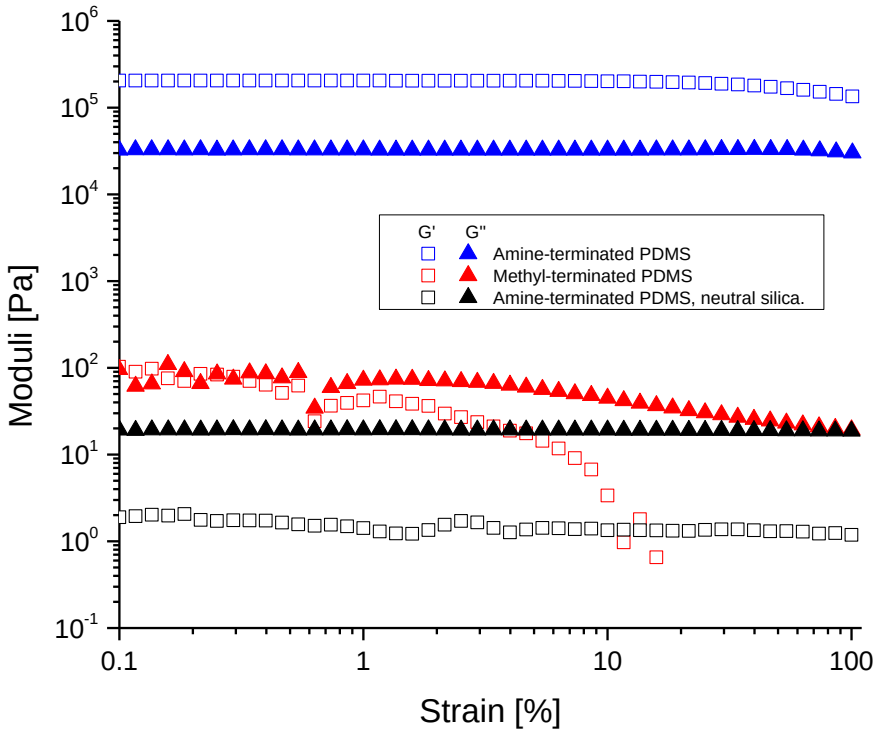

Figure 6.4. Strain sweeps of sample S15 (blue) with ionic interactions, and two control systems without ionic interactions – red shows methyl-terminated PDMS blended with sulfonated silica, and black shows amine-terminated PDMS blended with sulfonated silica that was neutralized to pH = 9 by sodium hydroxide prior to blending.

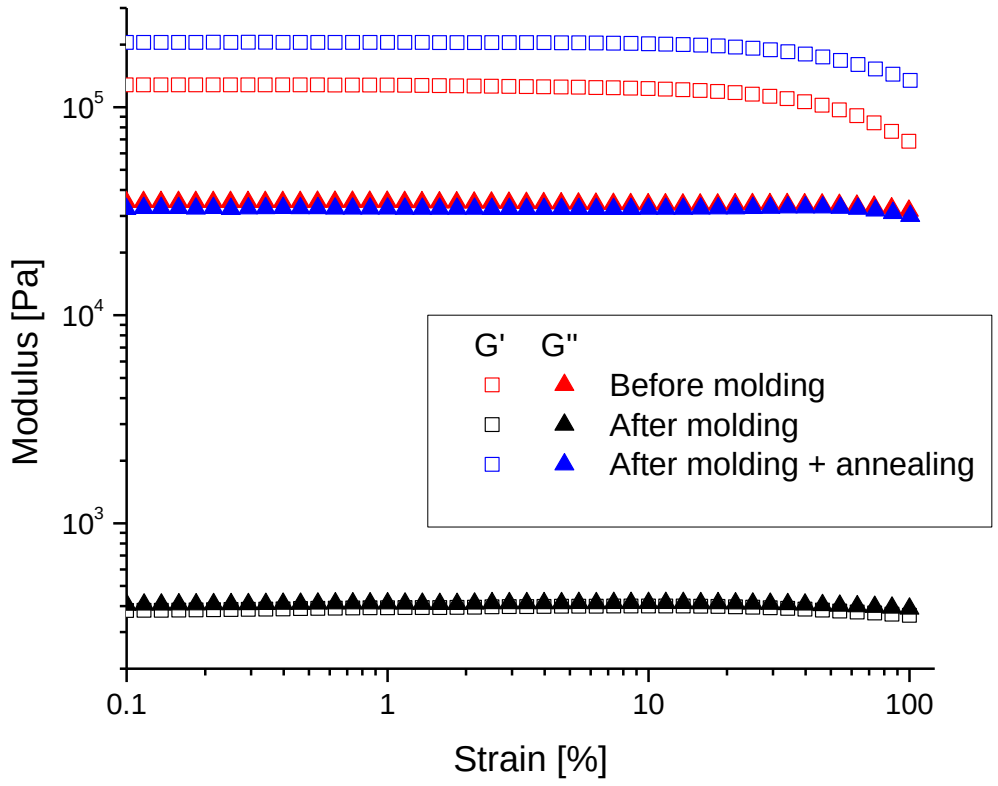

Figure 6.5: Strain sweeps before compression molding (red), immediately after compression molding (black), and after annealing for 48 hours at 90^0C (blue) showing recovery of rubberlike character.

due to the low dielectric constant of hexane favoring the de-ionization of the reactive groups, driving the equilibrium to the left in reaction (2). This property allows solvent-mediated defect healing in coatings consisting of these materials.

The dynamic nature of the ionic bond is not limited to solvent dissolution. When the sample S15 was put through a process of compression molding, with a pressure of 7 MPa and a temperature of 80°C, it softened significantly, as seen in the strain sweeps (Fig. 6.5). However, the material recovered its strength when it was annealed for 24 hours in vacuum at 75^0C. When the shear is removed, the chain fluctuations allow the end groups to spatially explore their immediate neighborhood and bond to new particles that have been moved to their neighborhoods. This strength recovery was reversible – repeated molding and annealing showed no variation in the softening or recovery process.

If the modulus is monitored as a function of time by small amplitude oscillations, the storage modulus increases to an asymptotic value, and the rate of increase of $G'(t)_{\gamma,\omega}$ increases with temperature (Fig 6.6.). For the healing process, an approximate rate $\left.\frac{\partial G'}{\partial t}\right|_T = k\frac{\partial v}{\partial t}$ can be extracted by looking at an approximately linear regime in the region of maximum increase. Using a linear fit at each temperature, a slope was extracted and the results are summarized in Table 6.2.

A number of polymer mechanical properties, such as terminal relaxations, follow Arrhenius-like behavior. Thus, if the rate of crosslink formation follows Arrhenius-type temperature dependence, it is expected that:

$$\frac{\partial G'}{\partial t} = \mathrm{A}e^{B/T} \tag{4}$$

or

$$\ln \frac{\partial G'}{\partial t} = \ln A + \frac{B}{T} \quad (5)$$

where $B = -\frac{E_A}{R}$

A fit of $\ln \frac{\partial G'}{\partial t}$ vs. $\frac{1}{T}$ verifies a linear relationship, with B = - 4710 ± 360 K^{-1} (adj. R^2 = 0.97), which translates to an activation energy of 39 ± 3 kJ•mol^{-1}. This activation is roughly twice the activation energy measured for segmental relaxations of PDMS using rheology [22]. One potential explanation is that since the formation of a bridge involves each end of the chain finding a particle, the activation energy measured for annealing is the energy for two relaxations of the same molecule, thus having twice the value.

The transition from liquid to rubbery solid can also be seen in differential scanning calorimetry traces of the samples (Figs. 6.8 and 6.9, Table 6.3). Figure 6.8 shows the second heating curve of samples S5, S7.5, S10, S12.5 and S15, as well as pure PDMS. Pure PDMS shows a glass transition at T_g = -126°C, a cold crystallization process at T_{cc} = -85^{0}C, and two melting processes at T_{m1}= -46^{0}C and T_{m2} = -36°C, where the crystals formed in the cold crystallization melt. All these transitions are visible in samples S5 and S7.5 with no significant shift in the temperatures. The cold crystallization process for S0, S5, and S7.5 is due to the quenching of the samples as they cool.[23] As the sample is reheated to above T_g, the chains are able to crystallize and then re-melt. Samples S10, S12.5 and S15 do not show a cold crystallization transition. Instead, as seen from the cooling curves, they exhibit a normal freezing transition at T_c ~ -75°C. For S12.5 and S15, the double melting transition at T_{m1},T_{m2} is replaced by a single melting transition at T_{m*} ~ T_{m2}, while S10 shows a small residual double-peaked transition. Conversely, there is no freezing process visible in the cooling curves for pure PDMS,

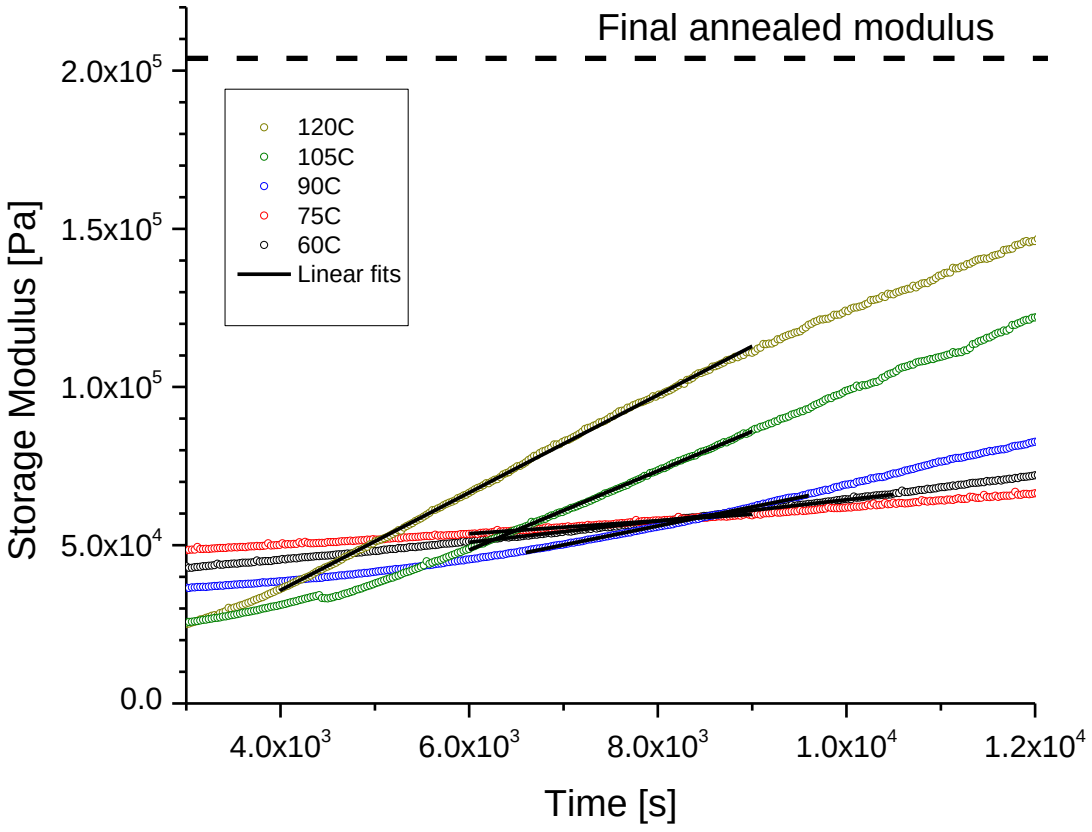

Figure 6.6: Monitoring the process of strength recovery using small amplitude oscillations at 5 temperatures. Black lines are linear fits in the region of greatest slope.

T	Fitting range		Slope $\frac{dG'}{dt}$	R^2	StdErr
[K]	From (s)	To (s)	(Pa•s^{-1})		(Pa•s^{-1})
393	3990	9000	15.4	0.999	0.03
378	6000	9000	12.5	0.999	0.03
363	6600	9600	6.0	0.997	0.03
348	6000	10500	3.4	0.998	0.012
333	6000	9000	2.0	0.992	0.02

Table 6.2: Fit parameters for recovery of modulus at various temperatures.

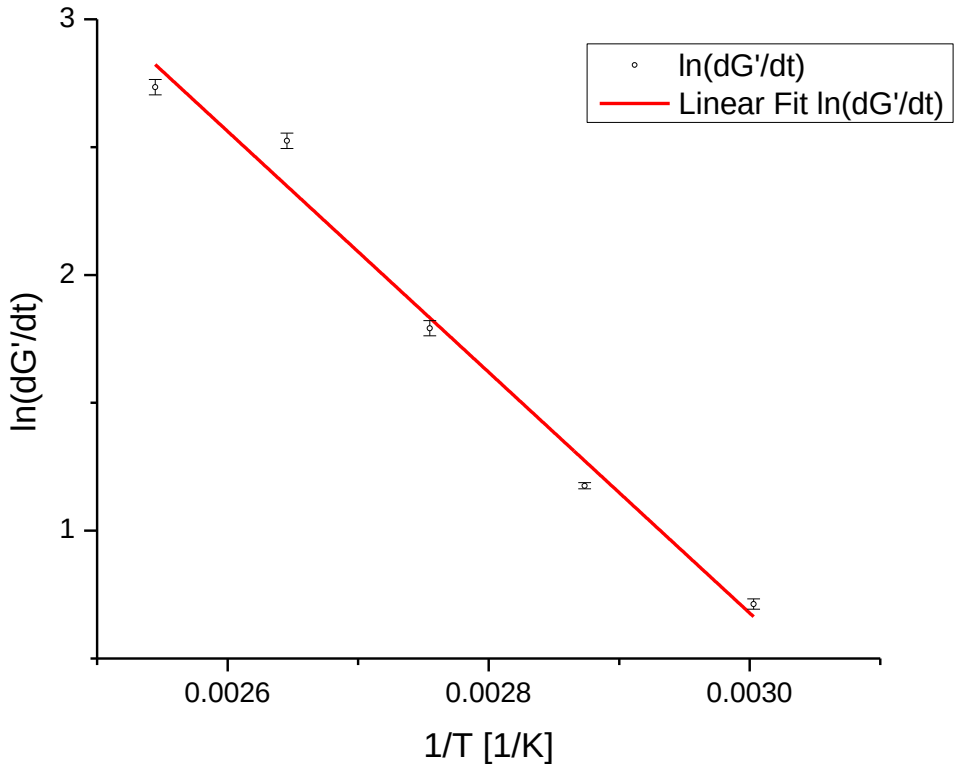

Figure 6.7: Plot of $\ln\frac{\partial G'}{\partial t}$ vs. $\frac{1}{T}$ and a linear fit, showing Arrhenius-like behavior for the recovery of the storage modulus.

S5 and S7.5. Literature shows that this transition from a glass-forming material with a prominent cold crystallization to a non-glassy conventional crystal-forming material is seen for PDMS chains that are end-functionalized to form crosslinked networks, due to local ordering of the chains, enhancing crystallization. [23]

When S15 is compression-molded, the cold crystallization, glass transition, and double melting transitions all reappear, suggesting that the shear forces induced in compression molding were sufficient to disrupt a portion of the ionic bonds in the materials, allowing a portion of the chains to behave as free chains (Fig. 6.10). Once the sample is annealed, the glass transition and cold crystallization disappear. This offers an additional non-mechanical method for testing the annealing state of a given sample.

6.4 Conclusion

A ionically crosslinked nanoparticle hybrid material was created by melt extrusion mixing of a sulfonated silica nanopowder and a (α,ω) amine terminated poly(dimethylsiloxane). At low loadings of silica, the material was a liquid (with no phase separation), but once a critical loading (~10% by weight) was reached, the annealed material was rubber-like. Differential Scanning Calorimetry verified that the behavior transitioned from a glass-forming liquid to a rubbery solid as silica loading increased, and thermal transitions of the material followed the trends seen in other studies of chemically crosslinked PDMS. The critical role of ionic interactions between the particles and the polymer was verified by creating samples with the ionic interactions turned off by either neutralizing the particle or using an unfunctionalized polymer. In both cases the resulting material was a slurry that rapidly phase separated.

The material could be compression molded repeatedly, becoming soft and gel-like during the molding process but recovering it after annealing. The recovery process was characterized by

small-amplitude oscillations, and was shown to follow Arrhenius-like behavior with an activation energy that was twice the energy reported for segmental relaxations of unfilled PDMS systems. This recoverable strength opens new avenues for moldable thermoplastic elastomers and self-healing materials.

ACKNOWLEDGEMENT:

Ms. Brenda Fisher, whose contribution is gratefully acknowledged, carried out a scaled-up version of this synthesis to ensure that sufficient material was available to create large quantities of samples. Dr. Suren Hayrapetan, whose contribution is gratefully acknowledged, optimized and carried out the extrusion according to the sample compositions specified.

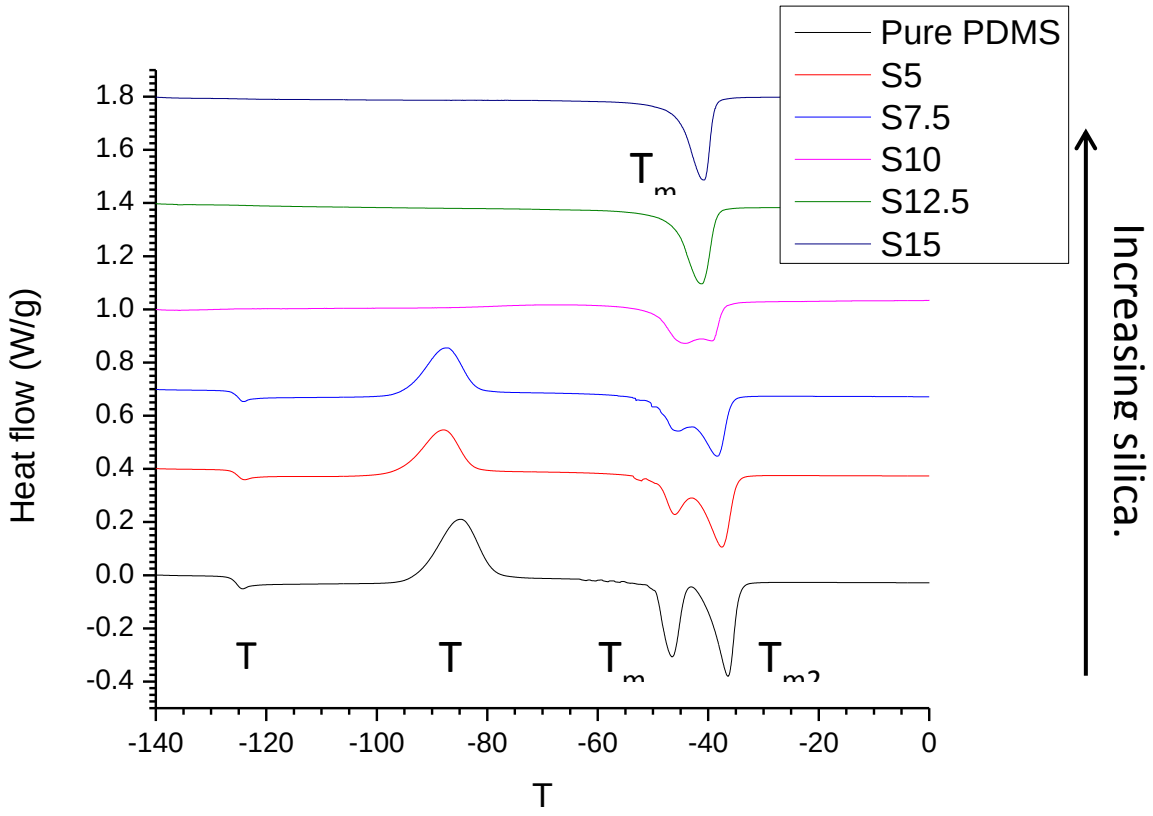

Figure 6.8: DSC thermograms (second heating) for materials with varied silica loading, showing the transition from glass-forming liquids (lower) to rubbery crystallizing solids (upper). Curves are arbitrarily offset for clarity.

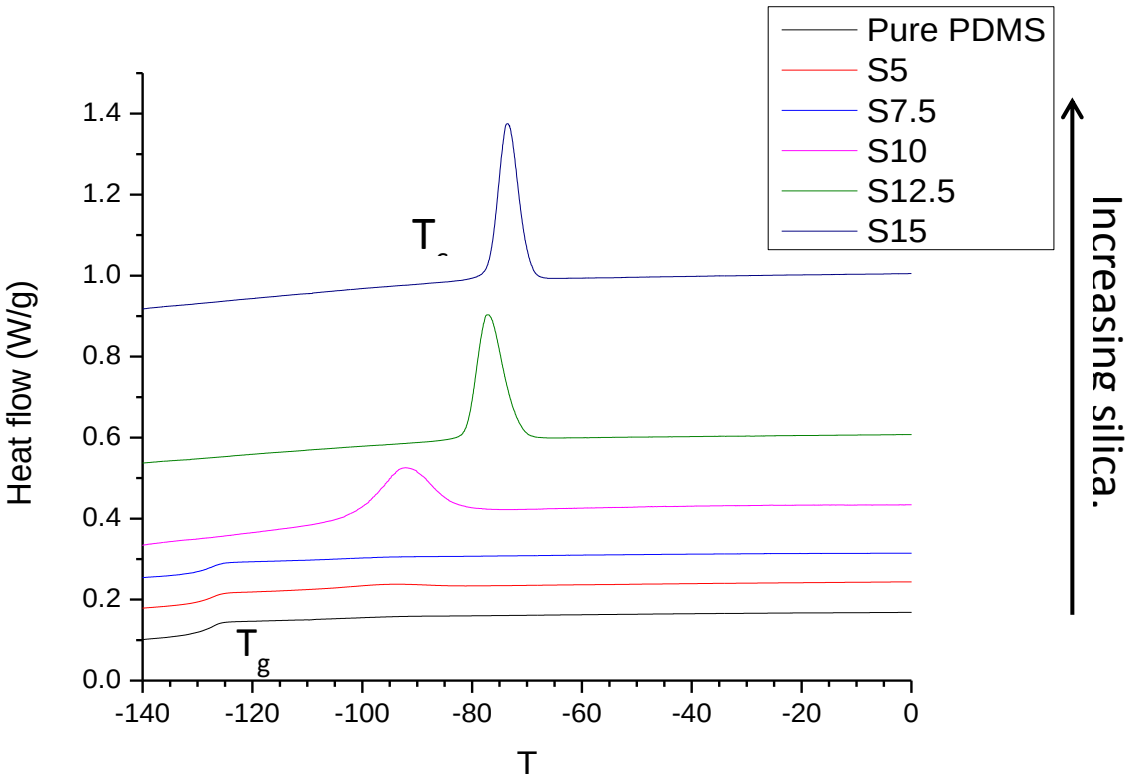

Figure 6.9: DSC thermograms (cooling) for materials with varied silica loading, showing the transition from glass-forming liquids (lower) to rubbery crystallizing solids (upper). Curves are arbitrarily offset for clarity.

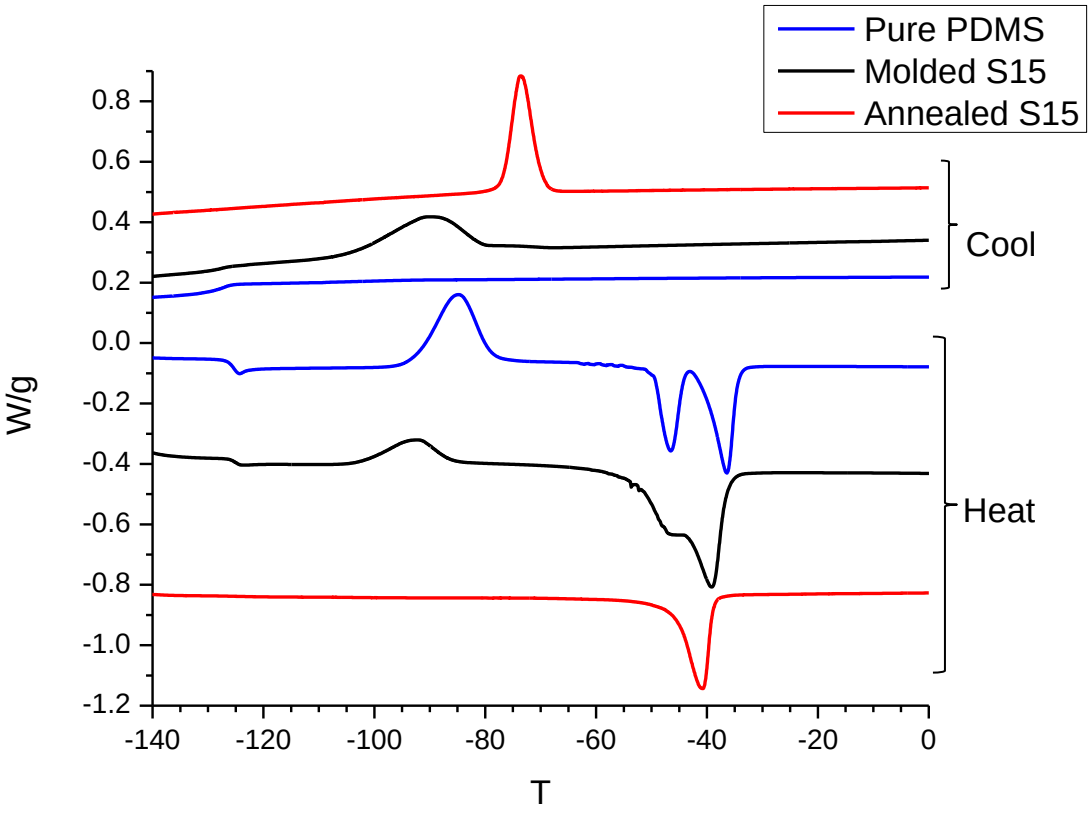

Figure 6.10: DSC thermograms for pure PDMS, compression-molded S15, and annealed S15, showing the reappearance of cold crystallization and glass transitions for the compression-molded material, verifying the disruption of crosslinks.

Sample	T_g	T_{m1}	T_{m2}	T_{m*}	T_{cc}	T_c
Pure PDMS	-126	-46.5	-36.3	--	-85.0	--
S5	-126	-46.2	-37.5	--	-88.0	--
S7.5	-126	-46.3	-38.2	--	-87.6	--
S10		-44.1	-39.1	--	--	-92.8
S12.5	--	--	--	-41.2	--	-77.3
S15	--	--	--	-40.7	--	-73.6
S15 molded	-126	-47.0	-39.2	--	-92.2	-90.5

Table 6.3: Summary of transition temperatures for the various transitions of all samples. All temperatures are in °C.

REFERENCES

(1) Krishnamoorti, R.; Vaia, R. A. Polymer nanocomposites. *J. Polym. Sci. Part B Polym. Phys.* **2007**, *45*, 3252–3256.

(2) Winey, K. I.; Vaia, R. A. Polymer Nanocomposites. *MRS Bull.* **2011**, *32*, 314–322.

(3) Vaia, R. A.; Giannelis, E. P. Polymer nanocomposites: Status and opportunities. *MRS Bull.* **2001**, *26*, 394–401.

(4) Kumar, S. K.; Krishnamoorti, R. Nanocomposites: structure, phase behavior, and properties. *Annu. Rev. Chem. Biomol. Eng.* **2010**, *1*, 37–58.

(5) Akcora, P.; Kumar, S. K.; Moll, J.; Lewis, S.; Schadler, L. S.; Li, Y.; Benicewicz, B. C.; Sandy, A.; Narayanan, S.; Ilavsky, J.; Thiyagarajan, P.; Colby, R. H.; Douglas, J. F. "Gel-like" Mechanical Reinforcement in Polymer Nanocomposite Melts. *Macromolecules* **2010**, *43*, 1003–1010.

(6) Hui, C. M.; Pietrasik, J.; Schmitt, M.; Mahoney, C.; Choi, J.; Bockstaller, M. R.; Matyjaszewski, K. Surface-Initiated Polymerization as an Enabling Tool for Multifunctional (Nano-)Engineered Hybrid Materials. *Chem. Mater.* **2013**, 130828072046006.

(7) Fernandes, N. J.; Koerner, H.; Giannelis, E. P.; Vaia, R. A. Hairy nanoparticle assemblies as one-component functional polymer nanocomposites: opportunities and challenges. *MRS Commun.* **2013**, *3*, 13–29.

(8) Fernandes, N. J.; Wallin, T. J.; Vaia, R. A.; Koerner, H.; Giannelis, E. P. Nanoscale Ionic Materials. *Chem. Mater.* **2013**, 131009111600003.

(9) Jespersen, M. L.; Mirau, P. A.; von Meerwall, E.; Vaia, R. A.; Rodriguez, R.; Giannelis, E. P. Canopy dynamics in nanoscale ionic materials. *ACS Nano* **2010**, *4*, 3735–42.

(10) Hong, B.; Panagiotopoulos, A. Z. Diffusivities, viscosities, and conductivities of solvent-free ionically grafted nanoparticles. *Soft Matter* **2013**, 6091–6102.

(11) Agarwal, P.; Qi, H.; Archer, L. A. The ages in a self-suspended nanoparticle liquid. *Nano Lett.* **2010**, *10*, 111–5.

(12) Agarwal, P.; Srivastava, S.; Archer, L. Thermal Jamming of a Colloidal Glass. *Phys. Rev. Lett.* **2011**, *107*, 268302.

(13) Agarwal, P.; Chopra, M.; Archer, L. A. Nanoparticle netpoints for shape-memory polymers. *Angew. Chem. Int. Ed. Engl.* **2011**, *50*, 8670–3.

(14) Blaiszik, B. J.; Kramer, S. L. B.; Olugebefola, S. C.; Moore, J. S.; Sottos, N. R.; White, S. R. Self-Healing Polymers and Composites. *Annu. Rev. Mater. Res.* **2010**, *40*, 179–211.

(15) Tant , Mauritz, K. A., Wilkes, G. L.,, M. R. *Ionomers : synthesis, structure, properties, and applications*; Blackie Academic & Professional: London; New York, 1997.

(16) Cordier, P.; Tournilhac, F.; Soulié-Ziakovic, C.; Leibler, L. Self-healing and thermoreversible rubber from supramolecular assembly. *Nature* **2008**, *451*, 977–80.

(17) Tee, B. C.-K.; Wang, C.; Allen, R.; Bao, Z. An electrically and mechanically self-healing composite with pressure- and flexion-sensitive properties for electronic skin applications. *Nat. Nanotechnol.* **2012**.

(18) Rodriguez, R.; Herrera, R.; Bourlinos, A. B.; Li, R.; Amassian, A.; Archer, L. A.; Giannelis, E. P. The synthesis and properties of nanoscale ionic materials. *Appl. Organomet. Chem.* **2010**, *24*, 581–589.

(19) Chen, X.; Stowell, J. G.; Morris, K. R.; Byrn, S. R. Quantitative study of solid-state acid-base reactions between polymorphs of flufenamic acid and magnesium oxide using X-ray powder diffraction. *J. Pharm. Biomed. Anal.* **2010**, *51*, 866–74.

(20) Erwin, B. M.; Vlassopoulos, D.; Cloitre, M. Rheological fingerprinting of an aging soft colloidal glass. *J. Rheol. (N. Y. N. Y).* **2010**, *54*, 915.

(21) Jiang, H.; Su, W.; Mather, P. T.; Bunning, T. J. Rheology of highly swollen chitosan/polyacrylate hydrogels. *Polymer (Guildf).* **1999**, *40*, 4593–4602.

(22) Roland, C. M.; Santangelo, P. G. Effect of temperature on the terminal relaxation of branched polydimethysiloxane. *J. Non. Cryst. Solids* **2002**, *307-310*, 835–841.

(23) Dollase, T.; Spiess, H. W.; Gottlieb, M.; Yerushalmi-Rozen, R. Crystallization of PDMS: The effect of physical and chemical crosslinks. *Europhys. Lett.* **2002**, *60*, 390–396.

CONCLUSIONS AND FUTURE WORK

As seen in this dissertation, the ionic bond at the heart of the NIMs platform endows it with both versatility and unique properties. In chapter 2, the wide variety of core-canopy combinations, and the applications thereof are highlighted. Chapter 2 also discusses the state of the literature regarding the canopy structure, and highlights the lack of a phase map and a detailed understanding of how the multilayer canopy model seen in NMR experiments affects the physical properties of NIMs. Chapter 3 is the first report of the corona-free synthesis concept, demonstrating the use of inherent surface charge in metal oxides to create NIMs.

In Chapter 4, the dependence of mechanical properties of NIMs on graft density and polymer molecular weight are examined, addressing the questions raised in chapter 2. Soft glassy behavior seen in hairy nanoparticle systems and star polymers is also seen in NIMs, verifying the expected model. It is found that the predicted occurrence of the multilayer canopy corresponds well with the transition from soft glassy to liquid behavior.

Chapters 5 and 6 focus on the use of ionic interactions to link multiple nanoparticles together. Chapter 5 examines the effect of crosslinks on otherwise identical systems, showing that toughness can increase with the use of multivalent branched polymers in the place of monovalent linear polymers without altering any other parameters. Chapter 6 examines the effect of changing nanoparticle concentrations in loaded divalent poly(dimethylsiloxane) system, creating a material that has rubberlike properties with novel self-healing behavior. In addition, the importance of the ionic bond is once again demonstrated.

All the work done here has been focused on two well-understood ionic bonds. A fundamental question that remains unanswered is the effect of changing the strength of the ionic bond, as well as the difference between ionic and covalent bonds. This is a question of

fundamental importance that can be answered by comparing the properties of carefully synthesized covalently grafted nanoparticles with identical systems with hydrogen bonding as well as ionic bonding.

Further work remains to be done on the phase map presented in chapter 4. Specifically, further Ultra-Small Angle X-Ray Scattering work would enable a discussion of order-disorder transitions in relation to graft density and molecular weight. Neutron scattering using a combination of deuterated and unmodified canopy molecules would reveal the multilayer structure in greater detail. Further, the effect of particle radius and polymer persistence length needs further examination.

An unexplored avenue is the creation of superlattices using varying sizes of particles. Another approach for this is using opposing charges of particles. These superlattices, when combined with the crosslinking motifs discussed in chapter 5 and 6, can lead to novel structures that may have significant applications as stand-alone functional materials, or as green bodies for porous membranes.